

# Temporal Landscape of Brain Connectivity in Aging, Disease, and Enhanced Imaging: Data-Driven Insights

**Nisha Chetana Sastry**

*Thesis submitted to  
National Brain Research Centre  
for the award of  
Doctor of Philosophy in Neuroscience*



National Brain Research Centre  
(Deemed to be University)  
Manesar, Haryana, India 122052

## CERTIFICATE

This is to certify that the thesis entitled '**Temporal landscape of brain connectivity in aging, disease and enhanced imaging: Data-driven insights**' is the result of work carried out by **Nisha Chetana Sastry** in the Division of Cognitive and Computational Neuroscience at National Brain Research Centre, Manesar, Haryana, India, towards requirements for Ph.D. degree.

The work presented herein is original and has not been submitted previously for the award of any degree or diploma to **National Brain Research Centre (Deemed to be University)** or to any other University. The work is as per the guidelines given by **National Brain Research Centre (Deemed to be University)** and is a record of the candidate's own efforts.

Dr. Arpan Banerjee

(Director, NBRC)

Scientist VI & Professor,  
National Brain Research Centre,  
NH-8, Manesar, Haryana 122052.  
(Supervisor)

Place: Manesar

Date:

## DECLARATION BY THE CANDIDATE

I, **Nisha Chetana Sastry**, hereby declare that the work presented in the form of this thesis was carried out by me under the guidance of **Dr. Arpan Banerjee**, Scientist VI & Professor, Cognitive and Computational Neuroscience division of **National Brain Research Centre (Deemed to be University)**, Manesar, Haryana, India.

I declare that no part of the thesis contains any plagiarised material. Any previously published or other material sourced from anywhere else has been appropriately attributed to the source.

I also declare that no part of this thesis has been previously submitted for the award of any degree or diploma to **National Brain Research Centre (Deemed to be University)** or to any other university.

Place: Manesar

Nisha Chetana Sastry

Date:



*Dedicated to,*

*Appa,*

*for teaching me how to fly*

*Amma,*


*for being the wind beneath my wings*

*Shubham,*

*for holding my hands in this adventure and in life*

*Maa,*

*for showing me what love and honesty can achieve*



*In loving memory of*

*Ajji,*

*A tigress*

*Who instilled academic prowess to her cubs*

*Papa,*

*A big banyan tree*

*Whose protective canopy I miss dearly*

# Acknowledgement

Pursuing my PhD at NBRC has been a profoundly transformative decision in my life journey. I want to express my gratitude to the many influences within this tranquil environment that have contributed to shaping my philosophical outlook on life, fostering my appreciation for solitude, and nurturing my capacity for critical thinking and continuous learning.

Foremost, I extend my heartfelt thanks to my advisor, Dr. Arpan Banerjee, whose unwavering support and guidance have been instrumental in my academic journey. Dr. Banerjee provided me with the precious gift of intellectual freedom, allowing me to explore, absorb knowledge and research at my own pace. I eventually came to deeply value and savour this academic independence once I found my footing. I extend my heartfelt gratitude to my co-supervisor, Dr. Dipanjan Roy, whose extensive knowledge of the literature, unwavering enthusiasm for scientific inquiry, and adept supervision have been invaluable to my journey. I would also like to thank my doctoral committee members – Prof Soumya Iyengar and Prof Ellora Sen for their time and astute guidance. I owe a debt of gratitude to Prof Sen for being a source of comfort during my father's illness. I wholeheartedly acknowledge the essential financial support provided by NBRC core funds for my doctoral research. Additionally, I'm grateful for the travel aid that enabled me to attend conferences, expand my academic horizons, and further enrich my learning experience

I extend my special thanks to my amazing lab mates, both past and present, for creating a warm and familial atmosphere within our lab. I will always treasure our lab meetings, the lively discussions that spilled over to the monu's, canteen, and sometimes culminated in our legendary lab parties. My heartfelt gratitude goes out to Kasturi, Ritu, Pratika, Priyanka, Vinsea, Mritikka and Yudhajit for their delightful company and the many insightful discussions we've had, both scientific and otherwise. I'd like to give a special thanks to the dynamic duo, Neeraj and Abhishek, for their unwavering companionship and willingness to engage in extensive conversations on a wide array of topics. I also want to express my gratitude to my batchmates for the wonderful memories we've created over the years. Barath, Hyma, and Shrey, you were my first friends at NBRC, and I cherish the moments we've shared. A big shoutout to the OG group - Apoorv Bhaiya, Vinodh, Bala, Guncha di, Kautuk, and Shanko di, who generously adopted me and provided a sense of protection. A heartfelt thanks to Sarbani di for always being like a maternal source of comfort and support. And of course, huge thank you to countless generations of little birds, puppies and kittens, who greeted me every single day, waiting at my doorstep, that I have had the privilege to love and play with.

I'm deeply grateful to Prof. Shobhana Narasimhan, whose kind encouragement and support, initiated by a simple email years ago, after reading her story in the 'Leelavath's daughters', played a pivotal role in my decision to pursue doctoral research. Heartfelt gratitude to my father's scientific circle – Prof Sujata Ramadorai, Prof KPJ reddy, Prof Shylaja, Prof Rohini Godbole, Prof Ganeshiah for their vibrant discussions at home, which illuminated the captivating world of research.

I owe all of this to the unwavering love and support of my family. Amma, you are the captain of our ship. Your unwavering strength has been my anchor in tough times,

making them bearable, and your love has made the good times truly wonderful. Appa, I am profoundly grateful for the scholarly and academic atmosphere at home, where learning was not just a pursuit but a source of joy. From nurturing bonsais, building telescopes, collecting fossils, exploring temple architectures, delving into paintings, music, classical literature, and especially mathematics, your unique guidance has been invaluable. To Shubham, the refreshing breeze in my life, my most precious gift, my wonderful husband, I express my heartfelt gratitude. Thank you for always holding my hand and for being my best friend above all else. Maa, your boundless love and kindness have enveloped me with warmth and care. You are not only my mother but also my close friend and guide, all rolled into one. To Saksham, thank you for the exotic snacks and the joyous laughter you bring. And to my extended family - Bhagya, Chinnu, Valli aunty, Mythili aunty, Chikkappa, Shubbi - your relentless support has made all of this possible.

Nisha

Sep 2023



# Table of Contents

List of Figures .....	i
List of Tables .....	vii
List of abbreviations .....	viii
1. Introduction .....	1
1.1. AI and Neuroscience – A symbiotic relationship .....	1
1.2. Part I: Brain connectivity patterns – An entry point .....	5
1.3. Functional connectome: dynamics and stability .....	8
1.4. Part II: Low field neuroimaging – Fresh perspectives .....	12
1.5. Clinical Significance.....	14
1.6. Summary and scope of the thesis .....	15
2. Temporal stability in resting state, movie watching and sensorimotor task across healthy ageing .....	18
2.1. Introduction.....	18
2.2. Methods.....	22
2.3. Results .....	33
2.4. Discussion .....	46
3. Temporal stability of resting state functional connectome across common mental disorders .....	57
3.1. Introduction.....	57
3.2. Materials and Methods .....	62
3.3. Results .....	75
3.4. Discussion .....	89

4. Towards translational low-field neuroimaging .....	96
4.1. Introduction.....	96
4.2. Materials and Methods .....	101
4.3. Results .....	114
4.4. Discussion .....	121
5. Conclusion .....	124
References.....	128
Appendix .....	145
List of Publications .....	154
Selected list of Conferences.....	155

# List of Figures

1.1. <b>Parallels between AI and Neuroscience.</b> (A) A Venn diagram showing the relationship and interdependencies between artificial intelligence (AI), machine learning (ML) and deep learning (DL) (B) Parallels between brain circuitry (biological) and a neural network (adapted from Shimon Ullman. Science. 2019).....	3
1.2. <b>A cartoon flowchart of two ways of diagnosis:</b> An expert radiologist and an AI model (ML or DL model). For AI modelling biological systems, it is imperative that the features, or perhaps computational biomarkers, are rooted in substantial biological evidence. (The figure is adapted and edited from Computer Science and Artificial Intelligence Lab. MIT – Mike Miliard 2023) .....	5
1.3. <b>Overview of static FC and Dynamic FC estimation.</b> (A) Static functional connectivity involves the averaging of brain activity across time intervals by calculating pearson correlation over the entire duration of the scan. There is one FC matrix for the entire duration of the scan (B) Sliding window approach to estimate dynamic FC involves computing average FC over small windows of time, and subsequently sliding the window over the entire duration of the BOLD time series.....	8
1.4. <b>Brief Summary of Brain State Studies</b> (A) (Cabral , et al., 2017) employ the K-means clustering technique to compress brain activity into discrete brain states. (B) (Vidaurre, Smith, & Woolrich, 2017) utilize Hidden Markov Model (HMM) clustering to achieve a similar compression of brain activity into discrete brain states.....	11
1.5. <b>Overview of temporal variability of brain networks.</b> (Zhang , et al., 2016) view the temporal dynamics of dynamic functional connectivity (dFC) as a continuous process, without segmenting it into discrete brain states and use pearson correlation to gauge the variability in temporal dynamics.....	12
2.1 <b>Brief overview of the unsupervised approach</b> (A) The schematic diagram shows how the temporal stability of dynamic functional connectivity subspaces (dFC) are computed. Dominant dFC subspace, at each time point, is estimated using the first three principal components of dFC(t), that was computed using the measure of BOLD phase coherence. The similarity between dFC subspaces is calculated using Angular distance (principal angle) and Mahalanobis distance (Euclidean distance). If the dominant dFC subspaces are similar for extended timepoints, then they are considered to be stable. (B) A flowchart representation of the method (C) Matrix representation of dFC patterns (dFC(t)) and reduced Dominant dFC patterns (D(t)) at t=40.....	25

**2.2 Using angular distance to characterise temporal stability matrices across age** (A) dFC matrices estimated using BOLD phase coherence. (B) Time X Time temporal stability matrix of resting state, naturalistic movie watching task and discrete, sensorimotor task for young, middle and old adults. Each entry in the matrix is the principal angle  $\phi(t_x, t_y)$  between dominant dFC subspaces at  $t_x$  and  $t_y$ . The principal angle ranges between 0 (low angular distance) to  $\pi/2$  (high angular distance). Resting state, in young, middle and old adults, has shorter-lived, global spread of patterns of temporal stability. On the contrary, both the tasks have a longer-lived, local spread of patterns of stability (indicated by arrows and rectangular boxes).....34

**2.3 Using Mahalanobis distance to characterise temporal stability matrices across age.** (A) Time X Time temporal stability matrix of resting state, naturalistic movie watching task, and sensorimotor task for young, middle and old adults, where each entry in the matrix is Mahalanobis ( $M^2(t_x, t_y)$ ) distance between the dominant dFC subspaces. Mahalanobis distance between dominant dFC subspaces is low when the dFC configurations are similar. (B) The profile of temporal stability estimated with Mahalanobis distance between dominant dFC subspaces at  $t=15$  and  $t=150$ ,  $t=50$ ,  $t=200$  across the brain regions.....35

**2.4 Quantifying complexity of temporal stability matrices across age** (A) Plots representing entropy of temporal stability matrices of resting state (rest), naturalistic movie watching task (movie) and sensorimotor task (SMT) across lifespan, for Angular distance and Mahalanobis distance metric. The subjects were divided into non-overlapping bins of 5 years starting from 18 years to 88 years (18-20, 21-25, 26-30, 31-35, 36-40, 41-45, 46-50, 51-55, 56-60, 61-65, 66-70, 71-75, 76-80, 81-88). (B) Plots representing entropy of temporal stability matrices of resting state (rest), naturalistic movie watching task (movie) and sensorimotor task (SMT) for young (cyan), middle (blue) and old (pink) adults, for Angular distance and Mahalanobis distance metric. Statistically significant differences (uncorrected) are indicated using \* ( $\mathcal{P} \leq 0.05$ ), \*\* ( $\mathcal{P} \leq 0.01$ ), \*\*\* ( $\mathcal{P} \leq 0.01$ ), \*\*\*\* ( $\mathcal{P} \leq 0.001$ ), \*\*\*\* ( $\mathcal{P} \leq 0.0001$ ), ns (not significant). (C) Plots representing distribution of Frobenius distance between temporal stability matrices of resting state, naturalistic movie watching (yellow) and resting state, sensorimotor task (purple) for Angular distance, and Mahalanobis distance metric, in young, middle and old adults. The violin plots reveal a shorter Frobenius norm between resting state and movie watching task than resting state and sensorimotor task in all young, middle and old adults.....37

**2.5 Age related changes in temporal stability of dynamic functional connectivity of whole-brain resting state** (A), sensorimotor network (B), central executive network (C) and Visual network (D) estimated with angular distance metric. Only those networks with significant modifications in temporal stability with age are shown. Statistically significant differences (uncorrected) are indicated using \* ( $\mathcal{P} \leq 0.05$ ), \*\* ( $\mathcal{P} \leq 0.01$ ), \*\*\* ( $\mathcal{P} \leq 0.01$ ), \*\*\*\* ( $\mathcal{P} \leq 0.001$ ), \*\*\*\* ( $\mathcal{P} \leq 0.0001$ ), ns (not significant).....40

**2.6 Spatial profile of Mahalanobis distance across resting state networks** (A) Short-range temporal stability - Mahalanobis distance between dominant dFC subspaces of Default mode network (DMN), Central executive network (CEN), Sensorimotor network (SM), Salience, and Visual brain networks at t=15 and t=20. (B) Long-range temporal stability - Mahalanobis distance between dominant dFC subspaces of Default mode network (DMN), Central executive network (CEN), Sensorimotor network (SM), Salience, and Visual brain networks at t=15 and t=150. ....41

**2.7 Stochastic characterization of dFC** (A) Stochastic modelling of principal angle,  $\phi(t)$  as autoregressive, AR ( $\rho$ ) process. The model order ( $\rho$ ) was varied from 0 to 100. The plot represents Akaike information criterion (AIC) values corresponding to the model order. Inset shows the first minima of the AIC value and its corresponding model order. (B) Table shows first minimal AIC value and its corresponding model order of  $\phi(t)$  for all the categories (C) Stochastic modelling of Mahalanobis distance,  $M(t)$  as AR ( $\rho$ ) process. The model order ( $\rho$ ) was varied from 0 to 100. The plot represents AIC values corresponding to the model order. Inset shows the first minima of the AIC value and its corresponding model order. (D) Table shows first minimal AIC value and its corresponding model order of  $M(t)$  for all the categories.....44

**3.1. A brief overview of the methodology used in this study.** (A) shows the BOLD time series data (B) illustrates the estimation of static functional connectivity using Pearson correlation, which is then transformed using the r-to-z method (C) displays topographic representation of the WSBM communities. The subject-wise undirected, signed, weighted adjacency matrix serves as the input for the Weighted Stochastic Block Model (WSBM), a data-driven generative community detection algorithm that groups brain areas into  $K=7$  communities based on their stochastic equivalence. (D) presents the matrix representation of the reduced dominant dynamic functional connectivity (dFC) patterns, denoted as  $D(t)$ , computed at each time point (E) demonstrates the calculation of similarity between dominant dFC subspaces using angular distance or principal angle ( $\phi$ ) (F) showcases the Time X Time temporal stability matrix, where each entry represents the principal angle ( $\phi(t_x, t_y)$ ) between dominant dFC subspaces at time points  $t_x$  and  $t_y$ . This matrix visualizes the temporal landscape, with the principal angle ranging from 0 (indicating low angular distance) to  $\pi/2$  (indicating high angular distance). Constructing a Time X Time temporal stability matrix allows us to visualize the temporal "landscape" for the entire duration of the scan. (G) we calculate the temporal stability of the dynamic functional connectome using two measures: entropy and global temporal distance. We investigate changes in community architecture in common mental health disorders such as schizophrenia, bipolar disorder, and ADHD.....64

<b>3.2. An overview of the community architecture differences between schizophrenics and healthy controls in Dataset 1</b>	
(A) shows the static functional connectivity matrices of schizophrenics and healthy controls, with brain areas ordered by communities (B) presents the partition of cortical regions into 7 communities using the Weighted Stochastic Block Model (WSBM), a generative community detection algorithm that groups stochastically equivalent brain regions into communities (C) each pair of communities ( $r$ and $s$ ) is classified into one of three community motifs: assortative, coreness, and peripheryness. The diversity index is calculated as the average across all brain regions per subject. The violin plots indicate that in schizophrenics, communities are less assortative (D) illustrates the construction of a network morphospace using all pairs of communities, which are coloured according to their motif type: blue for assortative community interactions and green for core or periphery community interactions.....	76
<b>3.3. Profile of brain regions showing significant difference in assortativity between patients, age and sex matched healthy controls</b>	
(A) ADHD (B) bipolar disorder (C) Schizophrenia.....	80
<b>3.4. An overview of the temporal stability differences between schizophrenia and healthy controls in Dataset 1</b>	
(A) showcases the Time X Time temporal stability matrices, visualized as the 'Temporal landscape'. Each entry represents the angular distance between dominant dFC subspaces at time points $t_x$ and $t_y$ , for patients with schizophrenia and healthy controls. In schizophrenics, there is a global spread of shorter-lived, low angular distant (yellow hue) repeated patterns of stability (B) focuses on quantifying temporal stability across the entire Time X Time temporal landscape using entropy (C) quantifies temporal stability over successive time points using global temporal distance. Both measures indicate low temporal stability in schizophrenics (D) global temporal distance is estimated for all the resting state networks defined in the Schaeffer atlas, comparing schizophrenics (purple) and healthy controls (orange).....	81
<b>3.5. An overview of the temporal stability differences in participants with ADHD and Bipolar disorder</b>	
(A) showcases the Time X Time temporal stability matrices, where each entry represents the angular distance between dominant dFC subspaces at time points $t_x$ and $t_y$ , for participants with ADHD and Bipolar disorder. The temporal stability is quantified using two measures: entropy (B) and global temporal distance (C) in patients with ADHD and healthy controls. The results show that global temporal distance is significantly higher in participants with ADHD, indicating decreased temporal stability. Similarly, temporal stability is quantified using entropy (D) and global temporal distance € in participants with bipolar disorder and healthy controls.....	86

- 3.6. **An overview of the temporal stability differences between individuals with schizophrenia and healthy controls in Dataset 2.** (A) illustrates the temporal stability matrices, visualized as a temporal landscape, for both schizophrenics and healthy controls. Each entry in the matrix represents the angular distance between dominant dFC subspaces at time points  $t_x$  and  $t_y$ . The angular distance ranges from 0 (indicated by yellow hue) to  $\pi/2$  (indicated by red hue) (B) quantifies the temporal stability across the entire temporal landscape using entropy (C) quantifies the temporal stability over successive time windows using global temporal distance. Both measures indicate a decrease in temporal stability in schizophrenics, which aligns with the findings from Dataset 1. (D) estimates the global temporal distance for each of the resting state networks defined in the Schaeffer atlas for both individuals with schizophrenia (purple) and healthy controls (orange). The plots demonstrate a significant decrease in temporal stability in schizophrenics, particularly in the control, dorsal attention, default, somatomotor, temporal parietal, and ventral attention networks.....88
- 4.1. **Portable Hyperfine 64 mT MR scanner.** Hyperfine Swoop, the world's first portable MR imaging system, is capable of providing neuroimaging at the point of care. Its capabilities enable timely diagnosis and treatment of acute conditions across various clinical settings.....102
- 4.2. **T1 w MR images used in the study** (A) Original 3D MR image or “Ground Truth” of two representative participants from the empirical hyperfine dataset (B) Original 3D MR image or “Ground Truth” of two simulated T1w images from the BrainWeb database with added Gaussian noise at 3% and 9%.....103
- 4.3. **Overview of SynthSR pipeline (adapted from (Iglesias , et al., 2021))** (A) The utilization of deep convolutional neural networks, exemplified by the SynthSR framework, presents a robust approach for enhancing images. In this context, the input comprises low-field hyperfine T1-weighted (T1w) MR images. The essence of this approach lies in training the convolutional neural network (CNN) on simulated T1 images, capitalizing on advanced machine learning techniques to achieve image enhancement. (B) In this diagram, the blue arrows represent the generative model, facilitating the sampling of random scans at each minibatch with GPU implementation. On the other hand, the red arrows connect the inputs and regression targets used during training for either super-resolution (SR) or joint SR/synthesis. It is important to note that real images are only necessary for joint SR/synthesis, and not for SR alone.....105
- 4.4. **Schematic diagram gives an overview of the NL means implementation.** The input to the algorithm is either an empirical 3D MR image (a) or a phantom 3D MR image generated with Brain Web database with two different noise levels (b). The denoising through NL means algorithm restores the value of voxel  $x_i$  (in red) with the weighted average of all intensities of  $x_j$  in the search volume  $V_i$ , based on the similarities of their intensity neighbourhoods,  $N_i$  and  $N_j$ . Output of the algorithm is a denoised 3D MR image.....106

4.5. **Image quality transfer (IQT) using SynthSR on hyperfine dataset.** Shown here are T1-weighted (T1w) images of two representative individuals both before and after undergoing image quality transfer (IQT) using SynthSR. These empirical data were acquired on a 64 mT Hyperfine MRI scanner, which is the world's first portable MRI scanner. Upon visual examination, the enhancement in image quality of hyperfine T1w images after IQT is evident.....113

4.6. **Calibration of NL means algorithm and Image quality metrics** (A) Calibration of  $\beta$  (adjusting constant to tune smoothing parameter  $h$ ) and  $\sigma^2$  (limiting constant for variance of  $u(N_i)$  and  $u(N_j)$ ). We check the influence of  $\beta$  for and  $\sigma^2$  on PSNR, MSE and SSIM. PSNR is high for low values of  $\beta$  and  $\sigma^2$ , peaking at  $\beta = 0.2$  and  $\sigma^2 = 0.5$  .....115

4.7. **Quantifying the performance of NL means algorithm** (A) Quantifying the performance of NL means across empirical and synthetic dataset. We estimate PSNR, MSE and SSIM for all the available participants of empirical dataset after denoising with NL means and validate the same with synthetic dataset. For the empirical dataset, we report the results of two participants with highest PSNR. We run NL means algorithm with  $\beta = 0.2$  and  $\sigma^2 = 0.5$ . These results suggest good performance of NL means algorithm on the empirical/synthetic dataset. (B) Original 3D MR image or "Ground Truth" of two simulated T1w images from the Brain Web database with added Gaussian noise at 3% and 9%.....116

4.8. **Before and after NL means.** Comparison between Ground truth and denoised images after applying NL means algorithm on T1w images: Synthetic data with 3% and 9% added Gaussian noise and Empirical data.

**Top:** Original Ground Truth T1-w images - Synthetic and empirical

**Middle:** Detailed zoomed-in images contrasting ground truth and denoised T1-w images of synthetic and empirical data. Denoising is achieved with NL means algorithm with adjusting constant of smoothing parameter ( $\beta$ )=0.2. Adjusting parameter controls the strength of denoising.

**Bottom:** Original denoised T1-w images obtained after applying NL means algorithm on synthetic and empirical MR images. ....117

4.9. **Image quality analysis metrics.** Quantifying the performance of NL means across empirical and synthetic dataset using two metrics - JPEG compression-based image quality analysis (A) and Image quality evaluation (B).....119

4.10 **Before and after NL means.** Visual comparison of T1w images for all subjects before and after the application of the NL means algorithm.....120



# List of Tables

**Table 3.1** Demographics of the UCLA consortium for Neuropsychiatric phenomics LA5c dataset (Dataset 1) and COBRE dataset (Dataset 2) . . . . . 66


**Table 3.2** Region wise significant assortativity differences in patients with schizophrenia, age and sex matched healthy controls. . . . . 82

**Table 3.3** Region wise significant assortativity differences in patients with bipolar disorder, age and sex matched healthy controls. . . . . 82

**Table 3.4** Region wise significant assortativity differences in patients with ADHD, age and sex matched healthy controls. . . . . 83

# List of Abbreviations

AAL	Automated Anatomical Atlas
ADHD	Attention-Deficit Hyperactivity Disorder
AR	Autoregressive
BOLD	Blood Oxygen Level Dependant
BP	Bipolar Disorder
Cam-CAN	Cambridge Centre for Ageing Neuroscience
CEN	Central Executive Network
CNN	Convolutional Neural Networks
DAN	Dorsal Attention Network
DCT	Discrete Cosine Transform
dFC	Dynamic Functional Connectivity
DL	Deep Learning
DMN	Default Mode Network
EPI	Echo-Planar Imaging
FC	Functional Connectivity
fMRI	Functional Magnetic Resonance Imaging
IQE	Image Quality Evaluation
IQT	Image Quality Transfer
JPEG	Joint Photographic Expert Group
LMIC	Lower- and Middle-Income Countries
ML	Machine Learning
MRI	Magnetic Resonance Imaging



MSE	Mean Squared Error
PCA	Principal Component Analysis
PDE	Partial Differential Equation
PSNR	Peak Signal to Noise Ratio
RSN	Resting State Network
SCID	Structured Clinical interview used for DSM disorders
sFC	Static Functional Connectivity
SM	Sensorimotor Network
SMT	Sensorimotor Task
SSIM	Structure Similarity Index Measure
SZ	Schizophrenia
TS	Temporal Stability
VAN	Ventral Attention Network
VN	Visual Network
WSBM	Weighted Stochastic Block Model

# Chapter 1

## Introduction

### 1.1 AI and Neuroscience – A symbiotic relationship

From the earliest stages of human involvement in agriculture and the gradual development of civilizations, a discernible trend emerges—a distinct scientific accomplishment that has the power to redefine the path of each century and fundamentally reshape the trajectory of human civilization. This pattern underscores the transformative influence that pivotal scientific breakthroughs exert on the historical narrative and the evolution of our shared human existence (Diamond, 1997). In the past century, one can argue from a pure scientific standpoint, the Manhattan Project and the utilization of nuclear energy for defence, energy generation, and more, emerge as a defining scientific feat—one that unmistakably reshaped human evolution. In the current 21<sup>st</sup> century, it is increasingly apparent that, with recent advancements like the ChatGPT and DALL-E, products of the organization OpenAI (<https://openai.com/>), artificial intelligence is poised to assume a defining role. Its potential to deeply penetrate every facet of human life is evident, suggesting its transformative influence on the entirety of human existence. But what precisely defines artificial intelligence or AI? In its essence, AI encompasses the realm of machines and softwares capable of executing tasks that traditionally necessitate human cognitive capabilities (Figure 1.1A). Interestingly, upon closer examination, a thought-provoking parallel arises between AI and neuroscience, both converging toward a common focal point. At

the core of this convergence lies the endeavour to understand and replicate the intricacies of the human brain's functioning. Viewed through this lens, artificial intelligence emerges as a pioneering force in innovation, aiming to traverse the divide between human intelligence and artificial constructs (Winston, 1984). This aspiration finds harmony with the essence of neuroscience—a discipline dedicated to the understanding of the intricate networks within the human brain. Likewise, professionals in the domain of artificial intelligence undertake the task of crafting neural networks that exhibit a remarkable semblance, mirroring both the structural composition and organizational dynamics of the intricate human nervous system (Figure 1.1B). As artificial intelligence strives to replicate human thought patterns, it takes on the role of embodying the collective insights amassed from neuroscience's continuous efforts in cracking the *brain-puzzle*.

A prominent application of artificial intelligence resides within the healthcare industry, notably in the realm of diagnostics (Ramesh , Khambhanpati , Monson , & Drew , 2004). Consider, for instance, the scenario of an adept clinical radiologist—an individual possessing specialized knowledge. When presented with an MRI scan of a patient, this radiologist can proficiently identify ailments like meningitis or ischemic blood clots from the imagery. Today, with the remarkable progress achieved in the field of AI, the possibility emerges to train a convolutional neural network (CNNs) based deep learning model. This model, through a process of assimilating the distinctive attributes inherent in MRI scans, is capable of replicating the precise diagnostic outcomes achieved by the skilled radiologist, thereby yielding a commendable level of accuracy. However, a crucial consideration comes to the fore. The potency and accuracy of a deep learning model are inherently contingent upon the parameters we define, as its learning

process is predicated solely upon the data or "*features*" provided. The model's precision stands in direct correlation with the calibre of these features, the inputs that shape its learning (Ramesh , Khambhanpati , Monson , & Drew , 2004). This becomes especially pertinent when applying deep learning or machine learning models to biological systems, such as comprehending the complexities of the human brain. In this context, it becomes imperative that these *features*, or perhaps more aptly put, *computational biomarkers*, are rooted in substantiated biological evidence. When these features are founded upon biological evidence, the predictions the model generates closely align with the outcomes manifested within the biological systems it seeks to emulate.

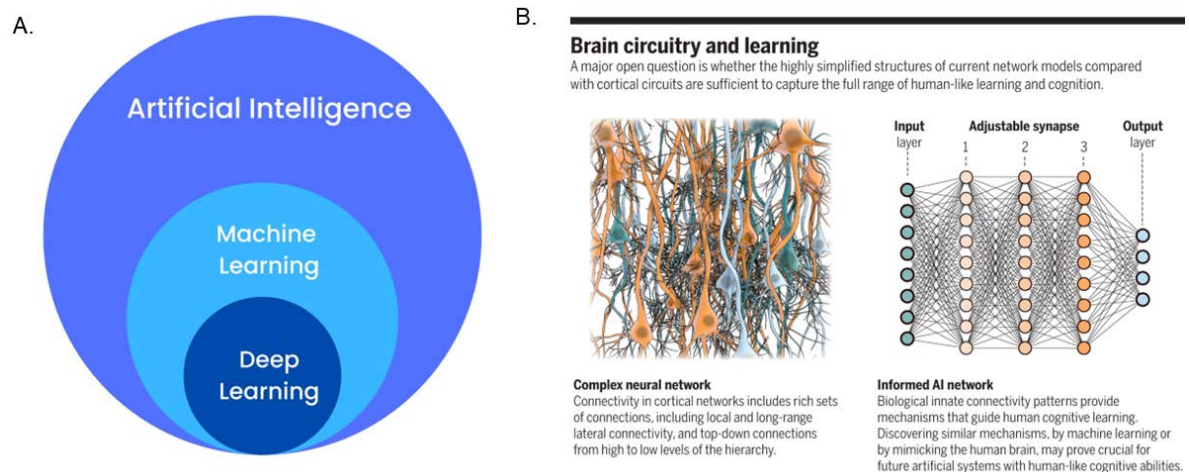


**Figure 1.1 Parallels between AI and Neuroscience.** (A) A Venn diagram showing the relationship and interdependencies between artificial intelligence (AI), machine learning (ML) and deep learning (DL) (B) Parallels between brain circuitry (biological) and a neural network (adapted from Shimon Ullman. *Science*. 2019)

Machine learning algorithms fall into two broader categories: supervised and unsupervised learning algorithms (Ray , 2019). The fundamental distinction between supervised and unsupervised learning lies in the requirement for labelled training data. Supervised machine learning algorithms rely on input and output data that have been appropriately labelled, whereas unsupervised learning algorithms

process unlabelled or raw data. In the realm of supervised machine learning, the model gains insights from the relationships embedded within the labelled input and output data. However, it's worth noting that creating labelled training data can frequently be resource-intensive. Conversely, unsupervised machine learning operates by extracting knowledge from unlabelled raw training data. An unsupervised or a data driven model delves into the intricacies of the unlabelled dataset, unveiling relationships and patterns that inherently reside within (Ray , 2019). This approach is often harnessed to unearth latent trends present within a given dataset. In response to the challenge of identifying biological evidence-based *features*, certain initiatives within the field have embarked upon the utilization of supervised learning algorithms (For example: Neuroimaging markers for Alzheimer's disease (Amini, Pedram , Moradi , Jamshidi , & Ouchani , 2021)). Nevertheless, it is imperative to recognize that this particular approach is not exempt from issues of its own. A particularly salient issue revolves around the potential introduction of bias during the analysis process, thereby posing a significant threat to the fidelity of the model's predictions (Viduarre, Smith, & Woolrich , 2017). This underscores the critical importance of exercising scrupulous deliberation and methodological precision when navigating the terrain where artificial intelligence intersects with intricate biological systems.

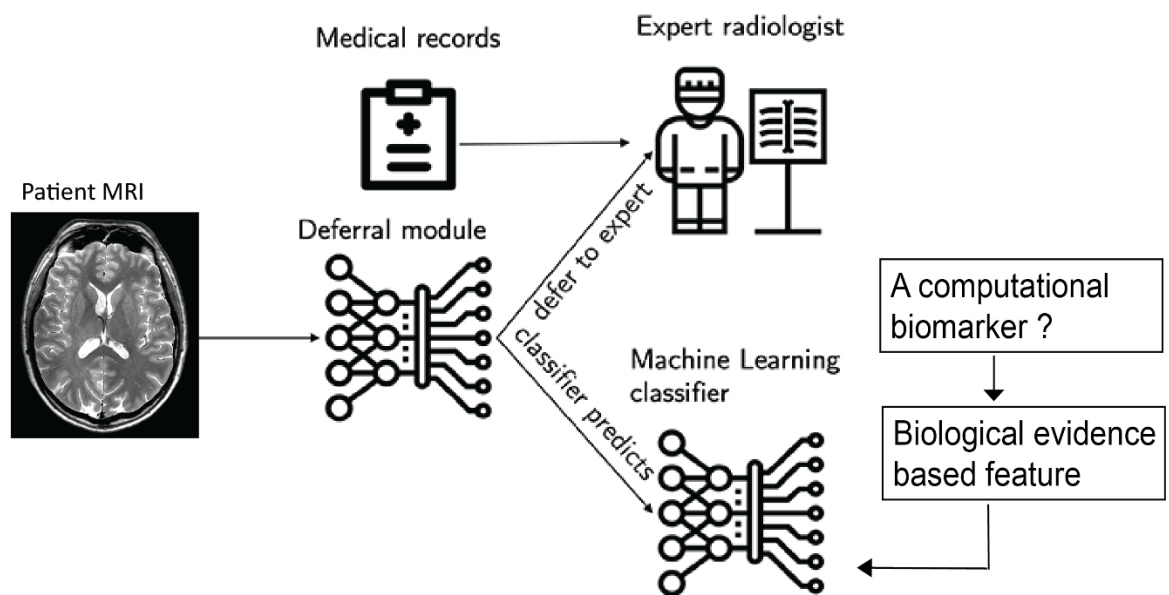


**Figure 1.2 A cartoon flowchart of two ways of diagnosis:** An expert radiologist and an AI model (ML or DL model). For AI modelling biological systems, it is imperative that the features, or perhaps computational biomarkers, are rooted in substantial biological evidence. (The figure is adapted and edited from Computer Science and Artificial Intelligence Lab. MIT – Mike Miliard 2023)

## 1.2 Part I: Brain connectivity patterns – An entry point

The human connectome comprises of functional and structural connectome. In part I, the thesis focuses on functional connectome where we explore data driven methodologies to investigate brain connectivity patterns, which presents a promising avenue for the identification of biological evidence-driven features. Within the domain of fMRI research, functional connectivity (FC) emerges as a promising approach for quantifying and characterising brain connectivity patterns (Preti, Bolton, & Van De Ville, 2017). Functional connectivity encompasses a statistical association forged between activity measurements procured from distinct brain regions. This statistical relationship is usually estimated through methodologies such as the pairwise Pearson correlation and gauges the extent of correlation within the Blood Oxygen Level Dependent (BOLD) time series from



distinct brain regions (Friston K. , Frith, Liddle, & Frackowiak, 1993). This metric sheds insights on the functional coupling and interconnectedness between proximal and distal brain regions, which play pivotal roles in the neural processing of resting state and tasks (Aertsen, Gerstein, Habib, & Palm, 1989) (Friston K. , Frith, Liddle, & Frackowiak, 1993). In traditional methodologies, functional connectivity has been computed by assessing brain connectivity patterns over the entire duration of the time series data. This involves the averaging of brain activity across time intervals. This approach is commonly referred to as *Static Functional Connectivity* (1.3 A). While studies conducted under this premise have yielded significant advancements in comprehending the broader properties of brain function, the resultant characterization inherently encapsulates an average representation across intricate spatio-temporal phenomena (Hutchison , et al., 2013). In recent times, it has come to light that functional connectivity exhibits temporal fluctuations, indicating that assessments based on the assumption of stationarity throughout the entire scan might be overly simplistic, potentially failing to capture the comprehensive spectrum of resting-state and task activity (Prete, Bolton, & Van De Ville , 2017). These spontaneous temporal fluctuations of FC which has been shown to contain relevant information is known as dynamic functional connectivity. Interpreting temporal fluctuations in FC metrics, such as correlations derived from fMRI time series, presents a nuanced challenge. This task is complicated by factors such as low signal-to-noise ratio (SNR), dynamic shifts in non-neural noise levels (arising from processes like cardiac and respiratory activities, as well as hardware instability), and fluctuations in both the mean and variance of the BOLD signal across time. The most commonly used method to estimate dFC is using the sliding window framework (Figure 1.3B), which estimates

dFC by computing average FC over small windows of time, and subsequently sliding the window over the entire duration of the BOLD time series (Hutchison & et al, 2013). Although, the sliding window approach has been the most common, simple, and intuitive analysis strategy for estimating dFC (Kudela, Harezlak, & Lindquist, 2017) (Prete, Bolton, & Van De Ville , 2017), the method suffers from prominent drawbacks. Arbitrary choice of window length, inherent variation present in the estimate that can be confused with the empirical time-varying nature of FC, equal weighting of all observations within the window leading to spurious fluctuations being magnified – all add to the woes of sliding window based approach (Lindquist, Xu, Nebel, & Caffo, 2014) (Hindriks, et al., 2016) (Prete, Bolton, & Van De Ville , 2017). Over the years, many meaningful extensions have been suggested to improve sliding window approach. Independent component analysis (ICA) was used to decompose windowed BOLD time series (Kiviniemi, et al., 2011). Several graph theoretical summary measures such as assortativity, modularity, efficiency offer promising avenues to extract information from dFC (Bullmore & Sporns, 2009). In addition, clustering algorithms such as K-means clustering (Damaraju, et al., 2014) (Allen E. , et al., 2014), hidden Markov models (HMM) (Vidaurre, Smith, & Woolrich, 2017), temporal ICA (TICA) (Yaesoubi, Miller, & Calhoun, 2015) allows to identify clustering-derived recurring connectivity patterns or dFC states. Several conceptual alternative strategies such as wavelet transform coherence (Chang & Glover, 2010), a time/frequency analysis strategy with an observation window for the frequency content of the time courses; and frame-wise analysis of the BOLD time series (Cabral, et al., 2017), which allows information to be retrieved from the observation of single frames and yield

temporally subsequent co-activation maps (Liu, Chang, & Duyn, 2013); have been suggested (see (Preti, Bolton, & Van De Ville, 2017) for a review).

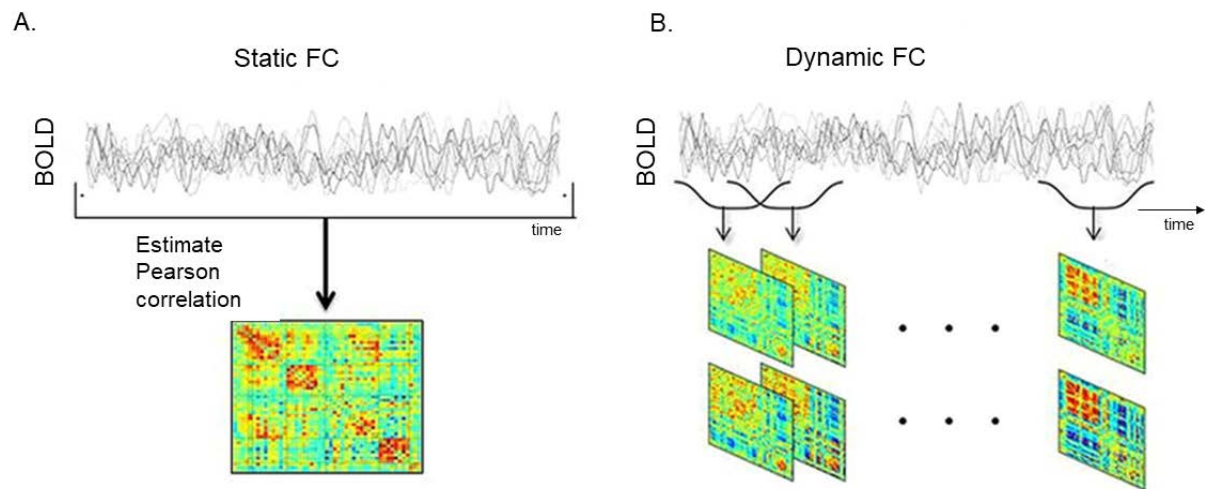


**Figure 1.3 Overview of static FC and Dynamic FC estimation.** (A) Static functional connectivity involves the averaging of brain activity across time intervals by calculating Pearson correlation over the entire duration of the scan. There is one FC matrix for the entire duration of the scan (B) Sliding window approach to estimate dynamic FC involves computing average FC over small windows of time, and subsequently sliding the window over the entire duration of the BOLD time series.

### 1.3 Functional connectome: dynamics and stability

Despite the inherent limitations, dynamic functional connectivity (dFC) possesses the capability to capture the intricate fluctuations within FC metrics, thereby encapsulating meaningful insights on a fine-grained temporal scale (Hutchison, et al., 2013). Acknowledging these temporal variations is pivotal for comprehending intricate behavioural dynamics. However, it is essential to recognize that alongside these fluctuations, a stable representation of neural activity's information content, along with the corresponding stability of FC patterns over time, assumes a crucial role for survival (Li, Lu, & Yan, 2019). This stable representation forms the bedrock for effective cognitive and behavioural functioning. The quantification of temporal

stability within dynamic functional connectivity (dFC) patterns constitutes a pivotal endeavour in studies focused on the intricate interplay between resting-state and task-related brain dynamics (Li, Lu, & Yan, 2019). Viewed from the context of dynamical systems, there is strong evidence for the existence of stability patterns of FC (Deco, Jirsa, & McIntosh, 2011). The resting-state functional connectivity that emerges attains optimal concordance with experimentally observed functional connectivity when brain networks function at a critical cusp of instability. This regime of near-critical conditions manifests in the emergence of resting-state BOLD networks featuring slow fluctuations ( $< 0.1$  Hz), which is presented as structured noise fluctuations around a stable equilibrium characterized by low firing activity. This equilibrium state coexists with latent "ghost" multistable attractors (Deco & Jirsa, 2012). Recent work has further demonstrated that during spontaneous resting state activity the ghost attractors makes frequent excursion to functionally and behavioural relevant phase locking states in a low dimensional state space (Vohryzek, Deco, Cessac, Kringelbach, & Cabral, 2020). Even in task, brain resides in a specific attractor state defined by a certain FC pattern according to the cognitive demands of the task (Fedorenko & Thompson-Schill, 2014) (Pillai & Jirsa, 2017). An overall increase in FC stability has been reported in the presence of the task (Gonzalez-Castillo & Bandettini, 2018). Investigations pertaining to the stability of dynamic functional connectivity (dFC) in both resting-state and task-oriented contexts can be broadly classified into two perspectives. The first perspective encompasses studies that condense brain activity into discrete states through the utilization of clustering techniques such as the K-means clustering algorithm (Allen E. , et al., 2014) (Cabral , et al., 2017) (Figure 1.4A) or the Hidden Markov model (Viduarre, Smith, & Woolrich , 2017) (Surampudi, et al., 2018)

(Figure 1.4B). Temporal stability of FC is then estimated by measuring the "switching rate" between these brain states. The switching rate, also known as flexibility, quantifies how quickly a specific node transitions between different brain states. Higher flexibility suggests more frequent transitions, which leads to reduced temporal stability (Long , Lu, & Liu, 2023). Nevertheless, it is essential to acknowledge that these investigations, which operate under the presumption of multiple discrete brain states, are constrained by inherent methodological limitations associated with the employed clustering algorithm and the predefined determination of the number of states (Rakthanmanon T. , Keogh, Lonardi, & Evans , 2011) (Allen E. , et al., 2014). Conversely, the second perspective entails studies that perceive the temporal dynamics of dynamic functional connectivity (dFC) not as discrete brain states but as an uninterrupted continuum. These investigations scrutinize the global and regional dynamics of dFC by quantifying variability and similarity. For instance, (Zhang , et al., 2016) explore temporal stability of dynamic FC by evaluating FC variability through Pearson correlation. Similarly, other researchers in the field view dynamic FC as a stochastic trajectory and examine its overall global and local dynamics by employing metrics like dFCSpeed (Arbabyazd, et al., 2020). However, it is worth noting that despite these endeavours, a data-driven approach to comprehensively characterize temporal dynamics, viewing dynamic FC as a continuum, remains at an early stage of development.

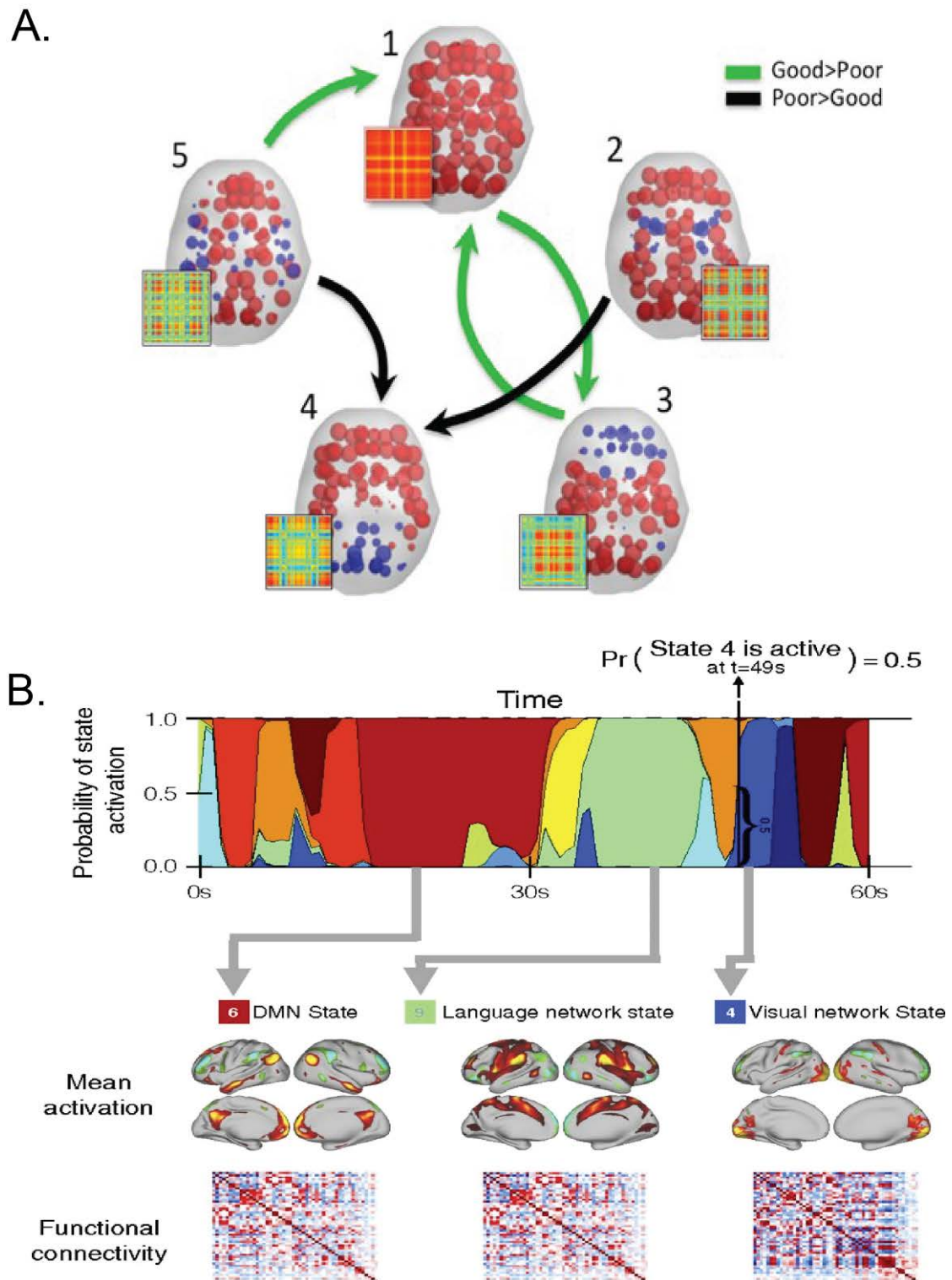


**Figure 1.4 Brief Summary of Brain State Studies** (A) (Cabral , et al., 2017) employ the K-means clustering technique to compress brain activity into discrete brain states. (B) (Vidaurre, Smith, & Woolrich, 2017) utilize Hidden Markov Model (HMM) clustering to achieve a similar compression of brain activity into discrete brain states.

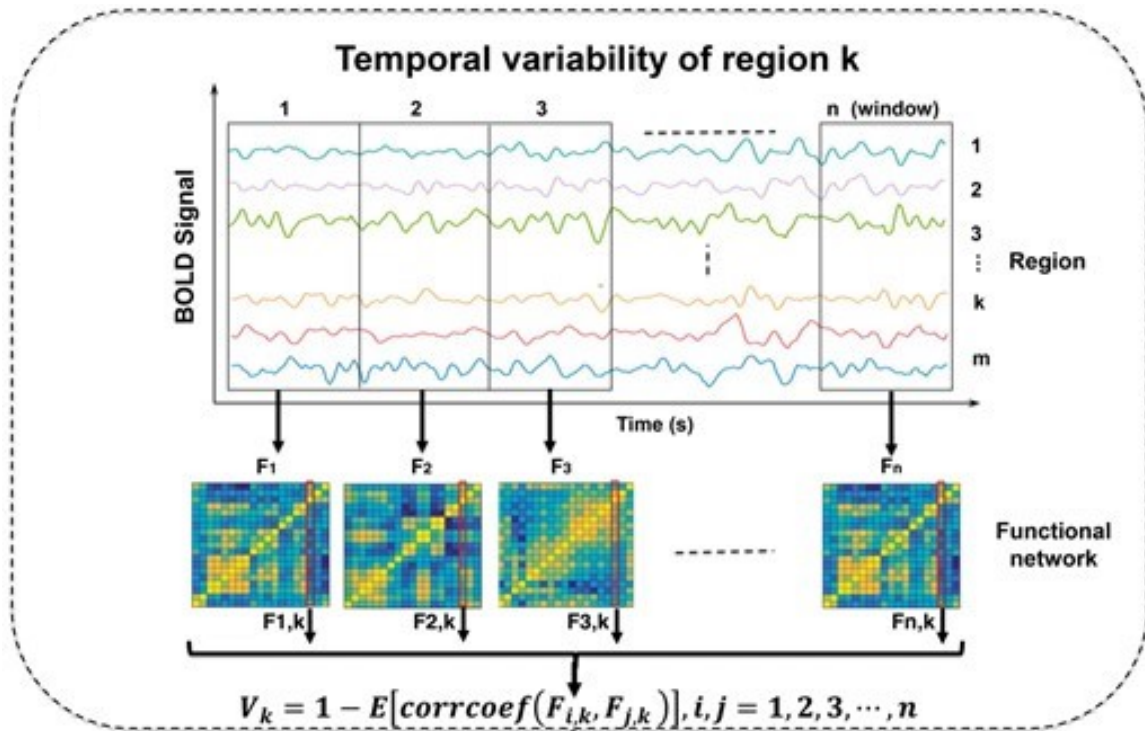


**Figure 1.5 Overview of temporal variability of brain networks.** (Zhang , et al., 2016) view the temporal dynamics of dynamic functional connectivity (dFC) as a continuous process, without segmenting it into discrete brain states and use pearson correlation to gauge the variability in temporal dynamics.

## 1.4 Part II: Low field neuroimaging – Fresh perspectives

Part II of the thesis is dedicated to the exploration of data-driven and machine/deep learning methodologies aimed at enhancing the image quality of magnetic resonance (MR) images acquired using low-field MRI systems. This study is part of an ongoing larger comprehensive international collaboration study funded by the Bill and Melinda Gates Foundation (BGMF) (Artificial Intelligence Methods for Low Field MRI Enhancement - INV-032788).

Magnetic resonance imaging (MRI) has ushered in a revolutionary era in brain research by providing non-invasive, high-resolution neuroimaging capabilities coupled with versatile soft-tissue contrast. In the realm of non-invasive human anatomy evaluation and understanding of physiological processes, particularly in

the domain of brain assessment, MRI holds a preeminent position. It is an invaluable tool for unravelling the intricate intricacies of neurology (Fornito , Zalesky , & Breakspear, 2015). However, despite these achievements, the complete realization of MRI's clinical potential remains pending. A significant impediment stems from the substantial size of MRI scanners and their intricate infrastructural requirements, which translate into formidable financial barriers for installation and operation. Consequently, this challenge restricts the widespread incorporation of MRI technology in regions with limited resources, notably in low- and middle-income countries (LMICs), where the burden of neurological disorders is particularly pronounced.

The challenge at hand appears to be relatively straightforward: MRI scanners, especially high-quality ones like the 3T machine, come with a significant financial burden. The installation and setup costs of these machines can amount to a substantial sum, which poses difficulties for lower and middle-income countries like India. As an alternative, low-field MRI scanners have emerged as an option. These scanners utilize a significantly lower magnetic field strength, typically in the order of milliteslas (mT), which reduces the overall cost of the equipment. However, this approach comes with a trade-off: the diminished magnetic power results in lower quality MRI images. To put it in perspective, if we liken 3T MRI images to 720p resolution, low-field MRI images are akin to subpar 240p resolution. Herein lies the inquiry: Is it feasible to enhance the quality of MRI images utilizing existing deep learning models? Can software be harnessed to address this challenge? This is the precise undertaking we have embarked upon. This ambitious project is generously supported by the Bill and Melinda Gates Foundation, aiming to leverage cutting-edge deep learning techniques to ameliorate the image quality of



MRI scans acquired using low-field MRI scanners. Existing methodologies in the field of deep learning use the technique of Image Quality transfer. This technique achieves super-resolution of scans by acquiring knowledge from higher-resolution images and then applying it to enhance the quality of their lower-resolution counterparts. IQT has predominantly found application in synthesizing 1mm isotropic images from thicker-slice clinical scans acquired at 1.5T magnetic field strength (Iglesias , et al., 2021). Moreover, this technique has demonstrated its utility in generating submillimetre-resolution images from 3T scans, harnessing insights gleaned from ultra-high-field (7T) imaging (Quiyuan , et al., 2021). An alternative approach involves the pre-emptive removal of image artifacts to bolster robustness and efficiency. This method capitalizes on a data-driven, machine learning-based denoising technique known as "non-local means-based denoising." This technique operates by reducing noise within the MR image, consequently elevating the overall image quality. In the context of our ongoing project, we delve into the exploration of these two methodologies: Image quality transfer and the utilization of the non-local means algorithm. These techniques serve as our investigative tools to enhance the quality of hyperfine low-field images obtained in regions characterized by lower- and middle-income economies.

## **1.5 Clinical Significance**

The convergence of artificial intelligence and neuroimaging analytics, encompassing both structural and functional connectivity analysis, holds immense potential in addressing a diverse spectrum of neuropathological disorders by serving as accurate diagnostic markers. Functional connectivity analytics, for instance, provide a promising avenue for the development of non-invasive tools

and markers to enable precise diagnoses of various brain disorders. This holds particular significance for common mental disorders such as schizophrenia, depression, attention-deficit-hyperactivity disorder, and autism, which exert significant societal impact and deeply affect patients and their caregivers. Pioneering studies such as (Wu , et al., 2023), (Zhang & et al, 2016) underscore the synergy between machine learning techniques and the assessment of brain connectivity stability, leading to the identification of patients experiencing cognitive motor dissociation (CMD). Other notable investigations like (Iglesias , et al., 2021) (Chengyuan , et al., 2021) delve into the utilization of deep learning models and structural connectivity markers to identify neuro-pathologies, including lesions and enhancements in T1-weighted (T1w) images. The potential for these connectivity-based markers to also serve as predictive indicators for these disorders presents an intriguing avenue for future research (Chengyuan , et al., 2021). By collectively enhancing our comprehension of brain connectivity patterns, particularly markers derived from the functional connectome, and advancing the development of deep and machine learning tools, we can pave the way for early identification, diagnosis, and ongoing monitoring of a wide array of neuropathological disorders. This interdisciplinary approach holds the promise of significantly improving clinical outcomes and patient care.

## **1.6 Summary and scope of the thesis**

Artificial Intelligence (AI), exemplified by advancements like ChatGPT and DALL-E, represents a transformative force permeating various aspects of life. One prominent domain for AI's application is healthcare, especially in diagnostics. This thesis delves into the applications of AI in the human brain, encompassing both its

structural and functional connectome. The effectiveness of AI's predictions heavily relies on robust input features, particularly when dealing with intricate systems like the brain. In this context, it becomes crucial for these features to be firmly grounded in well-established biological evidence. When rooted in biological evidence, these features enable the model's predictions to closely align with observed outcomes within the biological systems it aims to replicate. Notably, in functional connectomics, brain connectivity patterns offer a promising avenue for identifying input features guided by biological evidence. Dynamic functional connectivity has emerged as a prominent tool for studying brain connectivity patterns, with recent emphasis on their temporal stability. Developing a data-driven methodology for studying brain connectivity patterns, free from data biases, holds paramount importance. In the realm of structural connectomics, the utilization of machine learning and deep learning models to enhance the image quality of low-field MRI scans carries significant importance, especially for lower and middle-income countries. These advancements have the potential to substantially improve image quality, thereby positively impacting medical diagnostics and research within these regions. The objectives of this thesis are as follows:

- (1) To accurately characterize the stability of whole-brain dynamic functional connectivity patterns in both task and rest states across a cross-sectional population spanning the human adult lifespan (18-88 years). This will be achieved by developing a novel data-driven approach. The goal is to identify contributors (sub-networks) that influence the temporal stability of dynamic functional connectivity within the resting human brain. Additionally, the study aims to explore how these sub-networks organize and evolve throughout the lifespan.

- (2) To investigate the potential of whole-brain and sub-network level measures of dynamic functional connectivity as tools for characterizing common mental disorders, encompassing healthy individuals as well as those diagnosed with schizophrenia, bipolar disorder, and ADHD. Furthermore, the study seeks to comprehensively understand the disrupted brain network mechanisms associated with these disorders. This will be accomplished by combining community-based detection and dynamics-driven characterization of the functional connectome.
- (3) To customize and execute machine and deep learning-driven image quality transfer techniques, particularly employing methodologies such as SynthSR (Iglesias et al., 2021). The study's secondary objective involves adapting and implementing data-driven denoising algorithms, including the non-local means algorithm, on empirical hyperfine MR T1-weighted images. Additionally, the study aims to develop quality metrics capable of quantitatively evaluating the extent of image enhancement achieved through these adapted methodologies.

## Chapter 2

# Temporal stability in resting state, movie watching and sensorimotor task across healthy ageing

### 2.1 Introduction

Aging is typically associated with substantial structural and functional modifications of the brain. Significant number of studies which have investigated age-related modifications in functional networks using static functional connectivity reveal, an overall increase in between-network connectivity and decrease in within network connectivity in older adults (Damoiseaux, et al., 2008) (Betzal, et al., 2014) (Cao, et al., 2014) (Chen, et al., 2021). Recently, dynamic functional connectivity (dFC) has emerged as a major topic in the resting-state BOLD fMRI literature. In spite of inherent limitations (Prete, Bolton, & Van De Ville , 2017) , dFC captures the fluctuations in temporal scale of minutes which contain meaningful information (Hutchison & et al, 2013). While accounting for these fluctuations maybe important for understanding the itinerant nature of slow neuronal dynamics, stable representation of information of neural activity and corresponding stability of FC patterns over time is crucial for survival (Li, Lu, & Yan, 2019). Secondly, what are the key contributors that shapes stability of FC patterns in ongoing brain dynamics is a vital issue that needs resolution.

Recent evidence suggests FC stability increases with motor learning (Yu, Song, Huang, Song, & Liu, 2020), was significantly higher in patients with major depressive disorder (Demirtas, et al., 2016), decreases in patients of schizophrenia and their siblings (Guo, Zhao, Tao, Liu, & Palaniyappan, 2017). Previous studies exploring temporal dynamics of FC have tried to investigate the stability by calculating the correlation between FC matrices computed from successive temporal windows (Hansen, Battaglia, Spiegler, Deco, & Jirsa, 2015), characterizing variability of the functional connectivity profile of a given region across time (Zhang & et al, 2016) (Guo, Zhao, Tao, Liu, & Palaniyappan, 2017), by estimating voxel level dFC maps using Kendall's coefficient of concordance with time windows as raters (Li, Lu, & Yan, 2019), by estimating the standard deviation of global modularity averaged across all timepoints and all participants (Hilger, Fukushima, Sporns, & Fiebach, 2019).

Further, studies have also explored modifications in temporal stability of functional architecture in resting state of healthy control and patients with psychiatric disorders, and different battery of tasks. Zhang and colleagues showed disorder specific (ADHD, schizophrenia, autism spectrum disorder) variability modifications in functional architecture of DMN, visual and subcortical regions of the brain (Zhang & et al, 2016). Increased functional stability in high-order visual regions during naturalistic movie watching task were identified (Li, Lu, & Yan, 2019), but these studies are limited to stability of FC of a given region.

The temporal stability of functional architecture is shown to influence the relationship between resting state and task-related brain dynamics as well (Li, Lu, & Yan, 2019). Spontaneous brain activity during rest is not random and shows specific spatio-temporal organization in state space (Deco, Jirsa, & McIntosh,

2011). (Deco & Jirsa, 2012) speculate the existence of a multistable attractor landscape that describes the dynamic repertoire of resting state. Brain resides in a specific attractor state defined by a certain FC pattern according to the cognitive demands of the task (Fedorenko & Thompson-Schill, 2014) (Pillai & Jirsa, 2017). An overall increase in FC stability has been reported in the presence of the task (Gonzalez-Castillo & Bandettini, 2018). Thus, we hypothesised, unsupervised dFC characterization will reveal task-specific dFC stability patterns that are local in time i.e., limited, abated spread of stability patterns, whereas for the resting state dFC patterns, these functional states are composed of non-local correlations in time, with more global, widespread stability patterns. Although previous studies have explored the association between dynamic functional connectivity and age (Viviano, Raz, Yuan, & Damoiseaux, 2017) (Chen, et al., 2017) (Xia, et al., 2018), how the stability of functional architecture modifies across lifespan ageing remains an open question. Further, the age-related changes in temporal stability across resting state networks needs to characterised.

The aim of the present study is two-fold: 1) to precisely characterise the stability of whole-brain dFC patterns during task and rest for a cross-sectional population over human adult lifespan (18-88 years) using a novel unsupervised approach 2) to identify the contributors (sub-networks) to dFC temporal stability in in resting human brain and how they organize over lifespan. This manuscript is organized as follows. First, we estimate BOLD phase coherence over time (Glerean E. , Salmi, Lahnakoski, Jääskeläinen, & Sams, 2012) which was used as a measure of dFC for rest and task. Next, we proceed with unsupervised characterization of dFC subspaces involved in task and rest. Subsequently, the temporal stability of dFC subspaces were computed using two different measures - angular separation and

the Mahalanobis distance (Mahalanobis, 1930) (Shen, Kim, & Wang, 2010). Finally, we analyse the temporal stability of dFC to draw critical insights about age associated differences to task and rest using a large human cohort (N= 645) of healthy ageing (Shafto, et al., 2014).



## 2.2 Methods

### 2.2.1. Data sources and participants

The data were collected as part of stage 2 of the Cambridge Centre for Ageing and Neuroscience (CamCAN) project (available at <http://www.mrc-cbu.cam.ac.uk/datasets/camcan>) (Taylor, et al., 2017) (Shafto, et al., 2014). The CamCAN is a large-scale multimodal, cross-sectional, population-based study. The database includes raw and pre-processed structural magnetic resonance imaging (MRI), resting state and active tasks using functional MRI (fMRI) and Magnetoencephalogram (MEG), behavioural scores, demographic and neuropsychological data. From 3000 participants of stage 1, a subset of approximately 700 participants who were cognitively healthy (MMSE score >25), with no past or current treatment for drug abuse or usage, met hearing threshold greater than 35 dB at 1000 Hz in both ears, had at least a corrected near vision of 20/100 with both eyes and could speak English language (native English speaker or bilingual English from birth) were eligible for MRI scanning. They were home interviewed and recruited to stage 2. The study was in compliance with the Helsinki Declaration and was approved by the Cambridgeshire 2 Research Ethics Committee. The fMRI data from resting state and task periods (naturalistic movie watching and sensorimotor task) was used in the present study.

### 2.2.2 Data acquisition and experimental paradigm

The fMRI data were collected at MRC Cognition and Brain Sciences Unit, on a 3T Siemens TIM Trio scanner with a 32-channel head coil, the head movement was restricted with the aid of memory foam cushions. For the tasks, the instructions and visual stimuli were back projected onto the screen, auditory stimuli were presented via MR-compatible Etymotics headphones and manual responses from the participants made with the right hand were recorded using an MR-compatible button box (Taylor, et al., 2017). The fMRI data for eyes-closed resting state and sensorimotor task were acquired using Echo-Planar Imaging (EPI) sequence, consisted of 261 volumes, each volume with 32 axial slices (slice thickness 3.7mm, interslice gap 20% for whole-brain coverage) acquired in descending order, TR 1970 ms, TE 30 ms, voxel-size 3 mm 3 mm 4.44 mm, Flip angle 78 degrees, field-of-view 192 mm X 192 mm, Bandwidth 2232 Hz/Px. The duration of both the scans was 8 min 40s. The fMRI data for the naturalistic movie watching task were acquired using multi-echo EPI sequence, consisting of 193 volumes of 32 axial slices each (slice thickness 3.7mm, interslice gap 20% for whole brain coverage) acquired in descending order, TR 2470 ms, TE [9,4,21.2,33,45,57] ms, voxel-size 3 mm 3 mm 4.44 mm, Flip angle 78 degrees, field-of-view 192 mm X 192 mm, Bandwidth 2520 Hz/Px. The duration of the scan was 8 min 13s. A detailed description of data acquisition parameters can be found in (<https://camcan-archive.mrc-cbu.cam.ac.uk/dataaccess/>) (Taylor, et al., 2017).

The task-induced BOLD data from the naturalistic movie watching task was acquired from participants, who watched 8 minutes of narrative preserved, condensed, black and white version of Alfred Hitchcock's television drama "Bang! You're Dead". The participants were not aware of the title of the movie but were

instructed to pay attention to the movie. In the sensorimotor task, the trials consisted of a binaural tone simulation at either 300, 600, or 1200 Hz and bilateral black and white checkerboard. The participants were asked to button press with their right index finger if they hear or see any stimuli. More details about the task paradigm have been presented here (Shafto, et al., 2014) (Taylor, et al., 2017).

### 2.2.3 Data pre-processing

The fMRI data for each functional run (resting state, movie watching and sensorimotor task) were unwarped using field-map images, realigned to correct for motion and, slice-time corrected. EPI data were co-registered to the T1 image, transformed to MNI space using the warps and affine transformation from structural image (estimated using DARTEL). For region of interest (ROI) analysis, mean regional BOLD time series were estimated in 116 parcellated brain areas of Anatomical Automatic Labelling atlas (AAL) (Tzourio-Mazoyer, et al., 2002) (available at <http://www.gin.cnrs.fr/tools/aal>). Pre-processed data was provided by Cam-CAN research consortium. Detailed overview of pre-processing pipeline can be found in (Taylor, et al., 2017). In order to capture the pattern of temporal stability over lifespan (e.g.: of the 'Entropy' metric), we divided the whole dataset of N=645 participants into non-overlapping bins of 5 years starting from 18 years. On the other hand, to gather accurate insights in each stage of the adult lifespan, we divided the whole data of N=645 participants into three cohorts, young adults with an age range 18-40 years (50.27 % female; mean age=31.21±6.06 years), middle adults with an age range 41- 60 years (52.23% female; mean age = 50.49±5.70 years), old adults with an age range 61-88 years (49.92 % female; mean age =

73.72±7.20 years)..Each participant's BOLD time series in the resting state, naturalistic movie watching and sensorimotor tasks were extracted.

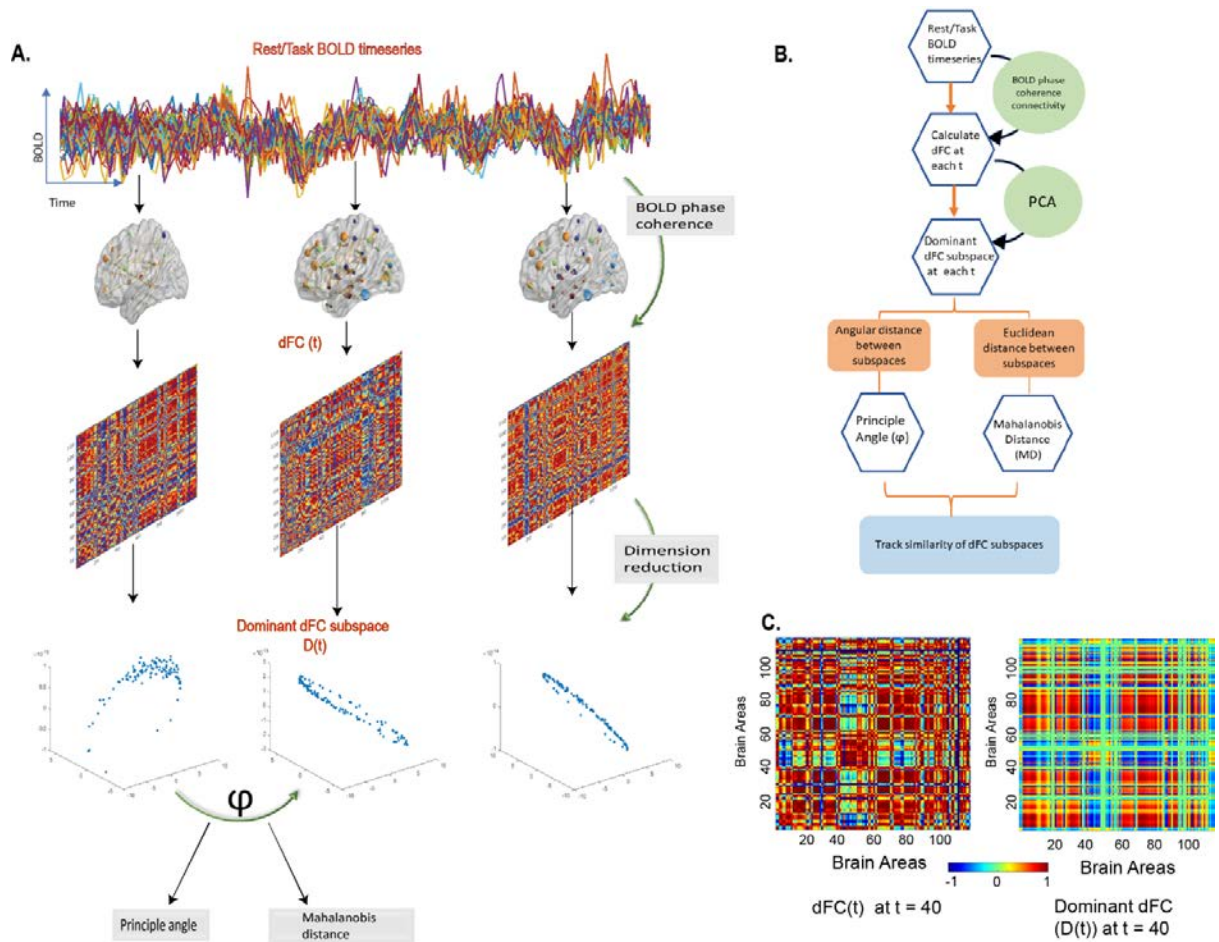


**Figure 2.1 Brief overview of the unsupervised approach** (A) The schematic diagram shows how the temporal stability of dynamic functional connectivity subspaces (dFC) are computed. Dominant dFC subspace, at each time point, is estimated using the first three principal components of dFC(t), that was computed using the measure of BOLD phase coherence. The similarity between dFC subspaces is calculated using Angular distance (principal angle) and Mahalanobis distance (Euclidean distance). If the dominant dFC subspaces are similar for extended timepoints, then they are considered to be stable. (B) A flowchart representation of the method (C) Matrix representation of dFC patterns (dFC(t)) and reduced Dominant dFC patterns (D(t)) at t=40.

## 2.2.4 Data analysis

### 2.2.4.1 Characterization of dynamic functional connectivity

Time-resolved dynamic functional connectivity (dFC) was estimated, for each individual, using BOLD phase coherence (Figure 2.1A) (Glerean E. , Salmi, Lahnakoski, Jääskeläinen, & Sams, 2012) (Ponce-Alvarez, et al., 2015) (Deco & Kringelbach, 2016) (Cabral, et al., 2017), which resulted in a matrix with size  $N \times N \times T$ , where  $N=116$  is the number of brain regions defined by AAL atlas,  $T$  is the total number of time points ( $T=261$  for resting state and Sensorimotor task,  $T=193$  for naturalistic movie watching task). We chose BOLD phase coherence instead of computing correlation over a sliding window to calculate dFC, because BOLD phase coherence is an instantaneous measure with maximum temporal resolution (Glerean E. , Salmi, Lahnakoski, Jääskeläinen, & Sams, 2012). BOLD phase coherence does not require time-windowed averaging, that generates biased estimates if the window length is short and reduces temporal resolution if the window length is longer (Glerean E. , Salmi, Lahnakoski, Jääskeläinen, & Sams, 2012).

First, the instantaneous phases  $\theta(n, t)$  of the BOLD time series for all the brain regions,  $n$ , was computed using Hilbert transform. The real-valued modulated BOLD signal  $s(t)$  is expressed as an analytical signal in the complex plane as:

$$z(t) = z_r(t) + jz_i(t) = s(t) + j HT[s(t)] \quad (2.1)$$

Where, (HT [\*]) represents the Hilbert transform. The instantaneous phase  $\theta(t)$  is computed as follows:

$$\theta(t) = \angle z(t) = \arctan \frac{z_i(t)}{z_r(t)} = \arctan \frac{HT[s(t)]}{s(t)} \quad (2.2)$$

Given the phases of the BOLD time series, phase coherence i.e.,  $dFC(n, p, t)$  for brain regions,  $n$  and  $p$  at time  $t$  is computed as:

$$dFC(n, p, t) = \cos(\theta(n, t) - \theta(p, t)) \quad (2.3)$$

when, the phases of BOLD signals,  $\theta(n, t)$ ,  $\theta(p, t)$  of the brain regions  $n, p$  are synchronized,  $dFC(n, p, t)$  (ranges from -1 to 1) is close 1, when the phases from the BOLD signals of brain regions  $n, p$  are orthogonal  $dFC(n, p, t)$  is close to 0. Since the phases are undirected,  $dFC(n, p, t)$  is symmetric along the diagonal.

In addition to this, to check for reliability, we compute dFC using a sliding-window approach (Hutchison & et al, 2013) with non-overlapping, gaussian windows, varying the window length (10, 20, 30 time points) (Supplementary information – (A 2.1, A 2.2., A 2.3)).

#### 2.2.4.2 Extracting Dominant dynamic functional connectivity

Principal component analysis (PCA) was applied to participant-wise  $dFC(n, p, t)$  matrix of size  $N \times N$  representing the FC between  $n$ th and  $p$ th brain area for each time point. PCA is an unsupervised, multivariate dimension reduction method that decomposes the data into a set of orthogonal principal components or leading eigenvectors sorted by their contribution to the overall variance (Friston, 1993). Thus,  $dFC(n, p, t)$  or simply  $dFC_t$  can be expressed as

$$dFC_t = V^T S V \quad (2.4)$$

where, matrix  $V$  of size  $N \times N$  are set of eigenvectors, with each column of  $V$  of size  $1 \times N$  representing orthogonal principal component, and  $S$  the diagonal matrix

$$\begin{pmatrix} \lambda_1 & \dots & 0 \\ \vdots & \ddots & \vdots \\ 0 & \dots & \lambda_N \end{pmatrix}, \text{ such that } \lambda_1 > \lambda_2 \dots > \lambda_N$$

If  $k$  is the number of principal components chosen to represent  $dFC$ , the corresponding subspace  $D(n, k, t)$  or  $D_t$ , representative of dominant dFC pattern, can be expressed as

$$D = \tilde{V}^T \tilde{S} \tilde{V} \quad (2.5)$$

where,  $\tilde{V}^T$  is a dimensionally reduced matrix of size  $N \times k$ ,  $\tilde{S}$  is a diagonal matrix

$\begin{pmatrix} \lambda_1 & \cdots & 0 \\ \vdots & \ddots & \vdots \\ 0 & \cdots & \lambda_k \end{pmatrix}$ . In this study, we chose  $k = 3$  because for all participants at least

99% variance in  $dFC$  matrix is captured by the 3 leading eigenvectors (**S 4**). The dimension of  $dFC(n, p, t)$  has been reduced to  $D(n, k, t)$ . Since, the  $dFC(t)$  matrices are symmetrical, several studies compare only the upper triangular elements (Cabral, et al., 2017). In our study, we use an alternative method, where we consider the first three leading eigen vectors, forming a reduced three-dimensional dominant dFC subspace ( $D(t)$ ) of each  $dFC(t)$ . Compared to considering all (upper triangular) the elements of  $dFC(t)$ , this method reduces the dimensionality of the of the data while still explaining almost 99% of the variance (A 2.4). This method of estimating  $dFC(t)$  also bypasses the use of sliding window approach to estimate dFC.

#### 2.2.4.3 Computation of stability of dynamic functional architecture

We seek to characterize the temporal stability of the dominant subspace  $D(n, p, t)$  (or referred to as simply  $D_t$ ) by estimating how similar they are across time  $t$ . To estimate the similarity between dominant dFC configurations, we introduce two types of distance measures successive dFC subspaces, 1) angular distance 2) Normalised Euclidean distance (Figure 2.1B). We define angular distance as the

principal angle between the dFC subspaces from different time points, given by the following equation:

$$\phi(t_x, t_y) = \angle(\mathbf{D}_{t_x}, \mathbf{D}_{t_y}) \quad (2.6)$$

Where, each entry in the time X time *temporal stability matrix*,  $\phi(t_x, t_y)$  is the principal angle between the two N X k dimensional subspaces at  $t_x$  and  $t_y$  (Banerjee A. , Pillai, Sperling, Smith, & Horwitz, 2012) ( Björck & Golub, 1973). The principal angle ranges between 0 (low angular distance) to  $\pi/2$  (high angular distance).

For each individual, we calculate the angular distance between dominant dFC subspaces at  $t_x$  and  $t_y$ , by estimating the principal angle between them. The low principal angle between dominant dFC subspaces means that their dFC configurations are very similar. On the contrary, the high principal angle between dominant dFC subspaces means that their dFC configurations are dissimilar.

We define the normalised Euclidean distance between dominant dFC subspaces by the Mahalanobis distance. Mahalanobis distance measures the distance between points in space 1 from space 2 with the following equation:

$$M^2 = (\mathbf{D}_{t_x} - \mathbf{D}_{t_y})^T \mathbf{C}^{-1}(\mathbf{D}_{t_x} - \mathbf{D}_{t_y}) \quad (2.7)$$

where  $M^2$  is the distance between each entry of  $\mathbf{D}_{t_x}$  and  $\mathbf{D}_{t_y}$ . For each timepoint, Mahalanobis distance was calculated between each ROI in the reduced dominant dFC subspace  $\mathbf{D}_{t_y}$  and whole-brain subspace  $\mathbf{D}_{t_x}$ . Every ROI in  $\mathbf{D}_{t_y}$  (point P) has Mahalanobis distance estimated with respect to subspace  $\mathbf{D}_{t_x}$  (distribution D). Subsequently, for each individual, we estimate the time X time *temporal stability*



*matrix*, where each entry is the Mahalanobis distance ( $M$  ranges between 0.5 to 2.5), averaged across all brain parcels. Low  $M$  means that dominant dFC subspaces are similar, high  $M$  means that the dFC subspaces are dissimilar. Figure 2.1C illustrates the Matrix representation of dFC patterns ( $dFC(t)$ ) and reduced Dominant dFC patterns ( $D(t)$ ).

### 2.2.1.1. Quantifying complexity of *temporal stability matrices*

#### *Entropy:*

To evaluate the informational content of *temporal stability matrices* we evaluated the entropy, for all three categories, rest, movie viewing and sensorimotor task in young and old adults. Entropy is defined by the following equation:

$$E = -\sum p \log(p) \quad (2.8)$$

where  $p$  contain the normalised histogram counts returned from 'imhist.m'. 'imhist.m' calculates the histogram of *temporal stability matrices*, estimated using reduced  $D_{t_x}$  and  $D_{t_y}$ , and returns histogram counts. We calculate entropy of *temporal stability matrices*, where each entry is angular distance or Mahalanobis distance estimated between reduced  $D_{t_x}$  and  $D_{t_y}$ , for each subject and condition. In our formulation, Entropy provides us a measure of distinguishable temporal order that can be interpreted as overall stability of the *temporal stability matrices*.

#### *Frobenius norm:*

Frobenius norm was used to measure the differences between the temporal stability matrices computed for rest and the task conditions. Frobenius norm, also called the Euclidean norm of a matrix, is defined as the square root of the sum of

the absolute squares of its elements. Here, we calculate Frobenius norm between temporal stability matrices with the following equation:

$$\|x_F\| = \sqrt{\sum_{i=1}^T \sum_{j=1}^T |a_{ij} - b_{ij}|^2} \quad (2.9)$$

where  $a_{ij}$  and  $b_{ij}$  are the entries in the temporal dynamic matrices of rest and any of the task conditions respectively (movie watching or sensorimotor).  $x_F$  is also computed between the two tasks.

### *Stochastic characterization of dFC*

The temporal variation of two measures, principal angle and Mahalanobis distance between the dominant *dFC* subspaces essentially capture the degree of temporal variation in functional network. Principal angular values close to  $\frac{\pi}{2}$  or high Mahalanobis distance at a specific time point reflects the reorganization of the functional state itself, whereas angular values closer to zero or low Mahalanobis distance indicates minor deviation from previous time. To understand the underlying stochastic characteristics of these measures, we use auto-regressive (AR) models where present values of  $\phi(t)$  and  $M(t)$  are modelled as a linear weighted sum of values from past  $\phi(t-1), \phi(t-2) \dots \phi(t-i)/M(t-1), M(t-2) \dots M(t-i)$ . The AR ( $\rho$ ) process,  $X_t$  ( $\phi(t)$  or  $M(t)$ ) is given by the following equation:

$$X_t = c + \sum_{i=1}^{\rho} \varphi_i X_{t-i} + \varepsilon_t \quad (2.10)$$

where  $\varphi_1 \dots \dots \dots \varphi_{\rho}$  are parameters of the model,  $c$  is a constant,  $\varepsilon_t$  is white noise and  $\rho$  is the lag term or model order. The simplest AR process is AR (0) is essentially a white noise process. In AR (1), the current value is dependant only

on its immediately preceding value, and hence captures a Markovian process. Optimal model of an AR process can be computed using the Akaike information criterion (AIC) which is expressed as

$$AIC(\rho) = -2L + 2\rho \quad (2.11)$$

where  $L$  is the likelihood function computed by summing up over the mean squared error for an AR model of order  $\rho$  (Wagenmaker & Farrell, 2004) (H.Akaike, 1974). Optimal model order can be selected at a value of  $\rho$  where AIC is minimum. We varied the model order ( $\rho$ ) from 0 to 100 and use the first minimal AIC value to select the best AR ( $\rho$ ), model. If the model order is found to be greater than 1, the underlying process is considered non-Markovian.

#### 2.2.5 Data/Code availability statement

The datasets generated during the analysis pipelines in the present study are available from the corresponding author on reasonable request. The codes for all the analysis carried out in this paper is available on <https://bitbucket.org/cbd/workspace/projects/DFC>

#### 2.2.6 Ethics statement

CamCAN dataset was collected in compliance with the Helsinki Declaration, and has been approved by the local ethics committee, Cambridgeshire 2 Research Ethics Committee (reference: 10/H0308/50)

## 2.3. Results

### 2.3.1. Dynamic functional connectivity (dFC) patterns during rest, continuous naturalistic movie watching, and discrete sensorimotor task.

We computed the *dFC* from parcellated BOLD time series of resting state, naturalistic movie watching task where the participants watched and listened to an excerpt from Alfred Hitchcock's "Bang! You're Dead", and a sensorimotor task where participants responded by a button press to either a visual or an auditory stimulus from the Cam-CAN dataset (details in Methods). Figure 2.2A represents dFC obtained using BOLD phase coherence connectivity in resting state. To capture the pattern of temporal stability over lifespan we divided the whole dataset of N=645 subjects into non-overlapping bins of 5 years starting from 18 to 88 years. Subsequently, to gather insights at each stage of adult lifespan we have divided the total N=645 subjects into three age groups -Young, Middle and Old with sufficient number of participants (> 180) in each category. We report the results of the analysis on young adults (age range 18-40) in this section.

Dominant dFC subspaces were obtained by applying the unsupervised approach of Principal Component Analysis (PCA) to BOLD time series at each time point, and then reconstructing either the task or rest as the dynamics of a reduced dimensional dFC subspace. To demonstrate, that the unsupervised characterization of dFC patterns indeed capture the functional brain network organization, we computed the differences between the temporal stability matrices of rest and the two task conditions; first using the measure of principal angle (Figure 2.2) and second using the measure of Mahalanobis distance (Figure 2.3). Thereafter, other measures of complexity and temporal variability were tested.

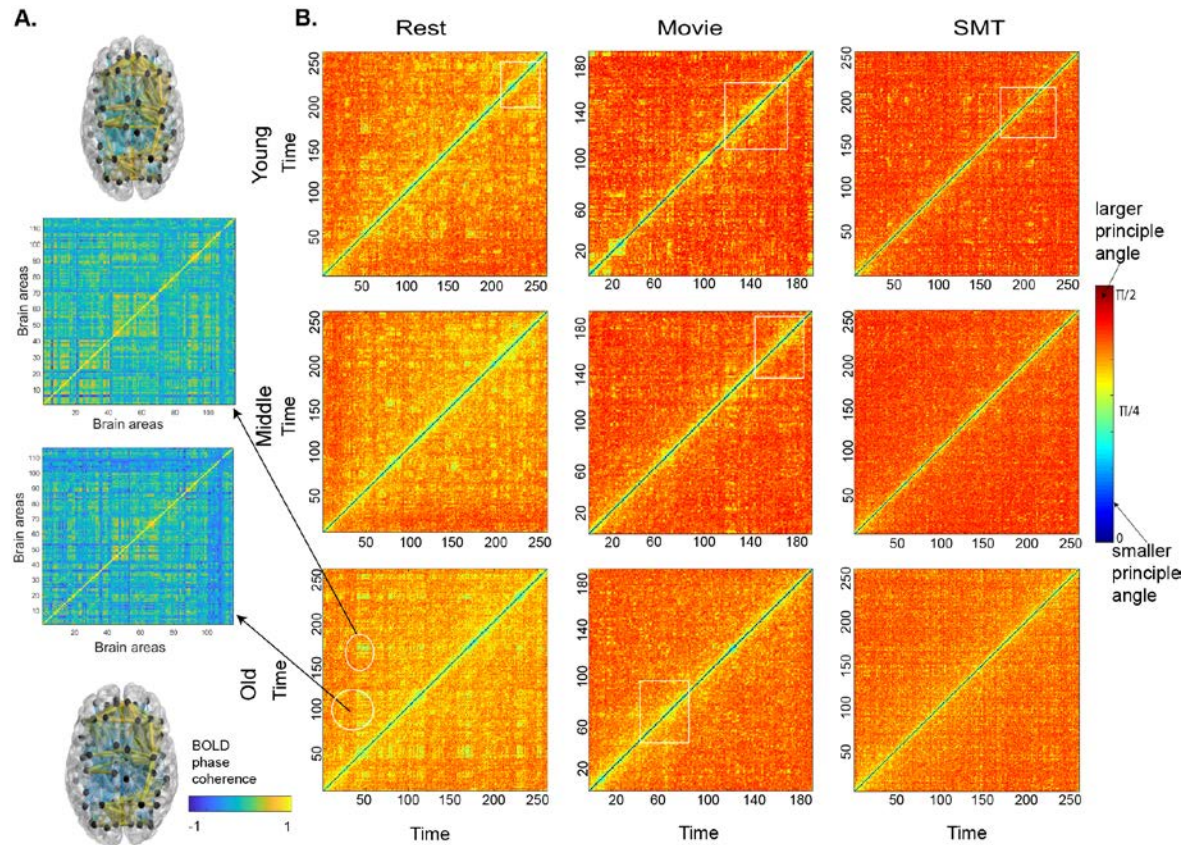


**Figure 2.2: Using angular distance to characterise temporal stability matrices across age** (A) dFC matrices estimated using BOLD phase coherence. (B) Time  $\times$  Time temporal stability matrix of resting state, naturalistic movie watching task and discrete, sensorimotor task for young, middle and old adults. Each entry in the matrix is the principal angle  $\phi(t_x, t_y)$  between dominant dFC subspaces at  $t_x$  and  $t_y$ . The principal angle ranges between 0 (low angular distance) to  $\pi/2$  (high angular distance). Resting state, in young, middle and old adults, has shorter-lived, global spread of patterns of temporal stability. On the contrary, both the tasks have a longer-lived, local spread of patterns of stability (indicated by arrows and rectangular boxes).



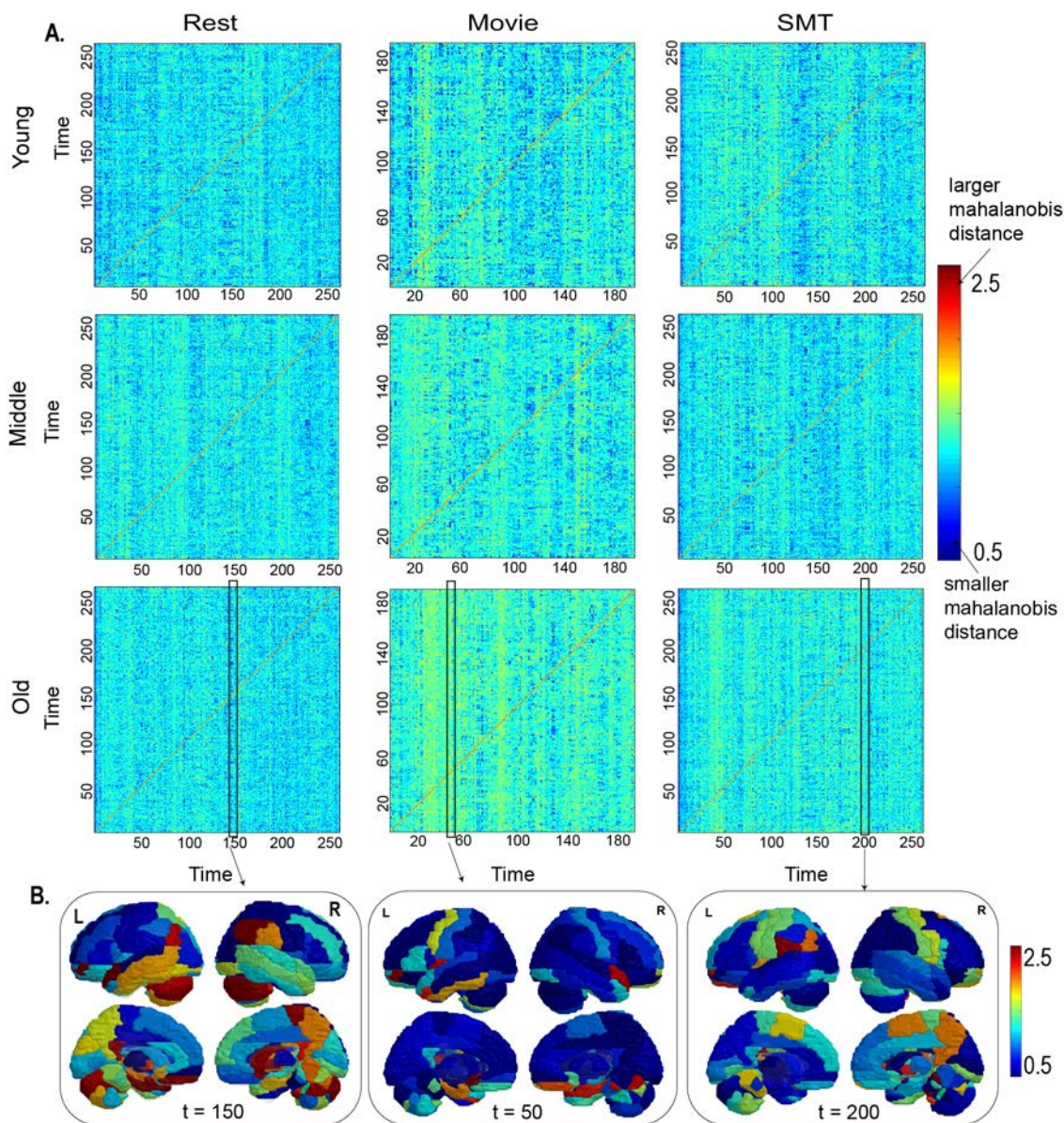


**Figure 2.3: Using Mahalanobis distance to characterise temporal stability matrices across age.** (A) Time X Time temporal stability matrix of resting state, naturalistic movie watching task, and sensorimotor task for young, middle and old adults, where each entry in the matrix is Mahalanobis ( $M^2(t_x, t_y)$ ) distance between the dominant dFC subspaces. Mahalanobis distance between dominant dFC subspaces is low when the dFC configurations are similar. (B) The profile of temporal stability estimated with Mahalanobis distance between dominant dFC subspaces at  $t=15$  and  $t=150$ ,  $t=50$ ,  $t=200$  across the brain regions.

### 2.3.1.1. Using angular distance to characterize temporal stability matrices

First, we calculate the principal angles among the dominant *dFC* subspaces generated across all time points. This resulted in time X time temporal stability matrix, averaged across all subjects, where each entry in the matrix is the angle between dominant *dFC* subspaces at  $t_x$  and  $t_y$ , as shown in Figure 2.2 B. We consider a dominant *dFC* configuration to be stable if the subsequent subspaces are similar in configuration, i.e., less “angular distant” for extended duration of time points. Results shown in Figure 2.2 B indicate that the resting state has a global spread of shorter-lived, repeated patterns of stability than both tasks. On the contrary, both the task cohorts, passive movie watching, and sensorimotor task, showed a local spread of, longer-lived stability patterns suggesting that local temporal stability of functionally connected networks are higher in the task than in resting state. To quantify these observations, we calculate the entropy of temporal stability matrices of resting state, movie watching task and sensorimotor task. The plots in Figure 2.4A, which represent entropy of temporal stability matrices of three categories of rest and task across lifespan, overall, report resting state to have the highest entropy, followed by movie watching task and sensorimotor task. We also calculate entropy of temporal stability matrices of young, middle and old age categories across resting state and both task cohorts (see A 2.5). Wilcoxon sign rank test revealed significant differences in entropy of temporal dynamic matrices of rest and task cohorts (details reported in supplementary material). Further, to analyse how similar temporal stability matrices across rest and tasks are, we calculate the Frobenius norm as shown in Figure 2.4C. The results reveal a shorter Frobenius norm between the temporal dynamic matrices of the resting state and movie watching task, than the resting state and sensorimotor task.

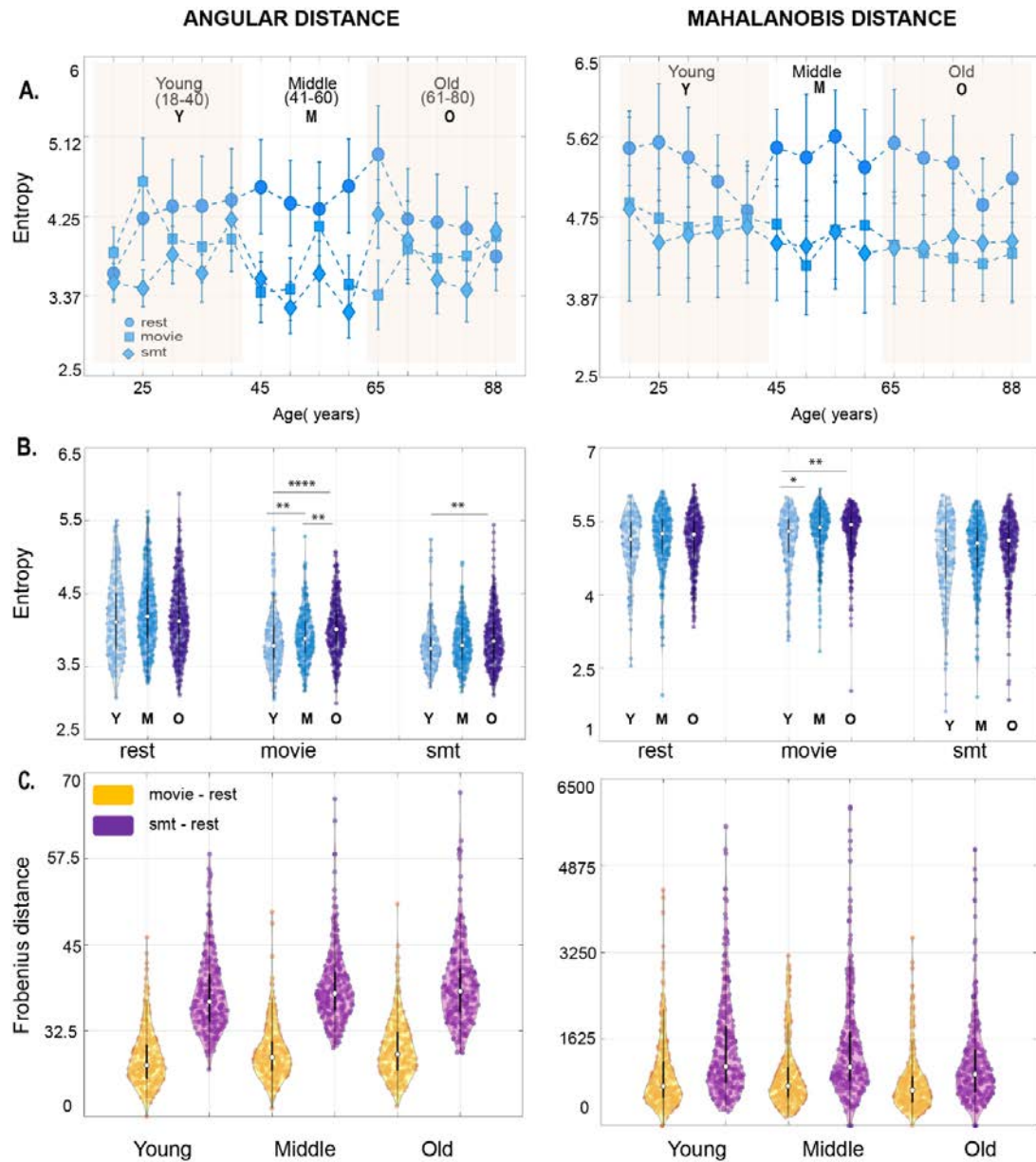


**Figure 2.4: Quantifying complexity of temporal stability matrices across age (A)** Plots representing entropy of temporal stability matrices of resting state (rest), naturalistic movie watching task (movie) and sensorimotor task (SMT) across lifespan, for Angular distance and Mahalanobis distance metric. The subjects were divided into non-overlapping bins of 5 years starting from 18 years to 88 years (18-20, 21-25, 26-30, 31-35, 36-40, 41-45, 46-50, 51-55, 56-60, 61-65, 66-70, 71-75, 76-80, 81-88). (B) Plots representing entropy of temporal stability matrices of resting state (rest), naturalistic movie watching task (movie) and sensorimotor task (SMT) for young (cyan), middle (blue) and old (pink) adults, for Angular distance and Mahalanobis distance metric. Statistically significant differences (uncorrected) are indicated using \* ( $P \leq 0.05$ ), \*\* ( $P \leq 0.01$ ), \*\*\* ( $P \leq 0.01$ ), \*\*\*\* ( $P \leq 0.0001$ ), ns (not significant). (C) Plots representing distribution of Frobenius distance between temporal stability matrices of resting state, naturalistic movie watching (yellow) and resting state, sensorimotor task (purple) for Angular distance, and Mahalanobis distance metric, in young, middle and old adults. The violin plots reveal a shorter Frobenius norm between resting state and movie watching task than resting state and sensorimotor task in all young, middle and old adults.



### 2.3.1.2. Using Mahalanobis distance to characterize temporal stability matrices

Alternatively, we evaluate the temporal stability of  $dFC$ , by estimating Mahalanobis distance, that resulted in a time X time temporal stability matrix. Each entry of this matrix is the Mahalanobis distance between dominant  $dFC$  subspaces. Results, as shown in Figure 2.3A and Figure 2.3B, reveal global, shorter-lived repeated patterns of temporal stability in resting state and local, longer-lived temporal stability patterns in both the tasks. The entropy results across lifespan (Figure 2.4A) reveal an overall high entropy in the resting state, followed by movie watching task and sensorimotor task. We repeat the Frobenius norm analysis, which produced similar results as the angular distance metric, as shown in Figure 2.4C.

### 2.3.2. Unsupervised characterization of $dFC$ across healthy lifespan ageing

Next, we have included three age cohorts, young, middle and old adults from the Cam-CAN dataset and carried out unsupervised characterisation of  $dFC$  using participant's resting state, movie watching, and sensorimotor task data to identify age associated alterations in temporal stability of dominant  $dFC$  subspaces.

#### 2.3.2.1. Using angular distance to quantify temporal stability differences in $dFC$ across healthy ageing

The time X time temporal stability matrix was computed for the middle (age range 41-60 years) and older cohort (age range 61-88 years) and compared with that of younger cohort computed in the section 3.1. A global spread of shorter duration of temporal stability patterns was observed in resting state and local spread of longer duration temporal stability patterns was observed in the task, in all young, middle and old adults (see Figure 2.2 B). Further, entropy analysis revealed (see Figure 2.4B), in movie watching and sensorimotor task, a peak entropy in older adults,

followed by middle and young adults. Whereas in resting state, we observed peak entropy in middle adults, followed by older adults and their younger counterparts. The distributions were non-parametric (normality check was done with Jarque-Bera test and D'Agostino-Pearson omnibus test), Wilcoxon rank sum test revealed significant differences in entropy values between young and middle adults ( $p=0.0073$ ), middle and old adults ( $p=0.0017$ ) and, young and old adults ( $p=2.24e-08$ ) in movie watching task and young and old adults ( $p=0.0019$ ) in sensorimotor task. The Frobenius norm analysis as shown in (Figure 2.4C) also revealed a similar trend in young and old adults i.e., shorter Frobenius norm between resting state and movie watching task than resting state and sensorimotor task

#### 2.3.2.2. Using Mahalanobis distance to quantify temporal stability of dFC across healthy ageing

Mahalanobis distance between dominant dFC subspaces showed patterns similar to principal angle in young, middle and elderly. Further, we calculate entropy as shown in Figure 2.4B, of temporal stability matrices of each age category, in both rest and task conditions. The results indicate peak entropy in older adults, followed by middle and young adults in movie watching and sensorimotor task and, peak entropy in middle adults, followed by old and young adults in resting state, a similar trend as the angular distance metric. The distributions were non-parametric (normality check was done with Jarque-Bera test and D'Agostino-Pearson omnibus test). Wilcoxon rank sum test revealed statistical significance between the entropy of temporal stability matrices of young and middle adults ( $p=0.0176$ ), young and older adults ( $p=0.0063$ ) in movie watching task. Frobenius norm analysis as shown in Figure 2.4C revealed a shorter Frobenius norm between resting state and movie watching task than resting state and sensorimotor task.

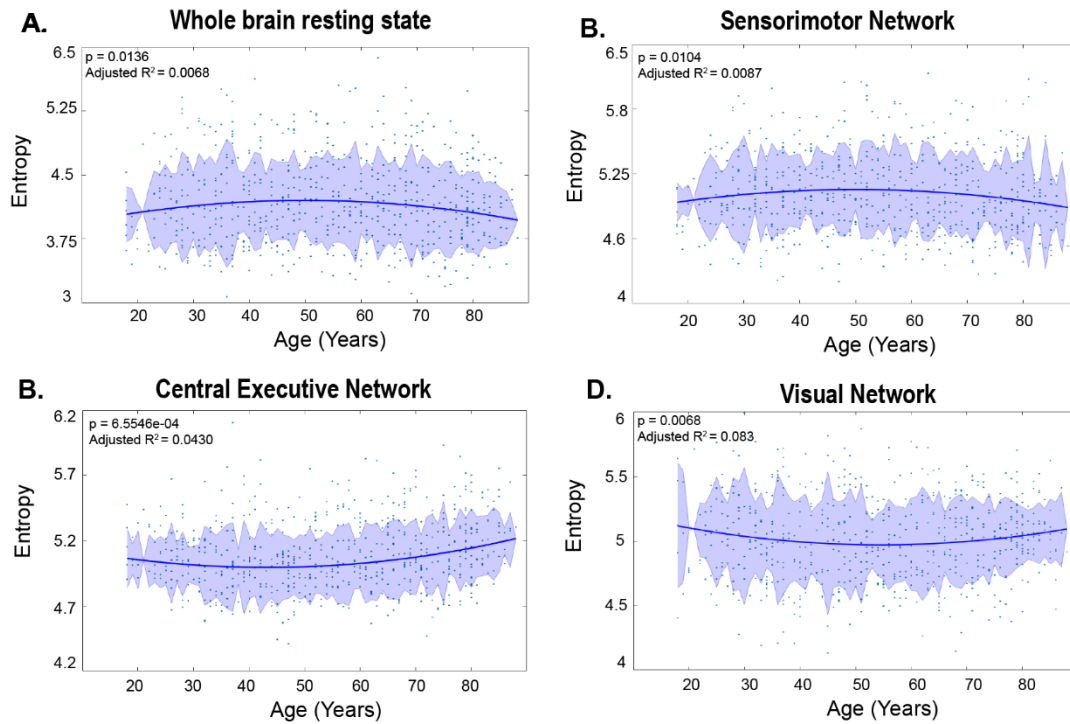


**Figure 2.5: Age related changes in temporal stability of dynamic functional connectivity of whole-brain resting state (A), sensorimotor network (B), central executive network (C) and Visual network (D) estimated with angular distance metric. Only those networks with significant modifications in temporal stability with age are shown. Statistically significant differences (uncorrected) are indicated using \* ( $\mathcal{P} \leq 0.05$ ), \*\* ( $\mathcal{P} \leq 0.01$ ), \*\*\* ( $\mathcal{P} \leq 0.01$ ), \*\*\*\* ( $\mathcal{P} \leq 0.0001$ ), ns (not significant).**

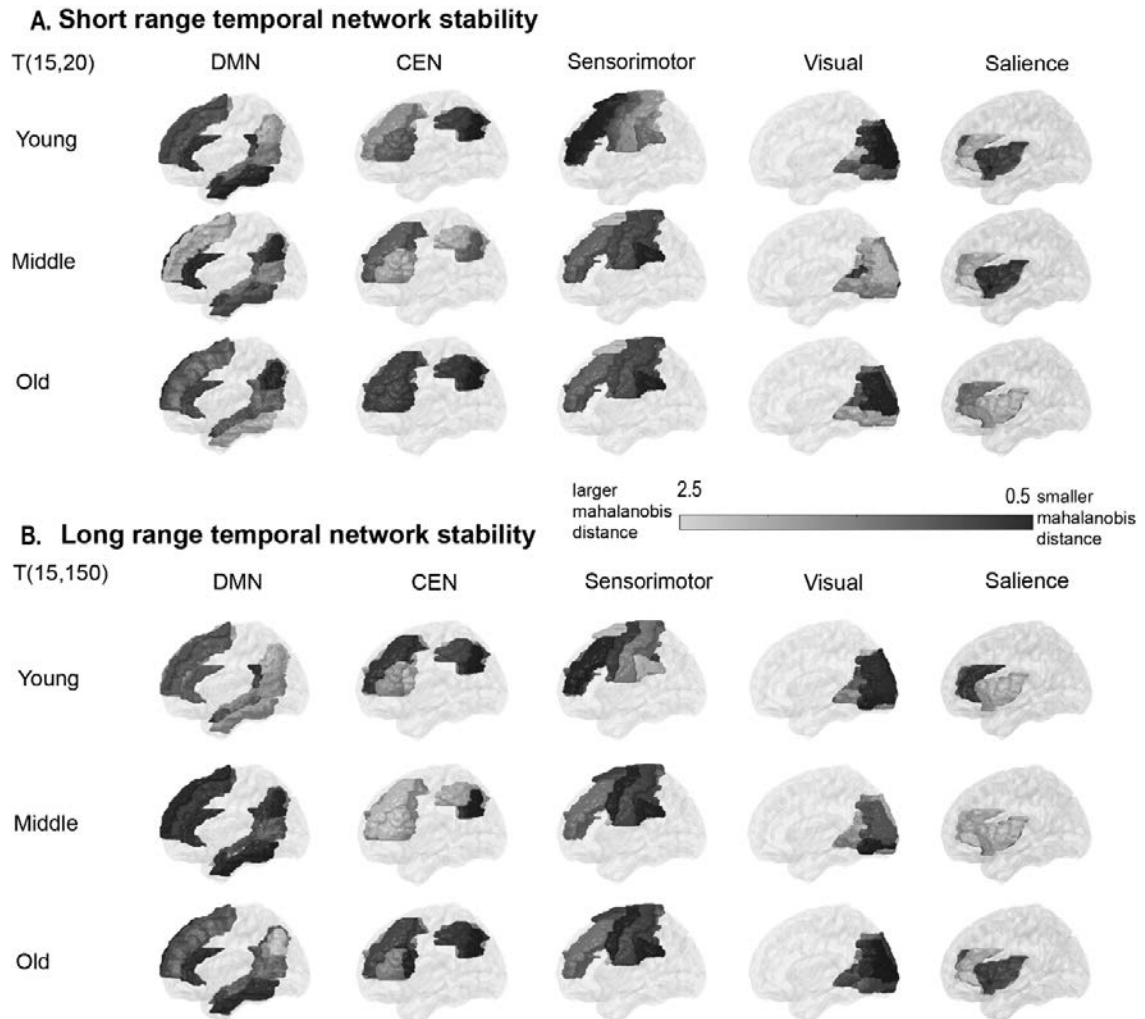


**Figure 2.6: Spatial profile of Mahalanobis distance across resting state networks** (A) Short-range temporal stability - Mahalanobis distance between dominant dFC subspaces of Default mode network (DMN), Central executive network (CEN), Sensorimotor network (SM), Saliency, and Visual brain networks at  $t=15$  and  $t=20$ . (B) Long-range temporal stability - Mahalanobis distance between dominant dFC subspaces of Default mode network (DMN), Central executive network (CEN), Sensorimotor network (SM), Saliency, and Visual brain networks at  $t=15$  and  $t=150$ .

### 2.3.3. Age related changes in temporal stability of dFC in resting state brain networks

Next, we apply our unsupervised approach of Principal Component Analysis (PCA) to BOLD time series of five resting state brain networks and at each time point estimate dominant *dFC* subspaces specific to the five resting state brain networks. Default mode network (DMN) regions were determined primarily according to (Fox, et al., 2005) and ROIs in the AAL atlas specific to DMN were selected according to (Wang , et al., 2012). We selected ROIs specific to Sensorimotor (SM) and Visual networks according to (Figueroa-Jimenez, et al., 2020) and ROIs specific to Central executive network (CEN) were selected according to (Oliver, Hlinka, Kopal, & Davidsen, 2019). We selected ROIs in AAL atlas specific to Salience network comprising of dorsal anterior cingulate cortex and anterior insula. Further, we estimate entropy to capture the temporal stability of dominant dFC subspaces of whole brain resting state and dominant dFC subspaces specific to five resting state brain networks (DMN, CEN, SM, Salience and Visual) using angular distance and mahalanobis distance, across lifespan ageing. We report only significant modifications in temporal stability of dFC subspaces with age in Figure 5 (we report others in A 2.6) Regression analysis revealed a “U” shaped trend for temporal stability of dFC subspaces of whole-brain resting state, sensorimotor, central executive and visual network with age. We found significant increase in temporal stability of whole brain resting state in older adults (Figure 5A). Of the five resting state brain networks, the temporal stability of sensorimotor network exhibited significant increase in older adults (Figure 5B), similar to whole brain resting state. The temporal stability of central executive network (Figure 5C) and, visual network (Figure 5D) demonstrated significant

decrease with age. We found no significant modifications in temporal stability of dFC with Mahalanobis distance metric. We report results estimated using Mahalanobis distance metric in A 2.7. Detailed overview of the terms included in the regression analysis is shown in A 2.8. The profile of temporal stability, estimated with Mahalanobis distance across brain regions is shown in Figure 2.6. We report two examples for young, middle and, older adults, one – short-range temporal stability i.e., Mahalanobis distance between dominant dFC subspaces of DMN, CEN, SM, Salience and Visual networks at  $t=15$  and  $t=20$  (see Figure 2.6A) and two – long-range temporal stability i.e., Mahalanobis distance between dominant dFC subspaces of DMN, CEN, SM, Salience and Visual networks at  $t=15$  and  $t=150$  (see Figure 2.6B). In summary, short and long-range temporal stability was assessed empirically by comparing time points that were 5 and 135 data points apart, respectively.

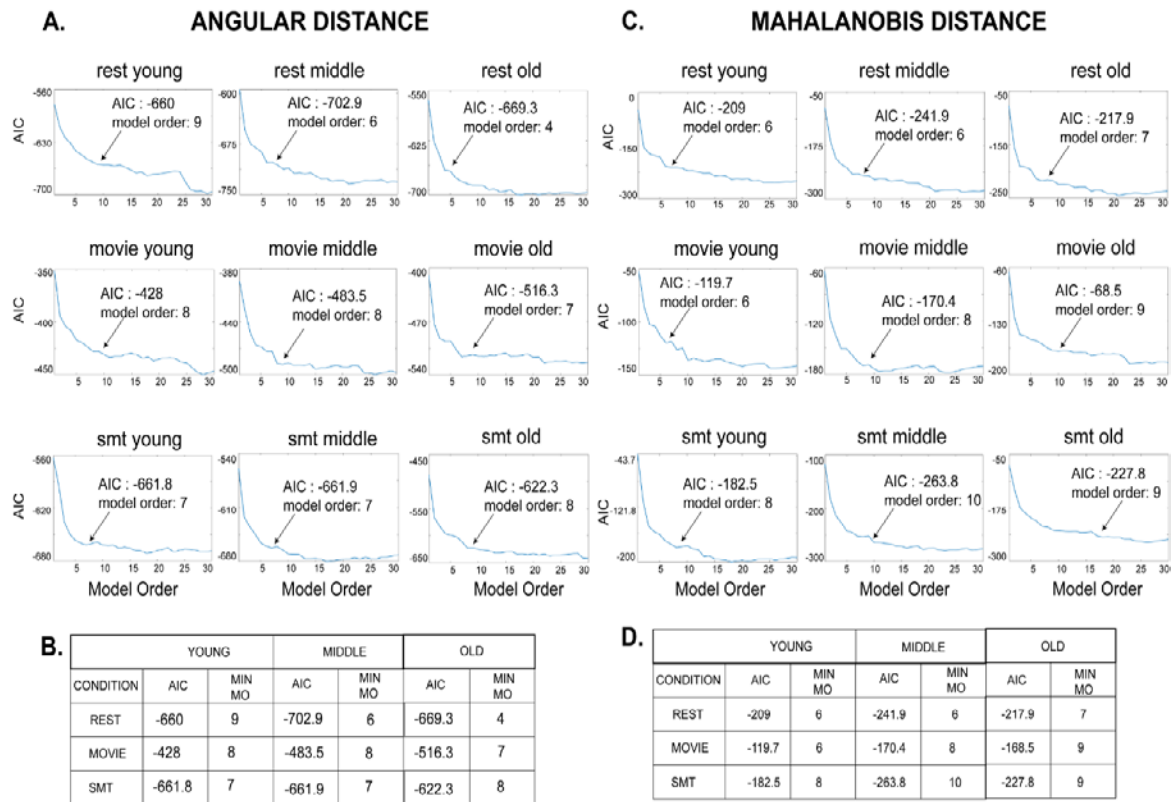


**Figure 2.7: Stochastic characterization of dFC** (A) Stochastic modelling of principal angle,  $\phi(t)$  as autoregressive,  $AR(\rho)$  process. The model order ( $\rho$ ) was varied from 0 to 100. The plot represents Akaike information criterion (AIC) values corresponding to the model order. Inset shows the first minima of the AIC value and its corresponding model order. (B) Table shows first minimal AIC value and its corresponding model order of  $\phi(t)$  for all the categories (C) Stochastic modelling of Mahalanobis distance,  $M(t)$  as  $AR(\rho)$  process. The model order ( $\rho$ ) was varied from 0 to 100. The plot represents AIC values corresponding to the model order. Inset shows the first minima of the AIC value and its corresponding model order. (D) Table shows first minimal AIC value and its corresponding model order of  $M(t)$  for all the categories

#### 2.3.4. Stochastic characterization of $dFC$

We examined the stochastic structure of  $dFC$  evolution by investigating the principal angle  $\phi(t)$  and Mahalanobis distance  $M(t)$  as functions of time.  $\phi(t)$  and  $M(t)$  are modelled as auto-regressive or AR ( $\rho$ ) process. The optimal model order was taken to be at the value which yields first lowest Akaike information criterion (AIC). The results from this analysis shown in Figure 7A and Figure 7B reveal the best fit model that explains  $\phi(t)$  has a model order  $\rho \geq 4$  i.e., the results suggest  $\phi(t)$  of resting state, movie watching task and sensorimotor task, in both young and old adults, is neither random ( $\rho \neq 0$ ) nor markovian ( $\rho \neq 1$ ) in nature, and is dependent on at least 4 immediately preceding values of  $\phi$ . For  $M(t)$ , as shown in Figure 7C and Figure 7D both resting state and tasks have the optimum model order  $\rho \geq 6$ , suggesting  $M(t)$  is neither random ( $\rho \neq 0$ ) nor markovian ( $\rho \neq 1$ ) in both young and old adults.



## 2.4. Discussion

The functional architecture of the brain is dynamic and changes on a minute temporal scale during resting state and task (Gonzalez-Castillo J. , et al., 2015) (Hutchison & et al, 2013) (Gonzalez-Castillo & Bandettini, 2018) (Bolton, Morgenroth, Preti, & Van De Ville, 2020). While previous studies have explored flexibility (Zhang & et al, 2016) (Yin, et al., 2016) and temporal variability (Zhang & et al, 2016) (Li, Lu, & Yan, 2019) of the functional architecture of a specific region, we propose a novel unsupervised method, that captures the stability of whole-brain functional architecture on a minute temporal scale. First, we apply the data-driven unsupervised approach to characterize the high dimensional dynamic functional connectivity into lower dimensional patterns by identifying temporally similar dominant FC configurations. Subsequently, using two different measures - principal angle and Mahalanobis distance applied on dFCs extracted across time, we capture the stability of dFC through the *temporal stability matrices* that could be used to draw critical insights about underlying functional brain states. For empirical validation, we explored modifications in temporal stability matrices of whole-brain FC during a continuous, naturalistic movie watching task and discrete, goal oriented sensorimotor task and showed that, in contrast to resting state, stability increased during the task (stability was highest in the sensorimotor task, followed by naturalistic movie watching task and resting state). Next, we explored ageing specific modulations in temporal stability matrices of dFC patterns between resting state and task and showed an overall increase in stability during the tasks across lifespan ageing. To gather insight at each stage of adulthood, we divide N=645 participants into three age categories – young (18-40 years), middle (41-60 years) and, old adults (61-88 years). Our results revealed significant differences in

temporal stability during task between young, middle and old adults. Temporal stability was highest in young adults, followed by middle and old adults during both movie-watching and sensorimotor task. Applying our unsupervised method on specific resting state brain networks revealed significant differences in temporal stability variation with age and allowed us to identify which of the resting state sub-networks shape the global age-related pattern change. Finally, we examined the stochastic properties of temporal stability matrices using an auto-regressive modelling, and showed dominant whole-brain FC configurations are neither random nor Markovian. With our results, using a novel unsupervised method, we were able to demonstrate significant differences in stability of dFCs among conditions and age groups which establishes the validity of our analysis – in the sense that low-dimensional dFC subspaces and subsequent estimation of temporal stability using quantitative metrics substantiated group differences and condition specific effects. We discuss the implications of these key results in the following subsections.

#### 2.4.1. Stochastic properties of dynamic functional connectivity

Studies describing brain dynamics have clustered recurring connectivity patterns into states, using clustering algorithms like K-means clustering (Allen E. , et al., 2014) (Cabral, et al., 2017) (Damaraju, et al., 2014), HMM (Cabral, et al., 2017) (Vidaurre, Smith, & Woolrich, 2017) (Vidaurre, et al., 2016) (Quinn, et al., 2018), suggestive of stability of functional architecture of the brain. Yet, most of the studies hypothesize a fixed number of discrete recurrent connectivity patterns or states with varying temporal fractional occupancy. The homogenous states are essentially clustered ignoring their temporal order and index. Studies have shown

clustering time series requires ignoring some data and few attempts at clustering time series have shown to be objectively incorrect in some cases (Rakthanmanon T. , Keogh, Lonardi, & Evans, 2011) (Rahman, Damaraju, Saha, Plis, & Calhoun, 2020). Rahman and colleagues (Rahman, Damaraju, Saha, Plis, & Calhoun, 2020) have proposed a novel framework, relying on the concept of shapelets, 'statelets'- a high dimensional state-shape representation of temporal dynamics of functional connectivity, instead of clustering. Another set of prior studies have explored the other side of stability – flexibility, which characterises heterogenous connectivity between a specific region and others over time (Yin, et al., 2016) (Harlalka, Bapi, Vinod, & Roy, 2019) and temporal variability (Zhang & et al, 2016) (Li, Lu, & Yan, 2019) of functional architecture in resting state (Li, Lu, & Yan, 2019) , naturalistic movie watching task (Li, Lu, & Yan, 2019) and in disease (Zhang & et al, 2016). But these studies are restricted to temporal variability and flexibility of the functional architecture of a specific region. Our main contribution in this study is an unsupervised, data-driven approach to characterise the stability of whole-brain functional connectivity patterns. A recent study (Faghiri , et al., 2020) has proposed a new method, where they calculate the gradients of timeseries pair and use their weighted average of shared trajectory (WAST) as a new estimator of dFC. This method defines a subspace on the raw BOLD fMRI timeseries whereas our approach estimated dFC with BOLD phase coherence and defined dominant whole-brain FC patterns as dominant dFC subspaces with PCA and characterised temporally similar dominant whole-brain FC patterns with two alternative measures, angular distance and verifying the same with Mahalanobis distance (Figure 2.1B). The central idea is if the dominant FC configurations are similar for extended time points, then they are considered to be stable.

Viduarre and colleagues (Viduarre, Smith, & Woolrich, 2017) have shown dynamic switching between brain networks and time spent visiting distinct brain networks are not random. Subsequently, another study has shown that the switching dynamics of functional brain states in the resting state follows AR model of order 1, or in other words a Markovian process fully explains the dFC evolution when correlation was computed using a sliding window approach (liégeois, Laumann, Snyder, Zhou, & Yeo, 2017). By constructing the unsupervised temporal stability matrices from two alternative approaches - principal angle,  $\phi(t)$  and Mahalanobis distance,  $M(t)$ , we reveal that dFC evolution is neither random nor Markovian (Figure7A and Figure7B) (Figure7C and Figure7D).

#### 2.4.2. Temporal stability of task related dynamic functional connectivity is higher than rest.

A key finding of our study indicates a global spread of shorter-lived, repeated patterns of stability between dominant FC configurations in resting state and local spread of longer-lived repeated patterns of stability in the task (in both continuous, naturalistic movie watching task and discrete goal oriented sensorimotor task) (Figure 2.2 B and Figure 2.3A). We find that in resting state the stability patterns are global, widespread with both short range (stability estimated between dominant dFC subspaces at timepoints in close proximity, for ex:  $D_{t_x}$  at  $t=15$  and  $D_{t_y}$  at  $t = 25$ ) and long-range temporal stability patterns (stability estimated between dominant dFC subspaces at timepoints distant from one another, for ex:  $D_{t_x}$  at  $t=15$  and  $D_{t_y}$  at  $t=150$ ), whereas in task *temporal stability matrices*, the stability patterns are limited with fewer long-range patterns. The resting state is shown to be a multistable stationary state-regime at equilibrium. In the absence of any stimuli, the

spontaneous resting state activity and the dynamics of formation and dissolution of Resting State Networks (RSNs) form multiple stable states (Deco & Jirsa, 2012). Ghosh and colleagues (Ghosh, Rho, McIntosh, Kötter, & Jirsa, 2008) have demonstrated that resting state networks operate close to instability and explore these states before committing to one of these states. Deco and Jirsa (Deco & Jirsa, 2012) have proposed that a repertoire of multistable states exists in resting state, that are functionally meaningful and inherently supported by the neuroanatomical connectivity, and can be rapidly activated even in the absence of any task. We speculate that in resting state the global spread of shorter-lived repeated patterns of stability between dominant FC configurations is associated with the exploration of multistable dynamic repertoire of states. On the contrary during a task (continuous or discrete), the repertoire of multistable states are limited, as only task-specific, cognitively relevant brain networks are explored. The brain visits task-specific stable states for duration that a putative stimulus triggered cognitive process demands. This is associated with the local spread of longer-lived temporal similarities between dominant functional connectivity subspaces in a task. Our entropy results indicate the stability of functional connectivity architecture was highest in the discrete, goal-oriented sensorimotor task, followed by continuous naturalistic movie watching task and resting state (Figure 2.4A). This is in line with previous studies which report an increase in overall stability of FC with the largest increase in between-network connections (Elton & Gao, 2015) (Gonzalez-Castillo & Bandettini, 2018), increase in stability of hemispheric homotopic connections during a task (Gonzalez-Castillo J. , Hoy, Handwerker, & Bandettini, 2014). Such increased stability of FC during a task is hypothesised to be associated with cognitive constraints during a task (Gonzalez-Castillo & Bandettini, 2018).

Frobenius distance analysis results reveal the temporal stability matrices of functional connectivity during continuous, naturalistic movie watching task was closer to resting state than discrete, goal oriented sensorimotor task (Figure 2.4C). Considering our Frobenius distance analysis, we hypothesized stability of functional connectivity architecture should be highest in the sensorimotor task, followed by the naturalistic movie watching task, which was validated by our entropy results. Our findings thus provide evidence of increased temporal stability of whole-brain functional connectivity in task, highest in the discrete, goal-oriented task, followed by continuous, naturalistic movie watching task and then resting-state, using a novel unsupervised approach of characterising the stability of functional connectivity architecture.

#### 2.4.3. Ageing introduces temporal variability in evolution of dynamic functional connectivity in both rest and task

Evidence from prior studies reveal the complexity of FC dynamics remains similar for all participants irrespective of age. An earlier study (Viviano, Raz, Yuan , & Damoiseaux, 2017) found no association between age and rate of switching between the FC states for resting brain. Our results (Figure 2.2 B and Figure 2.3 A) indicate the overall trend of global spread of shorter-lived repeated patterns of stability between dominant FC configurations in resting state and local spread of longer-lived repeated patterns of stability in the task, was similar in young, middle and old adults. Our study also revealed an overall trend of highest stability of functional connectivity in the discrete, goal-oriented sensorimotor task, followed by continuous, naturalistic movie watching task and resting state across lifespan ageing (Figure 2.4 A). The neural noise hypothesis suggests the age-related

cognitive decline could be explained as a consequence of the increase in the noisy baseline activity of the brain (Voytek, et al., 2015) (Davis , et al., 2009). Our results, which contrasted the stability of functional architecture in young, middle and old adults (Figure 2.4B) found increased stability of functional architecture in young adults, followed by middle and old adults in movie watching and sensorimotor task. In accordance to neural noise hypothesis, the decrease in stability of the functional architecture of the brain in older adults can be explained with an increase in neural noise with age. Interestingly, McIntosh and colleagues (McIntosh, et al., 2010) have reported BOLD signal variability of hub-region decreases with age, suggestive of increase in stability of hub regions with age. Our results, contrasting the stability of functional architecture of resting state in young, middle and old adults, report high stability in young and old adults and low stability in middle adults (Figure 2.4B). Previous resting state studies have reported quadratic or U-shaped trajectories of between-network connections with age (Betzel, et al., 2014) (Cao, et al., 2014). (Kupis, et al., 2021) demonstrate a U-shaped or quadratic trajectory among between-network connections in certain resting-state brain states in relation with cognitive flexibility across lifespan ageing. They also report shorter dwell time in middle adulthood and longer dwell time in childhood and older adulthood. Our result, scatter plot of entropy of whole-brain temporal dynamics matrices of resting state across lifespan ageing (N=645 participants) (Figure 2.5A) revealed an inverted U-shaped trajectory - with peak entropy among middle adults and low entropy among young and older adults. Our results are in line with (Kupis, et al., 2021) as shorter dwell time in middle adulthood among brain states suggests decrease in stability of functional architecture in middle adults.

#### 2.4.4. Dynamics of whole brain resting state is primarily influenced by stability of sensorimotor network across lifespan ageing

Earlier studies investigating age-related changes in resting state networks across lifespan have reported decrease in functional connectivity within default mode network (DMN) from early to late adulthood (Tomasi & Volkow, 2012) (Jockwitz & Caspers, 2021). (Betzel, et al., 2014) found decrease in resting state network modularity with age indicative of decrease in functional cohesiveness. (Chen, et al., 2021) report, in older adults, decrease in dwell time on a state where DMN and attention networks show antagonistic activity. They report increase in dwell time on a “baseline” state, and, higher transition probabilities from others to this state in the elderly. Our results, using angular distance metric, demonstrate significant decrease in temporal stability of central executive network (CEN) and, Visual networks in older adults (Figure 5C and Figure 5D). Whereas, the temporal stability of whole-brain resting state dFC and sensorimotor network significantly increased with age (Figure 5A and Figure 5B). Of the five resting state networks, we find stability dynamics of whole-brain resting state closely follows that of sensorimotor network with age. Recently, (Kong, et al., 2021) have shown causal manipulation of a large-scale circuit model describing resting state brain dynamics, suggests that sensorimotor regions are a driver of FC dynamics. (King, et al., 2017) attribute age-related decline in motor performance to decrease in segregation of large-scale brain networks rather than age-related connectivity changes within motor-related network. Our results demonstrate the influence of stability of sensorimotor network on stability dynamics of whole-brain resting state, which (King, et al., 2017) have associated with age-related decline in motor performance. We did not find significant differences in temporal stability of resting state networks with age using



Mahalanobis distance metric (see A 2.7). The differences in temporal stability of dominant subspaces across resting state networks with angular distance and Mahalanobis distance could be an outcome of the limitations of computing angular/Mahalanobis distance between linear subspaces. The Mahalanobis distance is a multidimensional generalization of the distance between a point P and a distribution D (Mahalanobis, 1930). In the current study, for each timepoint, Mahalanobis distance was calculated between each ROI in the reduced dominant dFC subspace  $D_{t_y}$  and whole-brain subspace  $D_{t_x}$ . Every ROI in  $D_{t_y}$  (point P) has Mahalanobis distance estimated with respect to subspace  $D_{t_x}$  (distribution D). In our case, Mahalanobis distance is the mean of the distance of all the points (i.e., ROIs) in dominant dFC subspace at  $t = t_i$  with distribution of dominant dFC subspace at  $t = t_j$  whereas angular distance is the scalar angle between the dominant dFC subspace at  $t = t_i$  with dominant dFC subspace at  $t = t_j$ . Mahalanobis distance takes into account the correlations of the data and, is a scale-invariant measure (Maesschalck, Jouan-Rimbaud, & Massart, 2000). Another reason may be due to the high dimensionality of the dynamic functional connectivity, the data is sparsely distributed in the high dimensional subspace, - referred to as “curse of dimensionality” (Y. Kuo & Sloan, 2005). Although principal component analysis (PCA) is a robust dimensionality reduction technique, used to circumvent “curse of dimensionality”, studies have found PCA is sensitive to outliers (J. Candès, Li, Ma, & Wright, 2011) and, degradation of performance of PCA when the dimensionality of data increases (Shetta & Niranjana, 2020).

#### 2.4.5. Limitations and Future directions

An important caveat of the current study was due to parcellation atlas used in the Cam-CAN dataset. The AAL atlas parcellates the brain regions into 116 structural parcels and few parcels span multiple functional regions. For future studies, for a more refined spatial profile of temporal stability of functional architecture, using a finely parcellated brain atlas is recommended. Researchers have shown stability of functional architecture is modified in patients of Schizophrenia, ADHD and ASD (Zhang & et al, 2016) (Guo, Zhao, Tao, Liu, & Palaniyappan, 2017). Hence, we can extrapolate that the temporal stability of functional architecture can provide a richer information to discover biomarkers for neurological and mental disorders. A meaningful extension of the present work would be to investigate the influence of subject-level characteristics and even, behavioural scores on temporal stability of FC. We want to address this in a future study including all different variables and demographic information over adult life span. This exercise could also strengthen and provide evidence for the robustness of the method and may aide in uncovering temporal stability markers specific to the tasks.

#### 2.4.6. Conclusion

In summary, the current study introduces a data-driven unsupervised approach to characterise the temporal stability of functional architecture. When applied to a putative lifespan ageing data, the whole-brain temporal dynamics of naturalistic movie watching task was found to be closer to resting state than during sensorimotor task. Further, the study revealed peak temporal stability in sensorimotor task, followed by naturalistic movie watching task and resting state, a trend similar in both young, middle and elderly. The dynamics of the temporal

stability of functional architecture of the whole-brain resting state was primarily influenced by temporal stability of sensorimotor network across lifespan ageing. The quantification of differences in network stability associated with healthy ageing provides evidence for the potency of the temporal stability measure to act as biomarker for multiple neurological disorder

## Chapter 3

# Temporal stability of resting state functional connectome across common mental disorders

### 3.1. Introduction

Common mental disorders, such as bipolar disorder, ADHD, and schizophrenia, have a significant societal impact in terms of disability-adjusted life years (DALYs), years lived with disability (YLDs), and years of life lost (YLLs) (Alize J Ferrari, 2022). Developing prevention and intervention strategies to assist behavioural psychiatrists is crucial in addressing these disorders. Non-invasive neuroimaging techniques, including functional magnetic resonance imaging (fMRI) and brain connectivity analytics, have emerged as powerful tools for early detection and management of these disorders (Edgar Canario, 2021) (Miranda, Paul , Putz, Koutsouleris, & Muller-Myhsok, 2021). The spontaneous resting state dynamics of the brain, which is believed to emerge from more robust metabolic and neural information processing principles (Deco , Jirsa , & McIntosh, 2010) (Smith , et al., 2013) offers a practical framework for investigating biomarkers of common mental disorders. Previous studies investigating alterations in resting-state brain dynamics in common mental health disorders have largely focused on the strategies of functional connectome communities – the mesoscale organization of individual neural elements into motifs, circuits, or clusters (Betzel , Medgalia , & Bassett,

2018). These studies have reported changes in community organization and decreased modularity in functional brain networks in schizophrenia and bipolar disorder (Alexander-Bloch, et al., 2010) (Yu , et al., 2020) (Lerman-Sinkoff & Barch , 2016). Other studies using multilayer community detection algorithms have reported altered community structure and higher flexibility in patients with schizophrenia (Gifford , et al., 2020) and ADHD (Ding , et al., 2022). A major drawback of most of these studies, in addition to the methodological biases of the community detection algorithms (Betzel , Medgalia , & Bassett, 2018) is the utilization of static functional connectivity to detect functional connectome communities. Recently, it has been demonstrated that resting-state functional brain networks exhibit spontaneous, time-varying, large-scale dynamic reconfiguration (Hutchison , et al., 2013) (Cabral , et al., 2017) (Allen E. , et al., 2014) .This suggests that measures assuming stationarity for the entire duration of the scan are too simplistic to capture the full extent of resting brain dynamics (Prete, Bolton, & De ville, 2017).

Dynamic functional connectivity (dFC) has been shown to exhibit non-random and non-trivial temporal structures (Lombardo, et al., 2020) and is associated with cognitive processing, learning, attention, and performance (Cohen , 2018), (Bassett, et al., 2011), (Kucyi, Hove , Esterman, Hutchison, & Valera, 2017), (Jia , Hu, & Deshpande , 2014) . The dysconnectivity observed in common mental health disorders suggests the presence of complex and transient spatiotemporal alterations in functional connectivity (Alexander-Bloch , et al., 2012), (Gifford , et al., 2020). This naturally raises the question: Are there alterations in dynamic functional connectivity (dFC) within the resting state functional connectome in common mental disorders? How can these patterns of dFC be accurately captured

and comprehensively studied? Moreover, can these patterns of dFC serve as characterizations for common mental disorders? Earlier studies have emphasized the significance of stability in dFC patterns over time for ensuring consistent information representation in the distributed neural connectome (Le , Lu , & Yan , 2020). While several studies have examined the temporal stability of the brain's functional connectome during resting state (Le , Lu , & Yan , 2020) and throughout healthy lifespan aging (Sastry, Roy, & Banerjee, 2023) only a limited number of studies have investigated alterations in the temporal stability of the whole-brain dynamic functional connectome in common mental health disorders (Zhang , et al., 2021) (Dong , et al., 2019).

A common approach to investigate the temporal stability of dFC is to summarize resting state brain activity into discrete states using techniques such as the K-means clustering algorithm (Allen E. , et al., 2014) (Cabral , et al., 2017) or the Hidden Markov model (Viduarre, Smith, & Woolrich , 2017) (Surampudi, et al., 2018). Temporal stability is then estimated by measuring the "switching rate" between these brain states. The switching rate, also known as flexibility, quantifies how quickly a specific node transitions between different brain states. Higher flexibility suggests more frequent transitions, which leads to reduced temporal stability (Long , Lu, & Liu, 2023). Other graph theoretical studies measure temporal stability by introducing the *temporal correlation coefficient*, which estimates the tendency of a dynamic brain network to remain stable over time. This coefficient calculates the average topological overlap of the network connections (Long , et al., 2023). However, these studies, which assume the existence of multiple discrete brain states, are limited by methodological drawbacks of the clustering algorithm and the predefined number of states (Rakthanmanon T. , Keogh, Lonardi, & Evans

, 2011) (Allen E. , et al., 2014) . As a result, they are ineffective in describing the temporal evolution of dFC. An alternative perspective is to view the temporal dynamics of dFC as a continuous process, investigating global and regional dynamics by measuring variability and similarity using techniques like Pearson correlation (Zhang , et al., 2016), angular distance (Sastry, Roy, & Banerjee, 2023) or *dFCSpeed* (Arbazyazd, et al., 2020). Previous studies on mental health disorders have associated increased temporal variability in schizophrenia with decreased stability in visual and subcortical regions (Zhang , et al., 2016) and reduced dFC variability in default mode and fronto-parietal networks (Dong , et al., 2019). Bipolar disorder showed a decreased switching rate in the precuneus, dorsal medial prefrontal cortex, and parahippocampal gyrus (Han , et al., 2020). Zhang and colleagues (Zhang , et al., 2016) reported decreased temporal stability in the default mode network in ADHD patients. However, most studies on temporal stability in mental health disorders focus on region-wise dFC patterns.

The objective of this study is to investigate the potential of dFC measures as characterizing tools for common mental disorders. The analysis utilizes two datasets consisting of 408 participants diagnosed with schizophrenia, bipolar disorder, and ADHD. The initial analysis focuses on exploring differences in community structure and interactions across these mental health disorders, using a generative community detection approach and mapping community interactions into assortative, coreness, and peripheryness motifs (Betzel, Bertolero, & Bassett, 2018). Next, the temporal dynamics of the resting state dynamic functional connectome, both at the whole-brain and network level, are characterized and visualized as a temporal landscape. An unsupervised data-driven approach described in (Sastry, Roy, & Banerjee, 2023) is used to estimate temporal stability.

Two novel measures are introduced: 1) entropy, which calculates temporal stability across all time points over the entire temporal landscape, and 2) global temporal distance, which quantifies temporal stability across successive time points. Through this comprehensive analysis, the study aims to gain insights into the potential of dFC measures as effective characterizing tools for common mental disorders. The analysis of two datasets, with a total of 408 participants, provides new evidence to draw critical insights about disease-specific modifications in temporal stability and community structure of the dynamic functional connectome.



## 3.2. Material and methods

### 3.2.1. Participants and Image acquisition

Overall, the study included two multicentre datasets involving 408 human participants. We downloaded resting state functional magnetic resonance imaging (fMRI) data from 285 participants who participated in the University of California Los Angeles (UCLA) Consortium for Neuropsychiatric Phenomics LA5c study (*Dataset 1*) (Poldrack, et al., 2016) (Gorgolewski, Durnez, & Poldrack, 2017). The public database was obtained via openfMRI (<https://openfmri.org/dataset/ds000030/>) and includes 138 healthy controls (HC), 58 individuals diagnosed with schizophrenia (SZ), 40 with attention deficit hyperactivity disorder (ADHD) and 49 with bipolar disorder (BP). Data from 14 healthy controls and 8 participants with schizophrenia were removed during preprocessing (see below). For both healthy and patient groups, participants were men or women, of any racial group, whose primary language was either English or Spanish, who completed at least 8 years of formal education, no significant medical illness, had visual acuity 20/60 or better and urinalysis negative for drugs of abuse (Cocaine; Methamphetamine; Morphine; THC; and Benzodiazepines) (Poldrack, et al., 2016). In the healthy control group, participants were excluded if they had lifetime diagnosis of Schizophrenia, Bipolar I or II disorder, substance abuse/dependence or current major Depressive disorder, suicidality, anxiety disorder and ADHD. Healthy participants were also screened for threshold ADHD and they could not have had medication treatment for ADHD within the prior 12 months. Each of the patient groups (SZ, BP, ADHD) excluded anyone with one of these other diagnoses. Stable medications were permitted for the patients. Participants who were left-handed, pregnant or had other conditions (metal in the body) were excluded for MRI studies (Poldrack, et al., 2016). The

resting state fMRI (rs-fMRI) data was acquired on 3T Siemens Trio scanner using echo planar imaging (EPI) sequence consisting of 152 volumes with the following parameters – slice thickness = 4mm, TR = 2s, TE = 30ms, flip angle = 90°, acquisition matrix = 64 X 64 sq.mm, voxel size = 3 X 3 X 4 mm<sup>3</sup>. More details on acquisition parameters can be found in (Poldrack, et al., 2016).

For the replication analysis, a publicly available dataset from the center for Biomedical Research Excellence (COBRE) was obtained (Calhoun, et al., 2012) (Bellec, 2016). The neuroimaging dataset (*Dataset 2*) included resting state functional MRI scans from 72 participants with schizophrenia and 74 healthy controls. All the subjects were screened and excluded if they had a history of mental retardation, a history of severe head trauma with more than 5 mins of loss of consciousness, history of substance abuse or dependence within the last 12 months. Diagnostic information was collected using the Structured Clinical interview used for DSM disorders (SCID). The eyes open rs-fMRI data was collected with echo-planar imaging (EPI sequence) consisting of 150 volumes, scan duration of 5 mins with a repetition time (TR) = 2s, echo time = 29 ms, acquisition matrix = 64 X 64 sq.mm, flip angle = 75 ° and voxel size = 3 X 3 X 4 mm<sup>3</sup>. A detailed description of acquisition parameters can be found in (Bellec, 2016).

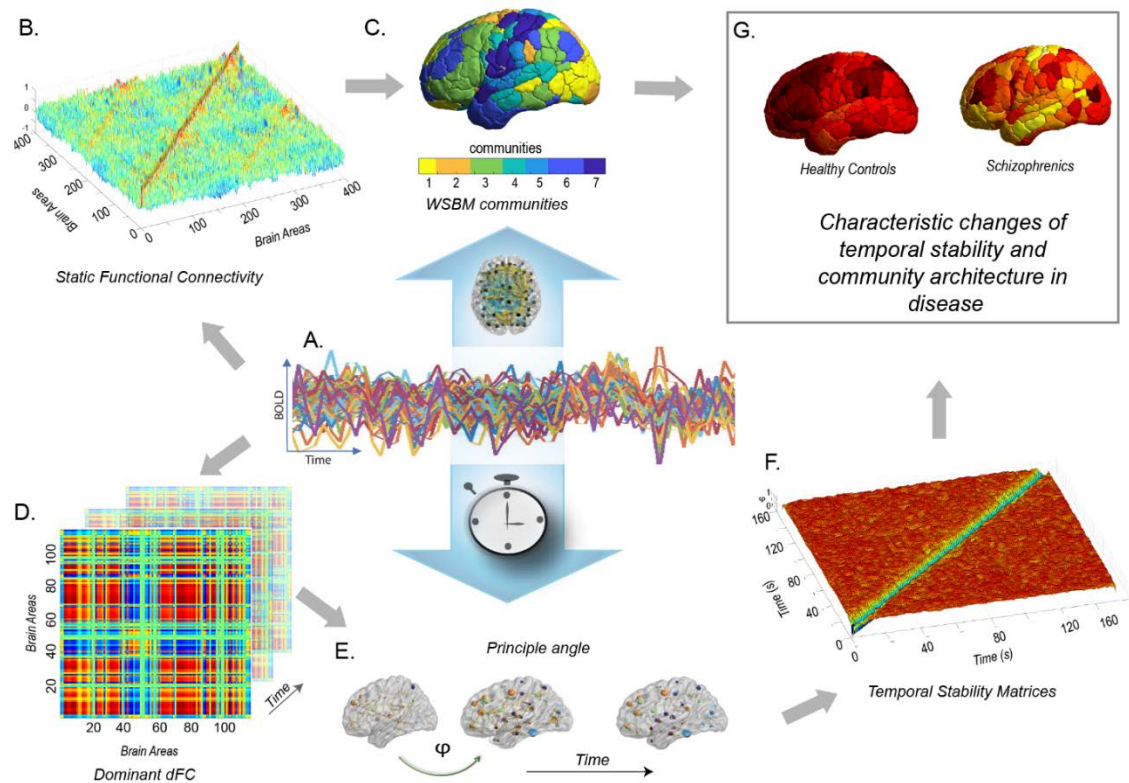


**Figure 3.1 a brief overview of the methodology used in this study.** (A) shows the BOLD time series data (B) illustrates the estimation of static functional connectivity using Pearson correlation, which is then transformed using the  $r$ -to- $z$  method (C) displays topographic representation of the WSBM communities. The subject-wise undirected, signed, weighted adjacency matrix serves as the input for the Weighted Stochastic Block Model (WSBM), a data-driven generative community detection algorithm that groups brain areas into  $K=7$  communities based on their stochastic equivalence. (D) presents the matrix representation of the reduced dominant dynamic functional connectivity (dFC) patterns, denoted as  $D(t)$ , computed at each time point (E) demonstrates the calculation of similarity between dominant dFC subspaces using angular distance or principal angle ( $\phi$ ) (F) showcases the Time X Time temporal stability matrix, where each entry represents the principal angle ( $\phi(t_x, t_y)$ ) between dominant dFC subspaces at time points  $t_x$  and  $t_y$ . This matrix visualizes the temporal landscape, with the principal angle ranging from 0 (indicating low angular distance) to  $\pi/2$  (indicating high angular distance). Constructing a Time X Time temporal stability matrix allows us to visualize the temporal "landscape" for the entire duration of the scan. (G) we calculate the temporal stability of the dynamic functional connectome using two measures: entropy and global temporal distance. We investigate changes in community architecture in common mental health disorders such as schizophrenia, bipolar disorder, and ADHD.

### 3.2.2. Data preprocessing and parcellation

The rs-fMRI images were pre-processed using the CONN toolbox (McGovern Institute for Brain Research, MIT, USA) running under MATLAB (The MathWorks). The default CONN preprocessing pipeline (*defaultMNI*) was used which includes the following steps: functional realignment and unwarp; slice-time correction; outlier identification; direct segmentation and normalization; functional smoothing. In the first step, the fMRI data were unwrapped and realigned using SPM12 *realign & unwarp* procedure (Andersson, Hutton, Ashburner, Turner, & Friston, 2001) where all scans are co-registered to a reference image using a least squares approach, resampled using b-spline interpolation to correct for motion and magnetic susceptibility interactions. Temporal misalignment between different slices of the functional data was corrected using SPM slice-timing correction (STC) procedure (Sladky, et al., 2011). Potential outlier scans were identified using ART. Functional and anatomical scans were normalized to standard MNI space, segmented into grey matter, white matter and cerebro-spinal fluid (CSF) tissue classes, and resampled to 2mm isotropic voxels following a direct normalization procedure using SPM unified segmentation and normalization algorithm (Calhoun, et al., 2017). Lastly, functional data is smoothed using spatial convolution with a Gaussian kernel of 8 mm full-width half maximum (FWHM). In addition, functional data were denoised using a standard denoising procedure (Castanon, 2020), followed by bandpass frequency filtering of BOLD time series between 0.01 Hz and 0.1 Hz. In *Dataset 1*, an inspection of fMRI data for each subject resulted in the exclusion of 14 healthy controls and 8 schizophrenics whose data did not include – 1) all 152 functional volumes 2) T1 w structural images. A detailed overview of

the preprocessing pipeline can be found at <https://web.conn-toolbox.org/fmri-methods/preprocessing-pipeline> . The final datasets used in this analysis and their group characteristics are described in Table 3.1. Resting state scans of each participant were parcellated using 400 region Schaefer parcellation (Schaefer , et al., 2018). This atlas was chosen as it pre-allocates brain regions or nodes into resting state networks (RSNs). For each subject, mean BOLD time series (Figure 3.1A) were estimated for each region over all voxels belonging to that brain region.

*Table 3.1 Demographics of the UCLA consortium for Neuropsychiatric phenomics LA5c dataset (Dataset 1) and COBRE dataset (Dataset 2) used in this study*

	Groups	N	Age (years)	Sex (% female)
UCLA dataset (Dataset 1)	Schizophrenia	50	36.46 ± 8.87	24 %
	Healthy Controls	124	31.58 ± 8.80	44.90 %
	Bipolar disorder	49	35.28 ± 9.02	42.80 %
	ADHD	40	33.09 ± 10.7	51.16 %
COBRE Dataset (Dataset 2)	Schizophrenia	71	38.16 ± 13.8	19.71 %
	Healthy Controls	74	35.82 ± 11.5	31.08 %

### 3.2.3. Estimating time dependant functional connectivity and dominant dFC matrices

These methods have first been introduced in (Sastry, Roy, & Banerjee, 2023) in the context of healthy ageing. Here we provide a brief explanation. For each subject, we estimate time-resolved dynamic functional connectivity (dFC) using BOLD phase coherence (Figure 3.1A) (Glerean E. , Salmi, Lahnakoski, Jaaskelainen, & Sams , 2012) (Deco & Kringelbach, 2016) (Cabral , et al., 2017), which resulted in a matrix with size  $N \times N \times T$ , where  $N = 400$  is the number of brain regions,  $T$  is the total number of time points ( $T = 152$  for *Dataset 1*, and  $T = 150$  for *Dataset 2*). First, instantaneous phases  $\theta(n, t)$  of the BOLD signals for all

the brain regions  $n$ , was calculated using Hilbert transform. Given the phases of BOLD signals, phase coherence between brain areas  $n$  and  $p$  at each timepoint  $t$ , i.e.,  $dFC(n, p, t)$  is computed as:

$$dFC(n, p, t) = \cos(\theta(n, t) - \theta(p, t)) \quad (3.1)$$

To characterize the evolution of dFC over time, we extract dominant subspace of dFC patterns (Figure 3.1B), by applying PCA (Friston K. , Frith, Liddle , & Frackowiak, 1993) (Sastry, Roy, & Banerjee, 2023). Accordingly,  $dFC(n, p, t)$ .  $dFC(n, p, t)$  can be expressed as

$$dFC(n, p, t) = V^T S V \quad (3.2)$$

Where matrix  $V$  with size  $N \times N$ , is the set of eigen vectors with each column (1 X N) representing an orthogonal principal component and  $S$  is the diagonal matrix

$$\begin{pmatrix} \lambda_1 & \dots & 0 \\ \vdots & \ddots & \vdots \\ 0 & \dots & \lambda_n \end{pmatrix},$$

such that  $\lambda_1 > \lambda_2 \dots \lambda_n$ . If  $m$  (in this study,  $m=3$ ) is the number of principal components chosen, then dominant dFC ( $D_t$ ) can be expressed as:

$$D_t = \hat{V}^T \hat{S} \hat{V} \quad (3.3)$$

Where  $\hat{V}^T$  is dimensionally reduced matrix of size  $N \times m$ ,  $\hat{S}$  is a diagonal matrix

$$\begin{pmatrix} \lambda_1 & \dots & 0 \\ \vdots & \ddots & \vdots \\ 0 & \dots & \lambda_m \end{pmatrix}.$$

### 3.2.4. Constructing temporal stability matrices

Given a set of dominant dFC matrices ( $D_t$ ), we seek to characterize temporal stability using the similarity of dFC patterns across timepoints. We use angular distance (Figure 3.1C) (Bjorck & Golub, 1973) (Banerjee A. , Pillai, Sperling , Smith , & Horwitz, 2012) (Sastry, Roy, & Banerjee, 2023) to estimate the similarity between dominant dFC subspaces. We define angular distance as the principal angle between dFC subspaces from different timepoints, given by:

$$\phi(t_x, t_y) = \angle(D_{t_x}, D_{t_y}) \quad (3.4)$$

Where  $\phi(t_x, t_y)$  is the principal angle between dominant dFC subspaces,  $D_{t_x}$  and  $D_{t_y}$  at time  $t_x$  and  $t_y$ . For each subject, we construct a *time X time* temporal stability matrix where each entry in the matrix is  $\phi(t_x, t_y)$ . The principal angle ranges between 0 (low angular distance) to  $\pi/2$  (high angular distance). The low angular distance between dominant dFC subspaces indicates that their dFC configurations are very similar, on the other hand, the high angular distance points to dissimilar dFC configurations.

### 3.2.5. Measures of temporal stability

Constructing a *time X time* temporal stability matrix allows us to visualize the '*temporal landscape*' (Figure 3.1D) for the entire duration of the scan. Visual inspection indicates differences in *temporal landscape* between healthy controls and patient groups. We introduce two distinct perspectives on measures of temporal stability – firstly, we seek to quantify temporal stability over the entire *time X time* temporal landscape across all timepoints. To achieve this, we evaluate the

informational content of the stability matrices by calculating entropy (Sastry, Roy, & Banerjee, 2023). We use entropy because it is a more direct measure of order and disorder in a dynamical system and provides us a measure of distinguishable temporal order that can be interpreted as the overall stability of the temporal stability landscape (Yang, et al., 2013). Entropy is defined by the following equation:

$$E = -\sum p \log(p) \quad (3.5)$$

Where  $p$  contains normalized histogram counts returned from “imhist.m” applied on temporal stability matrices, estimated using reduced  $D_{t_x}$  and  $D_{t_y}$ . “imhist.m” calculates the histogram of temporal stability matrices and returns the normalized counts. Overall temporal stability is estimated as follows

$$TS = 1/E \quad (3.6)$$

Secondly, we seek to quantify temporal stability across successive time windows. To do this, we estimate the *global temporal distance* by taking the average of the off-diagonal elements of the temporal stability matrix. The off-diagonal elements are angular distances among dominant dFC subspaces at two successive time points, thus the term ‘*global*’ signifies that the measure captures a temporally averaged snapshot of the dFC evolution.

$$\text{Global temporal distance} = \frac{1}{(t-1)} \sum_{i,j=i+1,i \neq j}^{T-1} \phi(t_i, t_j) \quad (3.7)$$



Where,  $\phi(t_i, t_j)$  is the angular distance entry at  $i^{th}$  row and  $j^{th}$  column in the temporal stability matrix,  $T$  is the total number of timepoints. *Global temporal stability* ( $TS_{global}$ ) is defined as the inverse of the *global temporal distance*:

$$TS_{global} = \frac{1}{Global\ temporal\ distance} \quad (3.8)$$

### 3.2.6. Model-based community detection using the weighted stochastic block model (WSBM) on static FC

We estimate the static functional connectivity (Friston K. , 2011) between two brain areas,  $n, p$  by calculating the Pearson correlation between BOLD time series of brain areas  $n, p$  (Biswal, Yetkin, Haughton, & Hyde , 1995) (Figure 3.1E). The correlations were subsequently r-to-z transformed. The  $N \times N$  functional connectivity matrix was represented as a network in which regions were represented by network nodes and functional connectivity between region  $n$  and region  $p$  was represented by network edge between nodes  $n$  and  $p$  (Bassett, Zurn , & Gold , 2018). Thereafter, subject-wise undirected, signed, weighted adjacency matrix ( $A$ ) was estimated for detection of community architecture.

The weighted stochastic block model (WSBM) is a generative model for learning community structure, which places each of the  $n$  nodes (brain areas) in the adjacency matrix  $A$  into one of  $k$  communities or “blocks” (Aicher , Jacobs , & Clauset, 2015). Nodes in the same community are stochastically equivalent, indicating their equivalent roles in generating the network’s structure. In its classic form stochastic block model (SBM), assumes an unweighted network, and the probability of edge existence is learned for each block. The weighted stochastic block model ( $WSBM$ ) is a generalization of SBM that can learn from both the

presence and weight of the edges. Specifically, WSBM models each weighted edge  $A_{ij}$  as a draw from a parametric family distribution, whose parameters  $\mu$  and  $\sigma$  depend only on block memberships of connecting nodes  $i$  and  $j$  (Aicher , Jacobs , & Clauset, 2015) (Tooley , Bassett, & Mackey, 2022).

In the SBM, the network's adjacency matrix  $A$  contains binary values for edge existence,  $A_{ij} \in \{0,1\}$ ,  $k$  denotes the fixed number of blocks or communities and vector  $z$  contains the group label for each node  $Z_i \in \{1, 2, \dots, k\}$ . The SBM assigns an edge existence parameter to each edge bundle  $\theta_{kk}$ . Assuming the placement of the edges are independent of one another, the likelihood function of SBM for  $A_{ij}$  can be written as:

$$\Pr(A | z, \theta) = \prod_{ij} \theta_{z_i z_j}^{A_{ij}} (1 - \theta_{z_i z_j})^{1 - A_{ij}} \quad (3.9)$$

Which can be rewritten as,

$$\Pr(A | z, \theta) = \prod_{ij} \exp(A_{ij} \cdot \log\left(\frac{\theta_{z_i z_j}}{1 - \theta_{z_i z_j}}\right) + \log(1 - \theta_{z_i z_j})) \quad (3.10)$$

The community structure of WSBM retains the stochastic equivalence principle of SBM. In case of WSBM instead of edge-existence probabilities, each edge bundle is now parameterised by a mean and variance i.e.,  $\theta_{z_i z_j} = (\mu_{z_i z_j}, \sigma^2_{z_i z_j})$ . The likelihood function would be,

$$\Pr(A | z, \mu, \sigma^2) = \prod_{ij} N(A_{ij} | \mu_{z_i z_j}, \sigma^2_{z_i z_j}) = \prod_{ij} \exp(A_{ij} \cdot \log\left(\frac{\mu_{z_i z_j}}{\sigma^2_{z_i z_j}}\right) - A^2 \cdot \frac{1}{2\sigma^2_{z_i z_j}} - 1 \cdot \frac{\mu^2_{z_i z_j}}{\sigma^2_{z_i z_j}}) \quad (3.11)$$

Where  $\mu \in R^{k \times k}$  and  $\sigma^2 \in R^{k \times k}$  are model parameters,  $A_{ij}$  is the adjacency matrix,  $\mu_{z_i z_j}$  and  $\sigma^2_{z_i z_j}$  parameterize the weights of edges between community  $z_i$  and  $z_j$ ,  $\Pr(A | z, \mu, \sigma^2)$  denotes the probability of generating the network  $A$  given the

parameters. For each subject, for a given  $n \times n$  adjacency matrix, we estimate WSBM and maximize the likelihood using variational bayes algorithm described by (Aicher , Jacobs , & Clauset, 2015). We select  $k=7$  (number of communities) (Tooley , Bassett, & Mackey, 2022) (Allen E. , et al., 2014) and repeat the optimization procedure 30 times for each subject. We implement the WSBM procedure in MATLAB using freely available code and estimate a weighted stochastic block model for each subject (<https://aaronclauset.github.io/wsbm/>) (Tooley , Bassett, & Mackey, 2022).

### 3.2.7. Measures for community architecture and interaction motifs

WSBM assigns brain areas into communities (Figure 3.1F). We characterize the interaction between communities using interaction motifs described in (Betzel , Medgala , & Bassett, 2018) (Betzel, Bertolero, & Bassett, 2018). One dimension on which we characterized the community interaction was the extent to which detected communities were assortative. The interaction between two communities,  $r$ , and  $s$ , can be characterized by the community densities:

$$\omega_{rr} = \frac{1}{N_r N_r} \sum_{i \in r, j \in r} A_{ij} \quad (3.12)$$

$$\omega_{ss} = \frac{1}{N_s N_s} \sum_{i \in s, j \in s} A_{ij}$$

$$\omega_{rs} = \frac{1}{N_r N_s} \sum_{i \in s, j \in r} A_{ij}$$

Where  $N_r$  and  $N_s$  are the number of nodes assigned to communities  $r$  and  $s$  and  $A$  is the adjacency matrix. Given these community densities, we classify their interactions as follows:

$$M_{rs} = \left\{ \begin{array}{ll} M_{assortative}, & \text{if } \min(\omega_{rr}, \omega_{ss}) > \omega_{rs} \\ M_{core-periphery}, & \text{if } \omega_{rr} > \omega_{rs} > \omega_{ss} \\ M_{core-periphery}, & \text{if } \omega_{ss} > \omega_{rs} > \omega_{rr} \\ M_{disassortative}, & \text{if } \omega_{rs} > \max(\omega_{rr}, \omega_{ss}) \end{array} \right\}$$

Although interaction motifs are defined at the level of communities, the motifs can be mapped and an analogous score for individual brain regions can be calculated. Given a region  $i$ 's community assignment  $z_i$ , its connection density to a community  $r$  is given by

$$a_{ir} = \frac{1}{n_r} \sum_{j \in r} A_{ij} \quad (3.13)$$

Then the regional assortativity score is given by:

$$Assr_{reg} = a_{iz_i} - \max_{r \neq z_i} a_{ir} \quad (3.14)$$

While calculating both regional and community assortativity scores, singleton communities have been excluded (Betzel , Medgalia , & Bassett, 2018).

### 3.2.8. Diversity Index

In addition to studying interaction motif classes (assortative, core, periphery, disassortative), for each motif class, we calculate how frequently it appears among community  $r$ 's interactions. For a  $k$  community partition, community  $r$  participates in  $k - 1$  interaction. The frequencies of appearance can be expressed as

probabilities,  $P_a$ ,  $P_c$ ,  $P_p$ , and  $P_d$  (“assortative”, “core”, “periphery”, “disassortative”) and we can then calculate the entropy as:

$$H_r = -[P_a \log P_a + P_c \log P_c + P_p \log P_p + P_d \log P_d] \quad (3.15)$$

The entropy or Diversity Index is 0 if the community ( $r$ ) participates in only one class and is maximized if  $r$  participates in all classes equally (Betzel, Bertolero, & Bassett, 2018). The resulting score is then assigned to all the nodes  $i \in r$ . We calculate this for all  $k$  communities and estimate mean diversity index by averaging across communities.

### 3.2.9. Morphospace analysis

We adopt this analysis from (Betzel, Medgalia, & Bassett, 2018). A morphospace is a hyperspace whose axes represent the features of the organism or a system. Network morphospace represents the topological properties of a network and helps visualize the richness of the topology (McGhee, 2006). In this study, we construct a community morphospace, whose axes are within-community ( $\omega_{rr}$ ,  $\omega_{ss}$ ) and between-community densities ( $\omega_{rs}$ ). Each point in the morphospace represents a pair of communities,  $r$ , and  $s$ .

### 3.2.10. Ethics statement

The COBRE (The Centre for Biomedical Research Excellence) dataset was obtained through the International Neuroimaging Data-sharing initiative ([http://fcon\\_1000.projects.nitrc.org/indi/retro/cobre.html](http://fcon_1000.projects.nitrc.org/indi/retro/cobre.html)). This was originally released under Creative Commons Attribution Non-Commercial.

### 3.3. Results

We report on how the community architecture and temporal characteristics of functionally connected brain networks can be used as a characterization tool for common mental disorders. The community architecture was assessed using the weighted stochastic block model (WSBM) to uncover the meso-scale community structure from static functional connectivity over the entire time course (see methods section). The WSBM uncovers both assortative and non-assortative community structures (Aicher, Jacobs, & Clauset, 2015). We used three network topology measures that indicate each brain area's participation in assortative, core, or peripheral community interactions (Betzel, Bertolero, & Bassett, 2018) and demonstrate their distinctness across common mental disorders. Temporal properties were studied using the temporal stability of brain networks that are functionally relevant, employing methods developed earlier (Sastry, Roy, & Banerjee, 2023). First, we captured the temporal fluctuations of dynamic functional connectivity with angular distance and construct a *temporal landscape* using temporal stability matrices. This was followed by the computation of entropy and global temporal distance, which quantifies the informational content in these matrices and serves as a defining characteristic for different mental health disorders such as schizophrenia, ADHD, and bipolar disorder. The first section presents the results of the community architecture analysis, second section presents results of temporal stability analysis for *dataset 1* (Poldrack, et al., 2016) across various mental health disorders, including schizophrenia, ADHD, and bipolar disorder. To ensure validity and robustness, we repeat the entire pipeline on *dataset 2* (Bellec, 2016) and demonstrate the results specifically for participants with schizophrenia in the third section.

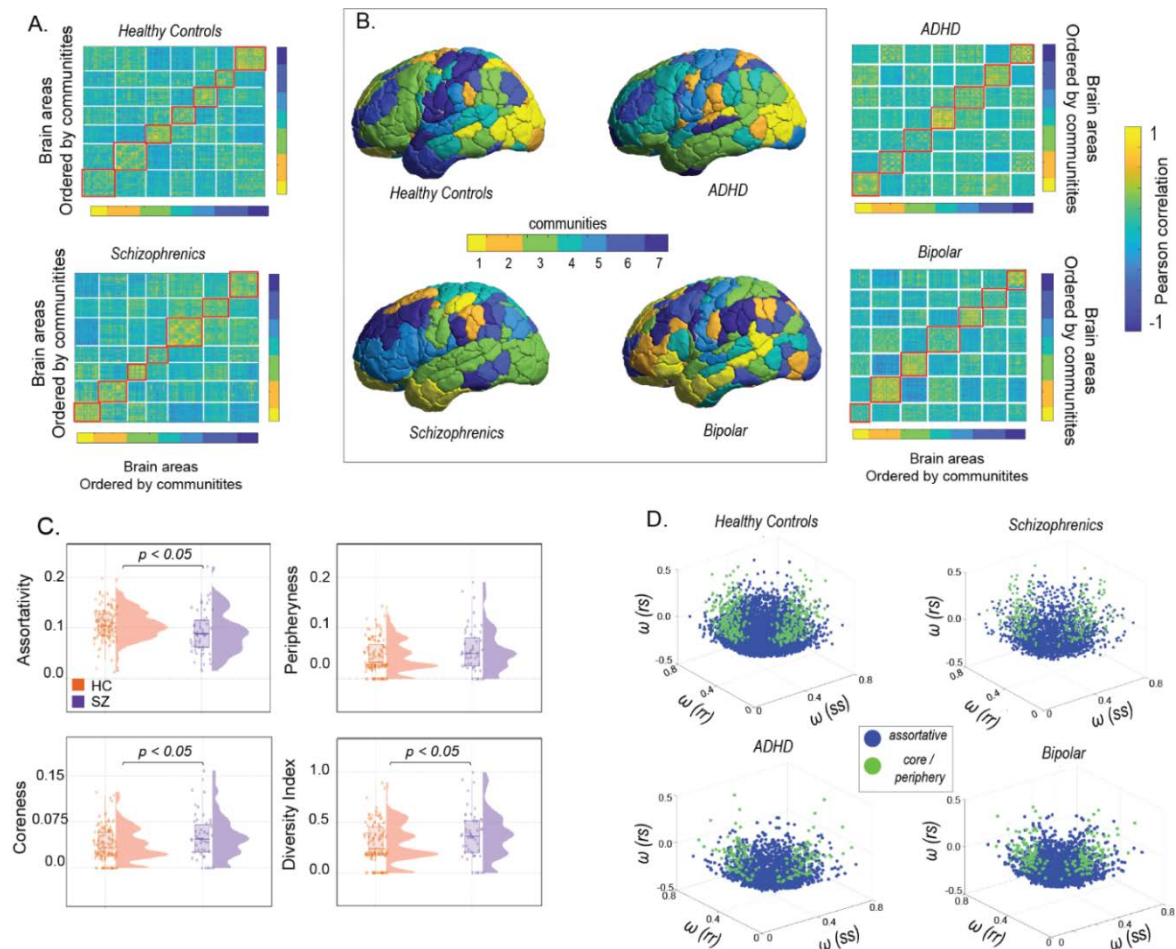


**Figure 3.2** An overview of the community architecture differences between schizophrenics and healthy controls in Dataset 1 (A) shows the static functional connectivity matrices of schizophrenics and healthy controls, with brain areas ordered by communities (B) presents the partition of cortical regions into 7 communities using the Weighted Stochastic Block Model (WSBM), a generative community detection algorithm that groups stochastically equivalent brain regions into communities (C) each pair of communities ( $r$  and  $s$ ) is classified into one of three community motifs: assortative, coreness, and peripheryness. The diversity index is calculated as the average across all brain regions per subject. The violin plots indicate that in schizophrenics, communities are less assortative (D) illustrates the construction of a network morphospace using all pairs of communities, which are coloured according to their motif type: blue for assortative community interactions and green for core or periphery community interactions.

### 3.3.1. Distribution of community architecture of brain networks across common mental disorders

The organization of neural elements into motifs, communities, and clusters – collectively comprise the meso-scale structure of the brain and, in turn drive the complex inter-community interactions that enrich the diverse functional connectome (Betzel , Medgalia , & Bassett, 2018). In this section, we investigate the differences in community structure and interactions, between cohorts of common mental health disorders - schizophrenics/ ADHD / bipolar and healthy controls.

First in *Dataset 1*, for each subject in both diseased and healthy cohort, we fit a weighted stochastic block model (WSBM) on the adjacency matrix computed from FC (see Methods for details on WSBM and network construction). Here, we report results for the fittings in which the number of communities were considered at  $k=7$ . Earlier studies, using clustering algorithms (Allen E. , et al., 2014), WSBM (Tooley , Bassett, & Mackey, 2022) report optimal solution at  $k=7$  which guided us to set the specific value. Figure 3.2A depicts the community partitions in FC observed for both diseased and healthy individuals. Figure 3.2B depicts a topographic representation of communities detected with WSBM and their assignment for given brain areas, in individuals with schizophrenia, ADHD, bipolar disorders and healthy controls. As expected, brain areas were distinctly assigned to different communities in diseased and healthy controls (Figure 3.2B). Community motifs represent interactions among pairs of communities. The interactions can be – assortative, core or periphery community interactions. In assortative communities, the internal density of connections within subnetworks exceeds their external density whereas core-periphery organization consists of a central core which is connected to the



rest of the subnetworks and peripheral nodes connect to the core but not with each other (Betzler, Bertolero, & Bassett, 2018). Here in the main manuscript, we report only significant group-level community interaction measures averaged across communities. Figure 3.2C reports significantly lower assortativity in schizophrenics ( $P=0.0121$ ,  $t=2.5374$ ) compared to healthy controls. The distributions were parametric and unpaired t-test was used to assess significance. Rank sum test (the distribution was non-parametric) revealed a significantly higher coreness in schizophrenics ( $P=0.0188$ ) compared to healthy counterparts. In addition to this, we mapped the motif participation index for individual brain areas and compute the diversity index (see methods) – measuring the entropy across each brain area's motif participation. Figure 3.2C reveals a significantly higher diversity index in schizophrenics (*unpaired t-test*,  $P=0.0354$ ,  $t = -2.1207$ ) indicating communities in schizophrenics, by and large, participate in more than one motif class. Although we see distinct modifications in community interaction motifs for both Bipolar and ADHD (see supplementary A 3.1) participants in comparison to healthy controls, the results were non-significant. Next, we construct a 3D community morphospace – each point in the morphospace represents a pair of communities  $\{r,s\}$ , and the axes are defined by within-community and between-community densities,  $\omega_{rr}$ ,  $\omega_{rs}$ ,  $\omega_{ss}$ . Morphospace allows us to investigate how the community interactions generate assortative and non-assortative architecture. We compared morphospace constructed for both diseased and healthy controls – individuals with schizophrenia, ADHD and bipolar disorder favoured fewer assortative but included more core-periphery community interactions than healthy controls (Figure 3.2D). Overall, the community motifs and morphospace analysis indicate community

structure in common mental disorders, especially in schizophrenics is less assortative.

Next, to identify disease-specific assortativity changes in brain regions, we calculate an analogous assortativity score for each brain region (see methods) (Betzel , Medgalia , & Bassett, 2018). We performed this analysis in patients with schizophrenia, ADHD and bipolar disorders from *Dataset 1*. To identify disease-specific changes in region-wise assortativity, we first generate age-matched, sex-matched healthy controls for each of the disease groups. For each brain region, we perform a *t-test* between assortativity scores of patients and matched healthy controls with age and sex regressed out. For schizophrenics, assortativity decreased significantly in peripheral visual, Dorsal attention, Ventral attention, and Temporal parietal networks (Table 3.2) whereas for individuals with ADHD, assortativity decreased significantly in central visual, limbic, dorsal attention, default, and control networks (Table 3.4). In individuals with bipolar disorder, significant assortativity reduction was seen in dorsal and ventral attention, limbic and default networks (Table 3.3). Figure 3.3A-C shows brain-wide topography of significant assortativity scores between patients with ADHD, bipolar disorder, schizophrenia and healthy controls.

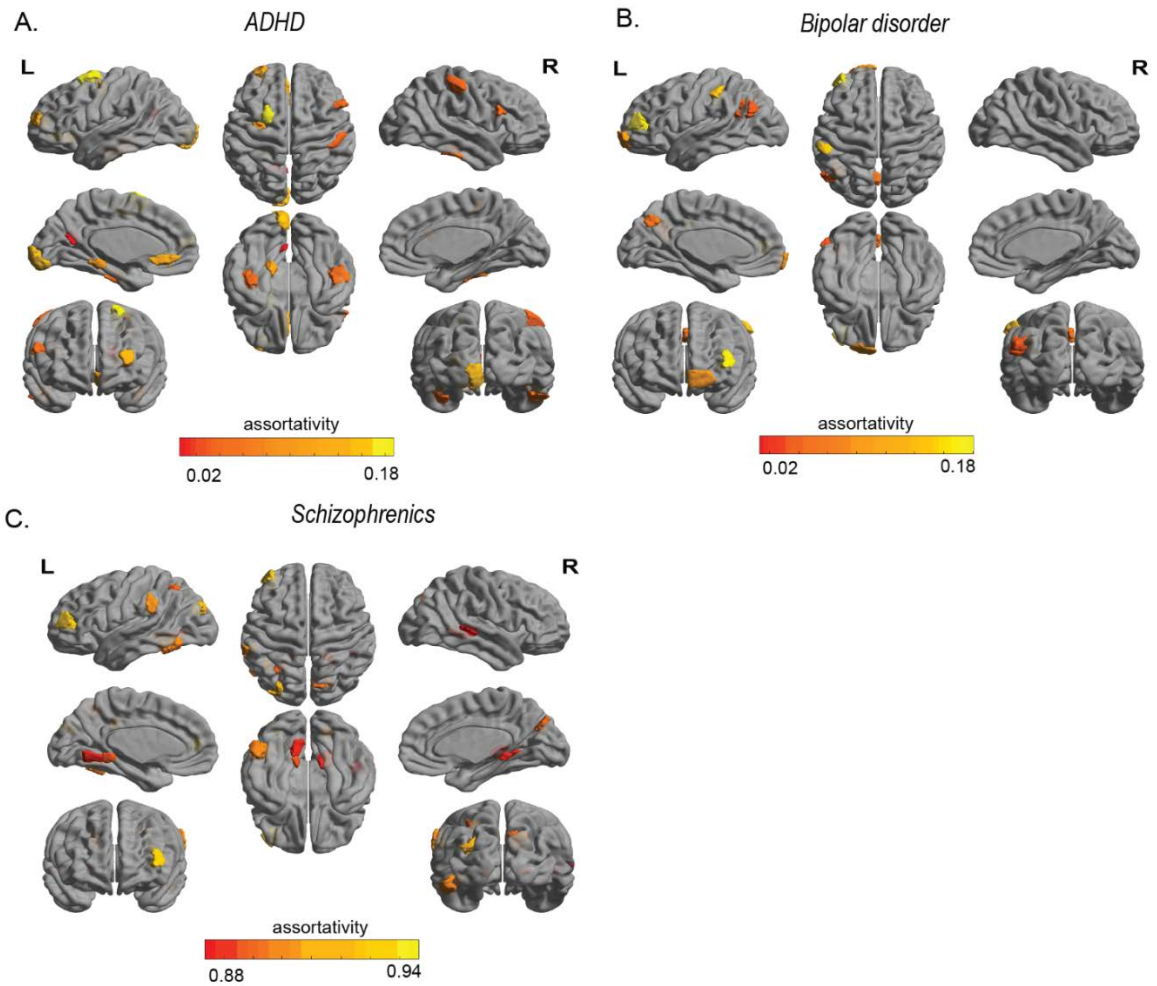


**Figure 3.3 Profile of brain regions showing significant difference in assortativity between patients, age and sex matched healthy controls (A) ADHD (B) bipolar disorder (C) Schizophrenia.**

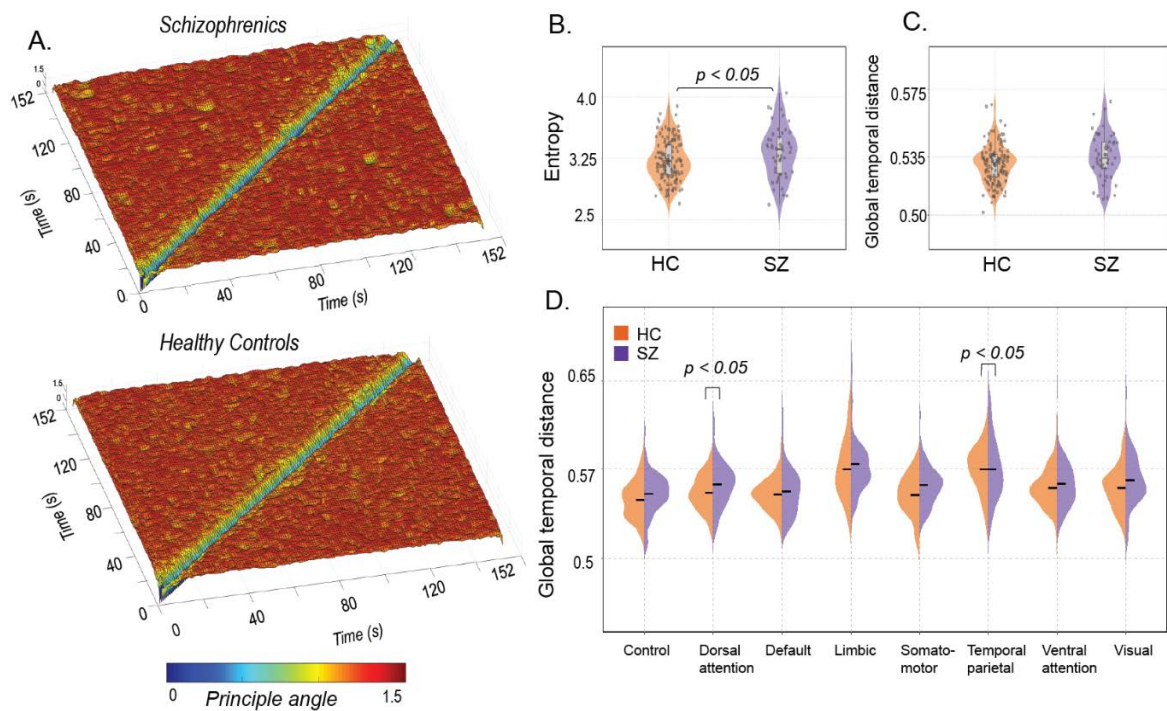


**Figure 3.4** An overview of the temporal stability differences between schizophrenia and healthy controls in Dataset 1 (A) showcases the Time X Time temporal stability matrices, visualized as the 'Temporal landscape'. Each entry represents the angular distance between dominant dFC subspaces at time points  $t_x$  and  $t_y$ , for patients with schizophrenia and healthy controls. In schizophrenics, there is a global spread of shorter-lived, low angular distant (yellow hue) repeated patterns of stability (B) focuses on quantifying temporal stability across the entire Time X Time temporal landscape using entropy (C) quantifies temporal stability over successive time points using global temporal distance. Both measures indicate low temporal stability in schizophrenics (D) global temporal distance is estimated for all the resting state networks defined in the Schaeffer atlas, comparing schizophrenics (purple) and healthy controls (orange).

*Table 3.2 Region wise significant assortativity differences in patients with schizophrenia, age and sex matched healthy controls*

Brain regions (ROI number)	Controls	Patient	P value
Peripheral visual (14)	0.933333	0.886667	0.02618
Peripheral visual (16)	0.926667	0.9	0.03743
Peripheral visual (217)	0.926667	0.886667	0.03239
Peripheral visual (222)	0.94	0.906667	0.0004645
Dorsal attention A (62)	0.93	0.913333	0.04117
Dorsal attention A (65)	0.926667	0.926667	0.004987
Dorsal attention A (69)	0.943333	0.903333	0.02541
Ventral attention/ (88) Salient network	0.946667	0.916667	0.01481
Ventral attention/(101) Salient network	0.933333	0.933333	0.01064
Temporal parietal (395)	0.913333	0.873333	0.007664

*Table 3.3 Region wise significant assortativity differences in patients with bipolar disorder, age and sex matched healthy controls*

Brain Region (ROI number)	Controls	Patients	P value
Dorsal attention B (75)	0.92517	0.921769	0.04821
Ventral attention B (101)	0.918367	0.908163	0.04906
Limbic B (113)	0.880952	0.918367	0.001511
Default A (149)	0.911565	0.918367	0.04192
Default A (159)	0.911565	0.908163	0.01705
Default B (173)	0.914966	0.897959	0.0275

*Table 3.4 Region wise significant assortativity differences in patients with ADHD, age and sex matched healthy controls*

Brain Regions (ROI number)	Control	Patient	P value
Central visual (7)	0.9	0.933333	0.02668
Dorsal attention B (84)	0.904167	0.870833	0.02501
Limbic A (118)	0.866667	0.866667	0.04766
Control A (127)	0.941667	0.9375	0.02998
Control B (142)	0.9	0.925	0.04677
Default A (162)	0.891667	0.858333	0.02264
Default C (191)	0.916667	0.883333	0.03971
Default C (194)	0.870833	0.85	0.04202
Somatomotor A (227)	0.929167	0.9	0.04864
Limbic A (324)	0.870833	0.875	0.04558
Control A (331)	0.9125	0.9	0.02631

### 3.3.2. Impaired and preserved patterns of temporal stability in common mental disorders: schizophrenia, ADHD and bipolar

To compute the temporal stability of dFC, the first step involved estimating the similarity/differences between dominant dFC subspaces by calculating the angular distance between them ( $(\phi(t_x, t_y))$ , see equation 4, Methods). The resulting temporal stability matrix, spanning time X time, characterizes the collective temporal characteristics of dFC and aids in visualizing the *temporal landscape*. A low angular distance between subspaces indicates that the corresponding dFC patterns were similar in configuration, while a high angular distance suggests dissimilarity (Sastry, Roy, & Banerjee, 2023). In this section, we present the results

of evaluating temporal stability changes between healthy controls and cohorts with common mental disorders (such as schizophrenia, ADHD, and bipolar disorder) in *Dataset 1*.

Group-level averages of temporal stability, computed on resting state fMRI BOLD time series from healthy controls and individuals with schizophrenia, are reported in Figure 3.4A. In schizophrenics, a global spread of shorter-lived, low angular distant (yellow hue) repeated patterns of stability was observed. Conversely, healthy controls exhibited a more evenly distributed, repeated pattern of stability. To quantify these differences across the entire landscape, we calculated the entropy of temporal stability matrices. Figure 3.4B illustrates the higher entropy of temporal stability matrices in schizophrenics compared to healthy controls, indicating impaired temporal stability in individuals with schizophrenia. The distributions were assessed parametrically using the Jarque-Bara test and D'Agostino-Pearson omnibus test. A two-sample t-test revealed significant differences in entropy values between healthy controls and individuals with schizophrenia ( $P=0.0475$ ,  $t=-1.9963$ ). Next, to quantify stability differences over successive time windows, we calculated the global temporal distance (see Methods for details). Although the results (Figure 3.4C) were not statistically significant (Wilcoxon rank-sum test,  $P=0.8902$ ), the violin plots suggest a trend: individuals with schizophrenia exhibit higher global temporal distance compared to healthy controls. Furthermore, for each of the 8 resting state networks (RSNs) defined in the Schaeffer atlas (Schaeffer, et al., 2018), we estimated the dominant dynamic functional connections (dFC) and constructed temporal stability matrices for participants in both the schizophrenia and healthy control groups. Additionally, we calculated entropy (see Supplementary, A 3.3A) and global temporal distance

(Figure 3.4C) specific to the 8 resting state networks (Control, Dorsal attention, Default, Limbic, Somatomotor, Temporal parietal, Ventral attention, and Visual networks). Figure 3.4D shows significantly higher global temporal distance in individuals with schizophrenia in two networks: 1) Dorsal attention network, indicating significantly lower temporal stability in schizophrenics ( $P=0.0153$ ,  $t=-2.4489$ ) (The distributions were assessed parametrically using an unpaired two-sample t-test) and 2) Somatomotor network, indicating significantly lower temporal stability in individuals with schizophrenia ( $P=0.0109$ ) (The distributions were non-Gaussian; hence, the Wilcoxon rank-sum test was used). Overall, these results indicate impaired temporal stability in individuals with schizophrenia, both at the whole-brain level and within specific networks.

Next, we investigate changes in temporal stability in patients with other common mental disorders, including ADHD, Bipolar disorder, and healthy controls from *Dataset 1*. Firstly, for each participant, we construct whole-brain temporal stability matrices by estimating  $\phi(t_x, t_y)$  across all timepoints. Figure 3.5A illustrates the temporal landscape of participants with ADHD and Bipolar disorder. The results indicate a minimal spread of low angular distant (yellow hue) and repeated patterns of stability in both ADHD and Bipolar disorder. We observed significantly lower entropy in participants with ADHD (two-sample t-test,  $P=0.0162$ ,  $t=-2.4293$ ), while global temporal distance was significantly higher (Wilcoxon rank-sum test,  $P=2.2128e-21$ ), indicating impaired temporal stability in patients with ADHD (Figure 3.5B). In the case of bipolar disorder, our results indicate high entropy (two-sample t-test,  $P=0.3467$ ,  $t=0.9436$ ) and global temporal distance (two-sample t-test,  $P=0.8892$ ,  $t=0.1395$ ) in temporal stability matrices, although these findings were not statistically significant.



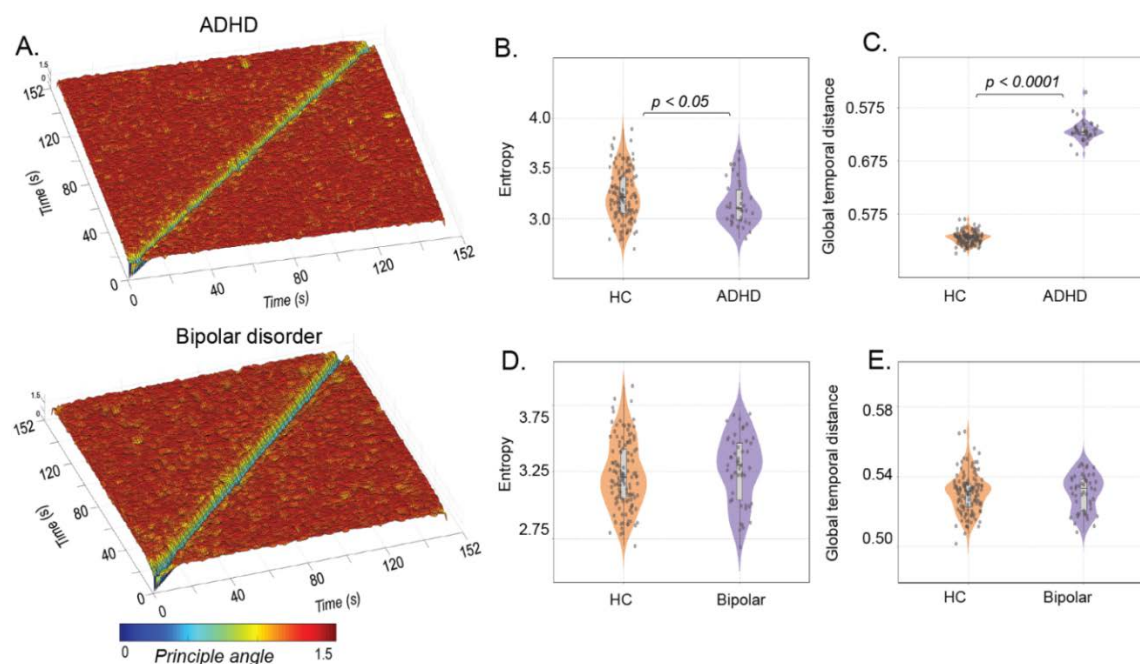


**Figure 3.5 An overview of the temporal stability differences in participants with ADHD and Bipolar disorder** (A) showcases the Time X Time temporal stability matrices, where each entry represents the angular distance between dominant dFC subspaces at time points  $t_x$  and  $t_y$ , for participants with ADHD and Bipolar disorder. The temporal stability is quantified using two measures: entropy (B) and global temporal distance (C) in patients with ADHD and healthy controls. The results show that global temporal distance is significantly higher in participants with ADHD, indicating decreased temporal stability. Similarly, temporal stability is quantified using entropy (D) and global temporal distance € in participants with bipolar disorder and healthy controls.

### 3.3.3. Validation Analysis

Furthermore, we replicated the entire analysis pipeline using *Dataset 2*. Firstly, at the single-subject level, we identified communities by fitting the weighted stochastic block model (WSBM) to adjacency matrices obtained from static functional connectivity (FC) (see Supplementary, A 3.2A). We investigated community interaction motifs and found that assortativity was significantly lower in individuals with schizophrenia (Wilcoxon rank-sum test;  $P=0.0483$ ) compared to their healthy counterparts, while coreness (Wilcoxon rank-sum test;  $P=0.0209$ ) and peripheryness (Wilcoxon rank-sum test;  $P=0.0043$ ) were significantly higher. The

diversity index was also significantly higher in individuals with schizophrenia (Wilcoxon rank-sum test,  $P = 0.0184$ ) (A 3.2B), indicating that brain areas participate in more than one motif class. Additionally, we constructed a 3D community morphospace, where the axes were defined by within-community and between-community densities,  $\omega_{rr}$ ,  $\omega_{rs}$ ,  $\omega_{ss}$ . Our results with the morphospace (A 3.2C) demonstrated that communities in individuals with schizophrenia favoured fewer assortative interactions compared to healthy controls, thus validating our findings from *Dataset 1*, specifically in patients with schizophrenia. Next, we construct temporal stability matrices (Figure 3.6A) and calculate entropy and global temporal distance for individuals with schizophrenia and healthy controls. Figure 3.6B reports significantly higher entropy in individuals with schizophrenia ( $P=0.0373$ ) compared to healthy controls. The distributions were non-parametric (normalcy test performed with Jarque-Bara test, and significance tested with Wilcoxon rank-sum test). Global temporal distance (Figure 3.6C) was also significantly higher in individuals with schizophrenia compared to healthy controls (Wilcoxon rank-sum test;  $P=2.5559e-04$ ). Both the entropy and global temporal distance results indicate impaired temporal stability in individuals with schizophrenia, thus validating our initial findings from *Dataset 1*. At the network level analysis (Figure 3.6D), we observe significantly higher global temporal distance in individuals with schizophrenia in the Control network ( $P=5.5055e-04$ ), Dorsal attention network ( $P=0.0057$ ), Default network ( $P=0.0048$ ), Somatomotor network ( $P=8.021e-04$ ), Temporal-Parietal network ( $P=0.0106$ ), and Ventral attention network ( $P=0.0042$ ). The distributions were non-parametric, and significance was tested with the Wilcoxon rank-sum test.

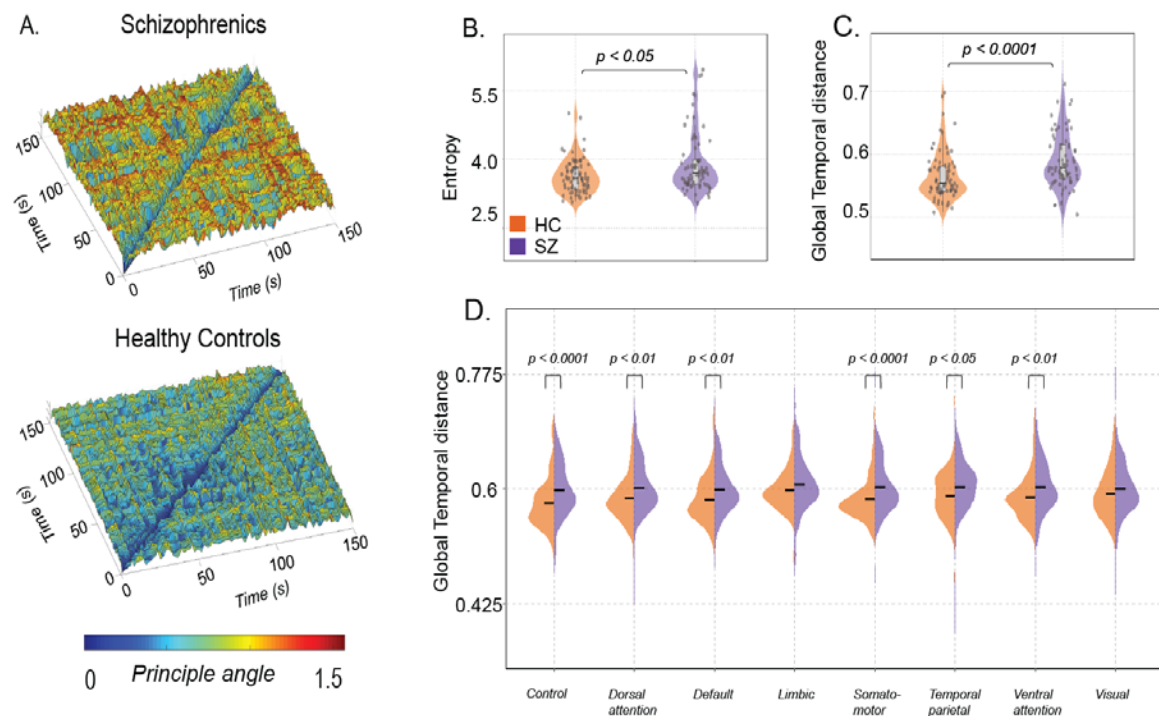


**Figure 3.6** An overview of the temporal stability differences between individuals with schizophrenia and healthy controls in Dataset 2. (A) illustrates the temporal stability matrices, visualized as a temporal landscape, for both schizophrenics and healthy controls. Each entry in the matrix represents the angular distance between dominant dFC subspaces at time points  $t_x$  and  $t_y$ . The angular distance ranges from 0 (indicated by yellow hue) to  $\pi/2$  (indicated by red hue) (B) quantifies the temporal stability across the entire temporal landscape using entropy (C) quantifies the temporal stability over successive time windows using global temporal distance. Both measures indicate a decrease in temporal stability in schizophrenics, which aligns with the findings from Dataset 1. (D) estimates the global temporal distance for each of the resting state networks defined in the Schaeffer atlas for both individuals with schizophrenia (purple) and healthy controls (orange). The plots demonstrate a significant decrease in temporal stability in schizophrenics, particularly in the control, dorsal attention, default, somatomotor, temporal parietal, and ventral attention networks.

### 3.4. Discussion

The current study aimed to explore the potential of dFC measures as characterizing tools for common mental disorders, including schizophrenia, ADHD, and bipolar disorder. Our findings revealed interesting insights into the spatiotemporal architecture of the dynamic functional connectome. Firstly, we utilized two datasets of individuals with common mental health disorders (total N=408 participants) to investigate differences in the community structure of the functional connectome. We employed a generative model-based community detection algorithm, weighted stochastic block model (WSBM) (Aicher , Jacobs , & Clauset, 2015) to identify communities and map their interactions into assortative, coreness, and peripheryness motifs. Our findings indicate that in individuals with schizophrenia, communities participate in more than one community motif and exhibit lower assortativity compared to healthy individuals (Figure 3.2 and *supplementary A 3.2*). Moreover, when comparing across diseases with age and sex-matched healthy controls, we identified specific brain areas that showed significant differences in assortativity (Figure 3.3). While our findings revealed altered community interactions in individuals with ADHD and bipolar disorder (see *supplementary A 3.1*), these differences did not reach statistical significance. To address this limitation we went beyond modifications in the community structure and investigated alterations in the dynamic functional connectome across these disorders by employing a novel methodology proposed by (Sastry, Roy, & Banerjee, 2023). This approach leverages the dynamic nature of functional connectivity to construct a temporal landscape and assess the temporal stability of resting-state dFC in participants with ADHD, bipolar disorder, schizophrenia, and healthy controls. We used entropy and global temporal distance as measures of

temporal stability. Our results demonstrated a significant increase in entropy of the whole-brain temporal landscape and specific resting-state networks (such as the dorsal attention and somatomotor networks) in individuals with schizophrenia, indicating decreased temporal stability of dFC. We extended our analysis to include participants with ADHD and bipolar disorder, revealing a significant decrease in temporal stability among ADHD participants (Figure 3.5). Notably, both the temporal stability and community architecture differences in individuals with schizophrenia were consistent across the two datasets used (Figure 3.6).

Using two resting-state fMRI datasets (Total N=408), the current study investigated the differences in community structure between individuals with mental disorders (schizophrenia, ADHD, bipolar disorder) and healthy controls. Earlier studies have reported alterations in community structure in common mental disorders, particularly in schizophrenia. (Alexander-Bloch, et al., 2010) reported decreased modularity in functional brain networks in individuals with schizophrenia. (Lerman-Sinkoff & Barch, 2016) using NMI, identified significant differences in community structure between healthy controls and individuals with schizophrenia, with subcortical, auditory, and somatosensory networks being major contributors to these changes. However, previous studies on the community structure of resting-state functional connectivity (FC) in individuals have been limited by methodological biases associated with modularity maximization and infomap techniques, which are designed to uncover only assortative communities (Betzel, Medgalia, & Bassett, 2018). In this study, we used the weighted stochastic block model (WSBM), a data-driven generative community detection algorithm capable of uncovering assortative and non-assortative communities at the mesoscale level (Betzel, Medgalia, & Bassett, 2018). As expected, WSBM uncovered distinct

communities in diseased and healthy controls (Figure 3.2B and A 3.2A). In our analysis, we classified community interactions into assortative, core, and periphery motif classes. Our results demonstrated that communities in individuals with mental disorders, particularly schizophrenia, exhibited significantly less assortativity, higher coreness and peripheryness (Figure 3.2C, Figure 3.2D and A 3.2) compared to healthy controls. The Diversity Index, a motif participation index, was significantly higher in individuals with schizophrenia, indicating that communities participated in more than one motif class (Figure 3.2C and A3.2 B). Our research has revealed significant changes in assortativity at the regional level in three common mental health disorders: schizophrenia, bipolar disorder, and ADHD. These findings offer potential evidence for the underlying neuropathological profiles of these diseases. Previous studies in schizophrenia, investigating modularity have identified disruptions in modular structure in sensory, auditory, and visual areas (Bordier , Nicolini , Forcellini , & Bifone , 2018), right insular and perisylvian cortical areas (Alexander-Bloch , et al., 2012). In line with these studies, our findings in schizophrenia show significantly lower assortativity in communities associated with peripheral visual, dorsal and ventral attention, and temporal parietal networks (Figure 3.3C) (Table 3.2). (Lin , et al., 2014) reported decreased brain network integration and increased network segregation in ADHD patients, along with significant alterations in local clustering coefficients in cerebellar, frontal, motor, and temporal regions. In our study, we found significant alterations in assortativity in brain areas belonging to central visual, limbic, default, and somatomotor networks in ADHD patients (Figure 3.6A) (Table 3.4) Studies on bipolar disorder have identified alterations in brain network topology in frontoparietal and limbic networks (Zhang , et al., 2021). Similarly, our findings

indicate significantly lower assortativity in brain areas associated with the default and dorsal attention networks, as well as limbic networks, in bipolar disorder patients (Figure 3.3B) (*Table 3.3*). Overall, these region-level alterations align with previous studies and suggest that alterations in community structure play a role in the neuropathology of common mental health disorders. Although we attempted to replicate our community detection and interaction motif analysis in patients with ADHD and bipolar disorder, our results did not yield statistical significance. We hypothesized that the lack of statistical significance in our results, along with the relatively small number of participants, could be attributed to the dependency of most community detection algorithms on static functional connectivity. (Preti, Bolton, & De ville, 2017) have highlighted the limited scope of static functional connectivity and its inability to fully capture the dynamic nature of brain activity. To explore the dynamic characteristics of the resting-state dynamic functional connectome and its alterations in common mental disorders, our study focused on estimating the temporal stability of these dynamic patterns. In this study, along with a companion report (Sastry, Roy, & Banerjee, 2023), we employed a methodology where, at each timepoint, we first extracted dominant dynamic functional connectivity (dFC) patterns and projected them into dFC subspaces using PCA. We then assessed the similarity of these patterns by calculating the angular distance between the subspaces (Figure 3.1C). We introduce two measures to quantify temporal stability: 1) Entropy, which estimates temporal stability across the entire temporal landscape and all time points, and 2) Global temporal distance, which measures temporal stability across successive time points. While previous studies have explored regional variations in temporal stability (Zhang , et al., 2016) (Dong , et al., 2019), our study extends this exploration by quantifying temporal

stability at both the whole-brain and brain network level. Our key finding is a significant decrease in temporal stability among individuals with schizophrenia, both at the whole-brain and network levels. Our results in both *Dataset 1* and *Dataset 2* indicate increased entropy (Figure 3.4B) (Figure 3.6B) and global temporal distance (Figure 3.4C) (Figure 3.6C) of the whole-brain functional connectome in individuals with schizophrenia, which suggests impaired temporal stability. Our findings also indicate impaired temporal stability in individuals with schizophrenia in several networks, including the dorsal attention, Somatomotor, limbic, ventral attention, control, and temporal-parietal networks (Figure 3.4D and Figure 3.6D). These results are consistent with previous studies that have investigated the regional temporal variability of dFC in schizophrenia. (Zhang , et al., 2016) found that patients with schizophrenia exhibited significantly increased temporal variability (decreased temporal stability) of dFCs in subcortical regions, such as the thalamus, palladium, and visual areas during resting state. Similarly, (Dong , et al., 2019), (Gifford , et al., 2020) and (Long , et al., 2020) using flexibility measures, observed significant impairment in temporal stabilities of dFC in multiple brain areas, including the thalamus, visual areas among individuals with schizophrenia. In line with these previous studies, our results showing significant impairment in temporal stability of dFCs at both the whole-brain and network level contribute to a better understanding of the temporal stability differences observed in schizophrenia. ADHD is characterized by dynamic reconfiguration of the functional connectome (Lin , et al., 2014) (Fair , et al., 2010) . (Zhang , et al., 2016) (Castellanos , et al., 2008) report increased temporal variability (decreased stability) in default-mode network and lower temporal variability in subcortical regions in patients with ADHD. Our findings show a significant increase in the



global temporal distance of whole-brain functional connectome in patients with ADHD, suggesting decreased temporal stability of whole-brain dFCs (Figure 3.5B). Similar to schizophrenia and ADHD, there are multiple studies on temporal stability modifications in bipolar disorder patients that report shared similarities in temporal stability alternations with schizophrenia (Long , Lu, & Liu, 2023) (Han , et al., 2020) (Nguyen , et al., 2017). Although our results show changes in temporal stability in individuals with bipolar disorder, the results were not statistically significant. Overall, these findings in common mental health disorders, validated across two datasets, especially in schizophrenia, point to a significant widespread decrease in the temporal stability of dFCs both at the whole-brain and network levels. Our results further suggest that these widespread alterations in dynamic functional network configurations, captured by dynamic measures such as temporal stability, provide a comprehensive representation of brain dynamics and reflect the dynamic nature of mental disorders. They may serve as a more promising potential biomarker for common mental health pathologies.

It is important to note a few methodological limitations of the present study. The generative community detection algorithm, WSBM, used in this study requires that the number of communities,  $K$ , be specified by the user. Accordingly, because the simulations are time and memory intensive, based on evidence from earlier studies, (Tooley , Bassett, & Mackey, 2022) (Allen E. , et al., 2014) we reasonably chose to run the simulations for  $K=7$ . Our results are limited in part, by the length of fMRI scan sessions as well. In both datasets, the scan durations are ~5 mins and there were relatively few timepoints (150 volumes) which may restrict dynamic functional connectivity estimation. A meaningful extension of the present work would be to investigate the potential of temporal stability to be used as a 'feature'

in classifying common mental health disorders by building unsupervised classification algorithms.

### **3.4.1. Conclusion**

This study highlights the significance of dynamic functional connectivity (dFC) and temporal stability in characterizing common mental disorders. While the community architecture of functionally connected brain networks, assessed using the weighted stochastic block model (WSBM), shows discernible patterns between individuals with mental disorders and healthy controls, the study faced challenges in clearly distinguishing between different disorders. The measurements of assortativity, coreness, and motif participation index provide valuable insights into community interactions but did not result in distinct separation between disorders. However, temporal stability analysis, through angular distance, global temporal distance and entropy calculations, uncovers impaired stability in schizophrenia and ADHD, while bipolar disorder shows notable differences. These findings underscore the crucial role of dFC and temporal stability in understanding and characterizing common mental disorders, offering potential insights into their underlying mechanisms and potential diagnostic markers.

## Chapter 4

# Towards translational low-field neuroimaging

### 4.1 Introduction

Magnetic resonance imaging (MRI) has been revolutionary in brain research, offering non-invasive, high-resolution neuroimaging with versatile soft-tissue contrast. MRI stands as a prominent tool for non-invasive evaluation of human anatomy and physiological processes, particularly in brain assessment. The continuous evolution of imaging technology (Sejowski , Churchland , & Movshon , 2014), coupled with refined analysis techniques and the widespread sharing of data (Poldarck, et al., 2017), has propelled significant advancements in comprehending both the structure and function of the brain (Park & Friston , 2013). This knowledge extends to both healthy states and pathological conditions, fostering a deeper understanding of neurological complexities (Fornito , Zalesky , & Breakspear, 2015). However, despite these achievements, the complete realization of MRI's clinical potential remains pending. A key hindrance is the considerable size of MRI scanners and their reliance on intricate infrastructures, rendering them financially prohibitive to establish and operate. Consequently, this limitation hampers the widespread integration of MRI technology in regions with limited resources, such as low- and middle-income countries (LMIC), where the prevalence of neurological disorders is high (IAEA, 2021). Furthermore, the utilization of MRI for bedside scanning of critically ill patients is also impeded. Addressing this challenge would not only promote equitable healthcare access

globally but also open avenues for expedited diagnosis and treatment in critical cases. Recognizing these barriers and actively seeking solutions for portable and cost-effective MRI technology could significantly extend its reach, offering transformative benefits to healthcare systems worldwide.

Advancements in technology have recently ushered in the era of (ultra-)low-field MRI scanners (for example Low-field hyperfine MRI scanners), offering the promise of portable imaging solutions at significantly reduced costs (Cooley , et al., 2021) (sheth , et al., 2021) (O'Rilley , Teeuwisse , De gans , Koolstra , & Webb, 2021) (Turpin , et al., 2020). These scanners utilize permanent magnets, eliminating the need for cryogenic systems and minimizing external power requirements. They can be operated using standard power outlets. It is noteworthy that the adoption of such systems comes with trade-offs. The magnetic field strength of these scanners is notably lower, ranging from 0.050 to 0.080T, in stark contrast to the conventional MRI's 1.5-3T. As a result, the achievable image quality experiences a corresponding reduction. Furthermore, the extent to which low-field imaging data can be correlated to traditional MRI data remains uncertain (O'Rilley , Teeuwisse , De gans , Koolstra , & Webb, 2021). This includes its compatibility with intricate quantitative analysis techniques that are integral to advanced imaging studies. While these novel low-field scanners hold great promise in terms of portability and cost-effectiveness, their capacity to produce diagnostically valuable images and facilitate rigorous quantitative assessments is an ongoing area of exploration. As technological advancements continue and methods for enhancing image quality and data comparability are refined, the full potential of (ultra-)low-field MRI scanners in both clinical and research contexts could be realized (Turpin , et al., 2020).

Concurrently, recent strides in machine and deep learning have ushered in swift and dependable processing of MRI data, automating an array of tasks. These encompass aligning scans with templates (Hoffman , Billot , Iglesias , Fischl , & Dalca , 2020), segmenting images into distinct tissue classes (Billiot , Robinson , Dalca , & Iglesias , 2020) (Insensee, Jaeger , Kohl , Peterson , & Maier-Hein , 2021) and deriving quantitative characteristics from regions of interest (Henschel , et al., 2020). A particularly promising facet of deep learning lies in its ability to perform image quality transfer (IQT). This technique achieves super-resolution of scans by learning and then transferring information from higher-resolution images to their lower-resolution counterparts. IQT has chiefly been utilized to synthesize 1mm isotropic images from thick-slice clinical scans acquired at 1.5T (Iglesias , et al., 2021). Additionally, it has been employed to synthesize submillimetre-resolution images from 3T scans, capitalizing on information gleaned from ultra-high-field (7T) imaging (Quiyuan , et al., 2021). The prospects of IQT are immense, particularly in enhancing the resolution and quality of low-field scans. This advancement can bolster their clinical diagnostic utility both through qualitative visual assessment and quantitative processing, facilitating feature extraction. The integration of IQT with machine learning methodologies has the potential to ameliorate the performance of low-field MRI scans, overcoming some of the limitations posed by lower magnetic field strengths (Iglesias , et al., 2021).

Quantitative imaging encompasses intricate image processing workflows involving tasks such as registration, segmentation, and visualization, becoming progressively sensitive to potential image artifacts. Consequently, a prerequisite for effective quantitative postprocessing is the elimination of image artifacts beforehand, enhancing robustness and efficiency. This challenge is particularly

pronounced in ultrasound and magnetic resonance imaging (MRI), especially when dealing with subtle structures that exhibit signals just above the noise threshold. Furthermore, the evolution of quantitative medical imaging necessitates the analysis of larger 3-D datasets to discern meaningful discriminants for specific pathologies (Mazziotta , et al., 2001). To accommodate this, intricate automatic image processing workflows that are impervious to diverse image qualities and parameter variations are required (Coupe P. , et al., 2007). Numerous techniques have been proposed for preserving edges while denoising images. Widely used methodologies encompass Bayesian approaches (Geman & Geman , 1984), partial differential equation (PDE)-based methods (Perona P & Malik , 1990) (Rudin , Osher , & Fatemi , 1992), robust and regression estimation (Black & Sapiro , 1999), adaptive smoothing (Saint-Marc, Chen , & Medioni , 1991), wavelet-based methods (Donoho & Johnstone , 1994), bilateral filtering (Tomasi & Manduchi, 1998), and hybrid approaches (Coupe P. , et al., 2007). Recent innovations include statistically enhanced averaging schemes that incorporate variable spatial neighbourhood strategies. Other strategies involve modelling non-local (NL) pairwise interactions from training data or a library of natural image patches (Coupe P. , et al., 2008). The focus of this work is on the utilization of the NL-means filter, originally introduced by (Baudes , Coll, & More , 2005) (Coupe P. , et al., 2007). The NL-means filter exploits the redundancy property of periodic, textured, or natural images to eliminate noise. Unlike traditional methods that rely on spatial proximity, the weight assigned to averaging voxels in this approach is rooted in the intensity similarity of their neighbourhoods to the neighbourhood of the voxel under scrutiny, akin to patched-based methodologies. Essentially, the NL-means filter can be perceived as an extreme case of neighbourhood filters with an infinite spatial

kernel, where neighbourhood intensity similarity replaces point-wise gray level similarity as seen in conventional bilateral filtering (Coupe P. , et al., 2008). This innovative NL recovery framework amalgamates two pivotal attributes of denoising algorithms: edge preservation and noise reduction.

The objective of this study encompasses two primary goals. Firstly, it aims to tailor and execute machine and deep learning-driven image quality transfer techniques, such as SynthSR (Iglesias , et al., 2021), on practical hyperfine MR T1w images. These empirical images are obtained within the scope of a comprehensive international collaboration study funded by the Bill and Melinda Gates Foundation (BGMF) (Artificial Intelligence Methods for Low Field MRI Enhancement - INV-032788). Secondly, the study seeks to adapt and apply data-driven denoising algorithms, including the non-local means algorithm, to the empirical hyperfine MR T1w images and to devise quality metrics that can quantitatively assess the extent of image enhancement achieved through these adapted methodologies.

## 4.2 Materials and Methods

### 4.2.1. Participants and Image Acquisition

#### 4.2.1.1. Empirical dataset

One of the main objectives of this study is the Low Field MRI (UNITY) Initiative, which aims to demonstrate proof-of-concept scalable imaging using a 64mT portable MRI scanner in LMIC (Lower- and Middle-income countries) settings. It also focuses on developing novel imaging methods and sequences to accurately measure neurodevelopmental signatures.

The Hyperfine Swoop ([www.hyperfine.io](http://www.hyperfine.io)) MRI system plays a crucial role in this initiative. It features a permanent main magnetic field of 64 mT, with a 5 Gauss boundary diameter of approximately 5 feet. Despite its low power requirements, the system weighs just over 1400 lbs (see Figure 1). The Swoop scanner was designed to increase access to MRI, and its motorized platform allows easy navigation through hospital corridors, elevators, and patient care areas. The compact system stands 59-inches tall and 33-inches wide, weighing 1,400 pounds. Imaging sequences include T1, T2, FLAIR, and DWI (with ADC map), all directed by a tablet interface. While the Hyperfine Swoop is currently capable of T1, T2, and T2-FLAIR weighted anatomical imaging, the analysis in this study has been restricted to T1-weighted data, as it provides the best image contrast and quality.

To demonstrate the potential of enhancing image quality with machine learning algorithms, MRI was performed using the 64 mT hyperfine lucy scanner, and data was collected from N=13 individuals (see Figure 4.2 A). This data collection process is part of an ongoing multi-centre collaboration project involving The Kings



College, London, Aga Khan University, Karachi, University of Cape Town, South Africa, and National Brain Research Centre, Manesar.

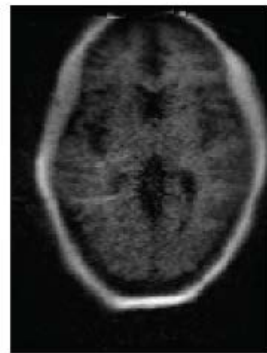


**Figure 4.1 Portable Hyperfine 64 mT MR scanner** Hyperfine Swoop, the world's first portable MR imaging system, is capable of providing neuroimaging at the point of care. Its capabilities enable timely diagnosis and treatment of acute conditions across various clinical settings.

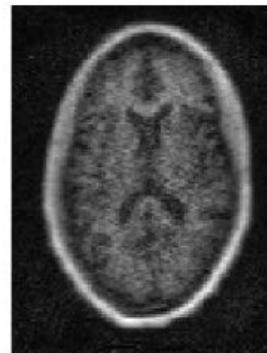
#### 4.2.1.2. Synthetic dataset

Brainweb is a synthetic 3-D MR image data simulator (Cocosco C. , Kollokian , Kwan, & Evans , 1997) which is often used as a gold standard for the analysis of the in-vivo MR data. Here, we generated two phantom T1-w images using SFLASH sequence (volume size = 217 X 181 X 181) and Gaussian noise was added to the phantom T1-w images at 3 % and at 9% (Figure 4.2 B).

## A. Empirical database



ADULT\_001\_15092020



ADULT\_010\_02082019

## B. Synthetic database



BRAINWEB 3% gaussian noise



BRAINWEB 9% gaussian noise

**Figure 4.2 T1 w MR images used in the study** (A) Original 3D MR image or “Ground Truth” of two representative participants from the empirical hyperfine dataset (B) Original 3D MR image or “Ground Truth” of two simulated T1w images from the BrainWeb database with added Gaussian noise at 3% and 9%.

### 4.2.2. Data Analysis

#### 4.2.2.1. Image Quality transfer using SynthSR

Various attempts have been made to bridge the gap between clinical and research scans in medical imaging, mainly using super-resolution (SR) and synthesis techniques inspired by computer vision. Early SR approaches relied on model-based methods with limitations in MRI's Fourier-encoded dimensions. Successful

SR of MRI has been achieved through machine learning (ML) techniques, including classical ML and later deep convolutional neural networks (CNNs). CNNs outperformed classical methods, with recent advancements like densely connected networks, adversarial networks, and progressive architectures further improving results, benefiting downstream analyses like cortical thickness and tractography. However, CNNs' adoption in clinical MRI analysis is hindered by the need for paired data or HR images during training, often unavailable due to varying MRI acquisition protocols across sites. To address this, probabilistic models have been proposed, but they underperformed compared to CNNs. To tackle this limitation, in this study we use "SynthSR," (Figure 4.3) which uses synthetically generated images to train a CNN for reconstructing isotropic scans of reference MRI contrasts from thick-slice scans with different resolutions and pulse sequences. This approach allows wide applicability without observing real HR scans. The effectiveness of SynthSR is validated by analysing various neuroimaging tools' performance on reconstructed isotropic scans, including segmentation, registration, and cortical thickness. The study emphasizes SynthSR's advantages over traditional SR approaches, which rely on image similarity metrics for validation, potentially inadequate predictors of downstream analysis performance. It concludes by discussing future possibilities and applications of SynthSR in medical imaging research. We adapt SynthSR directly from the GitHub repository (<https://github.com/BBillot/SynthSR>). The detailed methodology of SynthSR can be obtained at (Iglesias , et al., 2021).

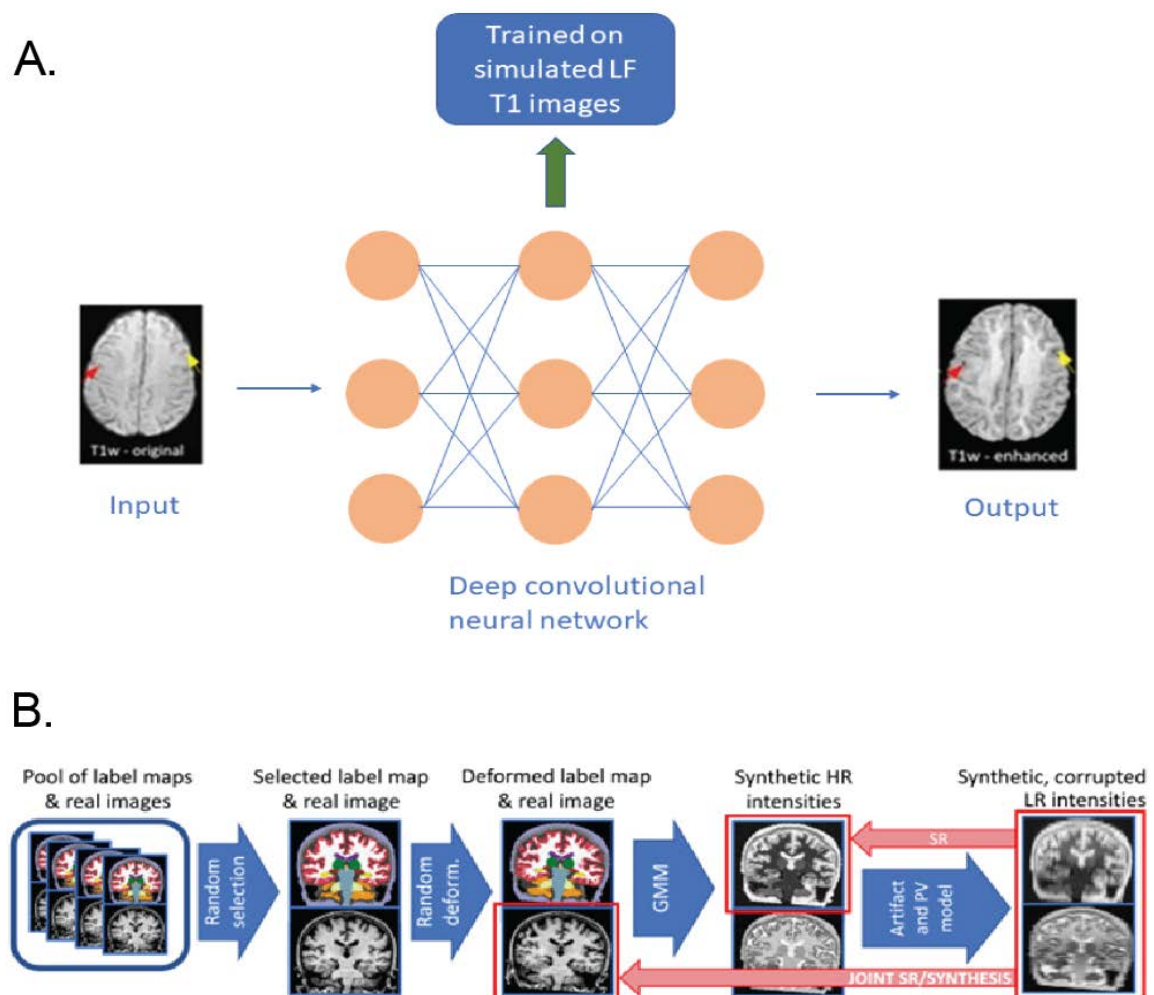


**Figure 4.3 Overview of SynthSR pipeline (adapted from (Iglesias, et al., 2021))**  
 (A) The utilization of deep convolutional neural networks, exemplified by the SynthSR framework, presents a robust approach for enhancing images. In this context, the input comprises low-field hyperfine T1-weighted (T1w) MR images. The essence of this approach lies in training the convolutional neural network (CNN) on simulated T1 images, capitalizing on advanced machine learning techniques to achieve image enhancement. (B) In this diagram, the blue arrows represent the generative model, facilitating the sampling of random scans at each minibatch with GPU implementation. On the other hand, the red arrows connect the inputs and regression targets used during training for either super-resolution (SR) or joint SR/synthesis. It is important to note that real images are only necessary for joint SR/synthesis, and not for SR alone.

A.

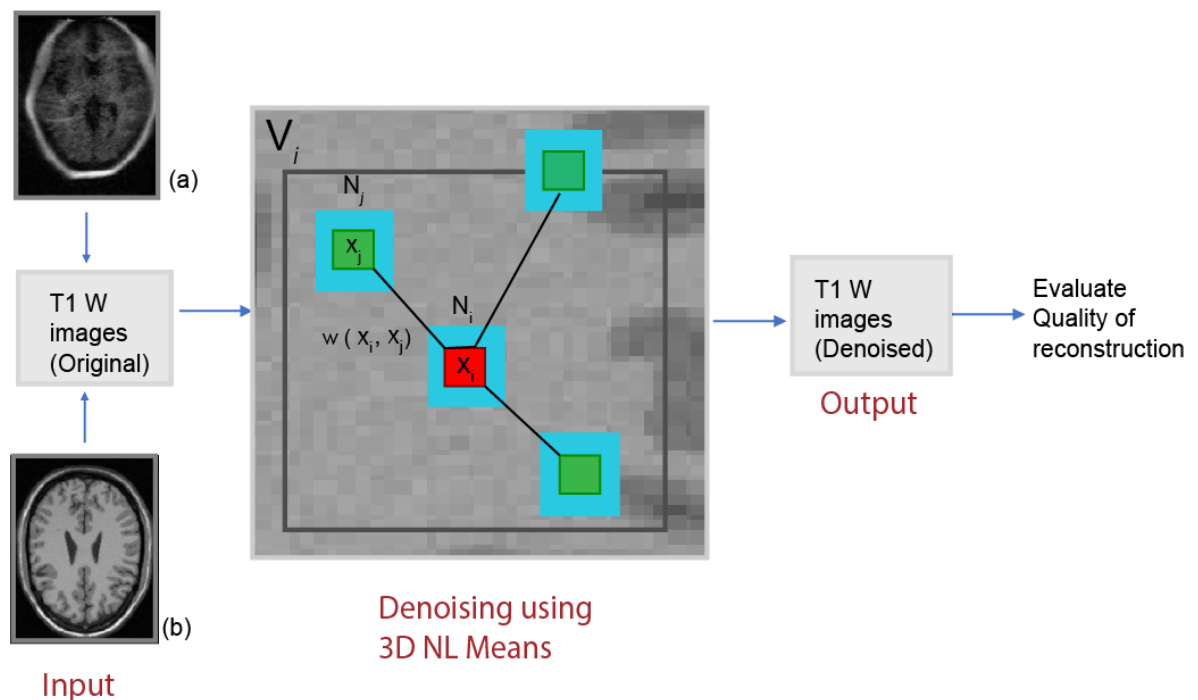


**Figure 4.4** Schematic diagram gives an overview of the NL means implementation. The input to the algorithm is either an empirical 3D MR image (a) or a phantom 3D MR image generated with BrainWeb database with two different noise levels (b). The denoising through NL means algorithm restores the value of voxel  $x_i$  (in red) with the weighted average of all intensities of  $x_j$  in the search volume  $V_i$ , based on the similarities of their intensity neighbourhoods,  $N_i$  and  $N_j$ . Output of the algorithm is a denoised 3D MR image.

#### 4.2.2.2. Denoising using NL means algorithm

Denoising is one of the crucial steps to increase the image quality by removing noise while keeping the integrity of the relevant image information. The basic intuitive, *data-independent* approach is to restore the intensity value of each image voxel by the average of voxels in its spatial neighbourhood (McDonnell, 1981). The major drawback of this approach is the blurring of edges/ structures of interest in the image. NL means algorithm, a *data-dependent* approach utilises the redundancy property (i.e., any voxel in the image is similar to other voxels that are

not necessarily located in its spatial neighbourhood) to remove noise from the image (Coupe P. , et al., 2008). In this denoising approach, the intensity similarity of the neighbourhood of a voxel with the neighbourhood of the voxel under study is used as a major criterion to eliminate/ reduce influence of dissimilar voxels to the voxel under study. Figure 4.4 shows the flow chart of the methodology used in the manuscript. We implement NL means using ANIMA software. The following are the notations used through the manuscript:

$u(x_i)$  : Intensity at voxel  $x_i$

$\Omega^3$  : Grid of the image

$M$ : Step size of the search volume  $V_i$  of the voxel  $x_i$

$d$ : Step size of the local neighbourhood  $N_i$

$V_i$  : Cubic search volume centred on voxel  $x_i$  of size  $|V_i| = (2M + 1)^3$ ,  $M \in \mathbf{N}$

$N_i$  : Cubic local neighbourhood of  $x_i$  of size  $|N_i| = (2d + 1)^3$ ,  $d \in \mathbf{N}$

$U(N_i)$ : Vector containing the intensities of  $N_i$

$NL(u)(x_i)$ : Restored value of  $x_i$

$w(x_i, x_j)$ : Weight of voxel  $x_j$  while restoring  $u(x_i)$

In the 3D NL-means filter, the restored intensity  $NL(u)(x_i)$  of the voxel  $x_i$  is the weighted average of all voxel intensities in the image  $u$  given by the following equation:

$$NL(u)(x_i) = \sum_{x_j \in \Omega^3} w(x_i, x_j)u(x_j) \quad (4.1)$$

where  $u(x_j)$  is the intensity of the voxel  $x_j$  and  $w(x_i, x_j) \in [0, 1]$  is the weight of voxel  $x_j$  while restoring  $x_i$ , which quantifies the similarity of neighbourhoods  $N_i$  and  $N_j$  of the voxels  $x_i$  and  $x_j$ .

The weight  $w(x_i, x_j)$  is computed as follows:

$$w(x_i, x_j) = \frac{1}{Z_i} e^{\frac{-\|u(N_i) - u(N_j)\|_{2,a}^2}{h^2}} \quad (4.2)$$

where  $Z_i$  is a normalization constant ensuring  $\sum_j w(x_i, x_j) = 1$ ,

$\|\cdot\|_{2,a}^2$  is a classical L2 norm for each voxel  $x_j$  in  $V_i$  which measures the distance between neighbourhood voxel intensities

$h$  acts as a smoothing parameter controlling the decay of the exponential function

#### 4.2.2.3. Automatic tuning of the smoothing parameter $h$

In optimised NL-means algorithm (Coupe P., et al., 2008) which allows for tuning of the smoothing parameter  $h$ , the weight  $w(x_i, x_j)$  is redefined as:

$$w(x_i, x_j) = \frac{1}{Z_i} e^{\frac{-\|u(N_i) - u(N_j)\|_{2,a}^2}{2\beta\sigma^2|N_i|}} \quad (4.3)$$

where only  $\beta$ , the adjusting constant needs to be manually tuned.

#### 4.2.2.4. Pre selection of voxels in the search volume

Most relevant voxels  $x_j$  in  $V_i$  that will have highest weight  $w(x_i, x_j)$  are preselected without having to compute distances between all of  $U(N_i)$  and  $U(N_j)$ . Selecting most relevant voxels a priori is shown to increase the processing speed of the NL-means algorithm (Coupe P., et al., 2008). The pre-selection of voxels is based on similarity of neighbourhood intensities. Intuitively similar neighbourhoods have the

same mean and same gradient information (Coupe P. , et al., 2008). Therefore, the ratio of average intensities of neighbourhood of pixels of  $x_i$  and  $x_j$  is considered when computing  $w(x_i, x_j)$ .  $\mu_1 < 1$  and  $\sigma^2 < 1$  are two limiting constants (Mahmoudi & Sapiro, 2005). The corresponding neighbourhood with non-zero value of  $w(x_i, x_j)$  would be 'pre-selected'. The selection test is as follows;

$$w(x_i, x_j) = \left\{ \frac{1}{z_i} e^{-\frac{\|u(N_i) - u(N_j)\|_{2,a}^2}{2\beta\sigma^2|N_i|}}, \text{ if } \mu_1 < \frac{\overline{U(N_i)}}{\overline{U(N_j)}} < \frac{1}{\mu_1} \right. \\ \left. \text{and, } (\sigma^2) < \frac{\text{Var}(U(N_i))}{\text{Var}(U(N_j))} < \frac{1}{(\sigma^2)} \right. \quad (4.4) \\ \left. 0, \quad \text{otherwise} \right\}$$

We vary both  $\beta$  (adjusting constant to tune smoothing parameter  $h$ ) and  $(\sigma^2)$  (limiting constant for variance of  $U(N_i)$  and  $U(N_j)$ ) to understand its influence on denoising and select an optimal value for these parameters based on quality measures. All other parameters are set to their default values.

#### 4.2.2.5. Quality measures

In assessing any new image acquisition or image reconstruction technique image quality assessment plays a vital role. We employ quality measures from two families – 1) Quality assessment measuring image compression quality (Lopez, Frederick, & Ventura, 2021) 2) Objective assessment computed with mathematical algorithms



#### 4.2.2.6. Quality assessment measuring image compression quality

##### 4.2.2.6.1. Peak SNR (PSNR)

*PSNR* is the ratio between a signal's maximum power and the power of the signal's noise. The peak signal-to-noise ratio (*PSNR*) between two images estimates the quality of reconstruction. Here, we estimate the *PSNR* between the "ground truth" (original image) and denoised MR image. In case of empirical data, the ground truth is the hyperfine T1 MR image, before denoising. *PSNR* is defined as follows:

$$PSNR = 10 \log_{10} \left( \frac{MAX^2}{MSE} \right) \quad (4.5)$$

where *MAX* is the maximum achievable value in the input image, *MSE* is the mean squared error

##### 4.2.2.6.2. Mean Squared Error

Mean Squared Error represents the cumulative squared error between ground truth and denoised MR image. *MSE* is defined as:

$$MSE = \frac{\sum_{M,N} [I_1(m,n) - I_2(m,n)]^2}{M*N} \quad (4.6)$$

where *M* and *N* are the number of rows and columns of the input image, *I*<sub>1</sub> and *I*<sub>2</sub> are the input images.

##### 4.2.2.6.3. Structural Similarity Index Measure (SSIM)

*SSIM* is an image quality metric that assesses three characteristics of an image: luminance, contrast and structure. The overall index is a multiplicative combination of three terms described as follows:

$$SSIM(x, y) = [l(x, y)]^\alpha * [c(x, y)]^\beta * [s(x, y)]^\gamma \quad (4.7)$$

$$l(x, y) = \frac{2\mu_x\mu_y + C_1}{\mu_x^2 + \mu_y^2 + C_1} \quad (4.8)$$

$$c(x, y) = \frac{2\sigma_x\sigma_y + C_2}{\sigma_x^2 + \sigma_y^2 + C_2} \quad (4.9)$$

$$s(x, y) = \frac{\sigma_{xy} + C_3}{\sigma_x\sigma_y + C_3} \quad (4.10)$$

where  $\mu_x$ ,  $\mu_y$ ,  $\sigma_x$ ,  $\sigma_y$  and  $\sigma_{xy}$  are the local means along  $x$  and  $y$  dimensions, standard deviations along  $x$  and  $y$  dimensions, and cross-covariance for images  $x$  and  $y$  respectively. The weights  $\alpha, \beta, \gamma$  are set to 1 in this manuscript.

#### 4.2.2.7. Objective assessment

Although there is no gold standard for assessing image quality, the objective assessment of medical images is divided into three categories: (1) Full reference (FR) where there is an ideal reference image for comparison with the test image (2) Reduced reference (RR), which consists of partial information of reference image and (3) No reference (NR), also known as blind assessment uses inherent image characteristics to compute image quality, forgoing the need for a reference image (Chow & Paramesran, 2016). No reference (NR) image quality assessment techniques are preferred for assessing medical images because there is no perfect reference image in the real-world medical imaging (Chow & Paramesran, 2016). Here, we use two No reference (NR) image quality assessment techniques as quality measures

##### 4.2.2.7.1. JPEG compression-based image quality analysis

We applied a no-reference image quality measure (developed by (Wang, Sheikh, & Bovik, 2002) adapted for structural MRI images by (Woodard & Carley-

Spencer, 2006) based on distortions caused by JPEG DCT based lossy compression. This method estimates image quality by assessing image blockiness and blurring artefacts created during quantization. The software provides three image quality measures, all of which are used in the current study: a measure for image blockiness, a measure for image blurring and an overall measure of image quality. For more details, please refer (Wang , Sheikh , & Bovik , 2002).

#### 4.2.2.7.2. Image Quality Evaluation (IQE)

Image Quality Evaluation (Osadebey , Pederson , Arnold , & Wendel-Mitoraj , 2018) is an objective, no-reference attribute-based quality evaluation for MRI images. The technique utilises the statistical properties that describe different levels of contrast degradation in MRI images. Each possible level of contrast-distorted MRI image slice is assigned a unique set of pixel configuration. The Quality prediction can be summarised in four steps: (1) extract local contrast feature image from the test image (2) compute mean and standard deviation of the feature image (3) Standardise the distribution using mean and standard deviation computed from the feature image (4) Predict the lightness contrast quality score and texture contrast quality score. Lightness contrast quality score is the magnitude of perceived visual differences of local structures within the MRI image. Texture contrast quality score is the magnitude of details that describe the local and anatomical structures within the MRI image in the presence of either blurring or noise degradation process.



## 4.3. Results

### 4.3.1. Image Quality Transfer (IQT) using SynthSR

In this section, we elaborate on the process and outcomes of enhancing the quality of hyperfine MR images using the SynthSR technique, which was directly adapted and implemented from the GitHub repository. Initially, we conducted training sessions of SynthSR using synthetic data, followed by its application to enhance real hyperfine MR images acquired from a 64mT coil, serving as our testing dataset. To evaluate the capability of the SynthSR method in terms of super-resolution (SR) performance, we initiated a controlled experiment. For this, we utilized synthetically down sampled MP-RAGE scans obtained from a 3T GE scanner, provided by Kings College London through Dr. Rosalyn Moran's research group. The objective of this initial phase was to assess the method's ability to enhance a single volume while considering variations in slice spacing. Subsequent to the initial training phase, we proceeded to test the CNN model of SynthSR using the designated testing dataset, consisting of real hyperfine T1w images (as illustrated in Figure 4.5). Through visual inspection, we were able to observe the noticeable improvement in image quality achieved through the Image Quality Transfer (IQT) process applied by SynthSR. This enhancement became evident in the hyperfine T1w images, thus underscoring the effectiveness of the SynthSR approach in enhancing the quality of the acquired hyperfine MR images.

### 4.3.2. Denoising using NL means algorithm

#### 4.3.2.1. Estimating optimal values for $\beta$ and $(\sigma^2)$

First, in order to select optimal values for  $\beta$  (adjusting constant to tune smoothing parameter  $h$ ) and  $\sigma^2$  (limiting constant for variance of  $U(N_i)$  and  $U(N_j)$ ) we run the NL means algorithm on a single subject and estimate *PSNR*, *MSE* and *SSIM*.

Figure 4.6 A shows the influence of  $\beta$  and  $\sigma^2$  on quality measures. Optimal values for  $\beta$  and  $\sigma^2$  are selected as the ones with highest *PSNR*, *SSIM* and lowest *MSE*. The results indicate the best value of  $\beta$  is close to 0.2 and  $\sigma^2$  is close to 0.5. With  $\beta=0.2$  and  $\sigma^2 = 0.5$ , we implement NL means algorithm on empirical dataset and validate the same on synthetic dataset.

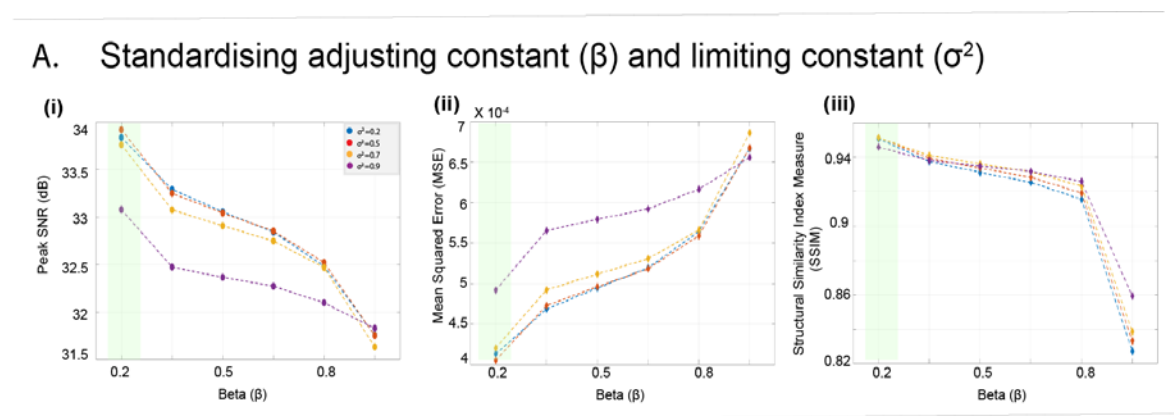


**Figure 4.6 Calibration of NL means algorithm and Image quality metrics (A)** Calibration of  $\beta$  (adjusting constant to tune smoothing parameter  $h$ ) and  $\sigma^2$  (limiting constant for variance of  $u(N_i)$  and  $u(N_j)$ ). We check the influence of  $\beta$  for and  $\sigma^2$  on *PSNR*, *MSE* and *SSIM*. *PSNR* is high for low values of  $\beta$  and  $\sigma^2$ , peaking at  $\beta = 0.2$  and  $\sigma^2 = 0.5$

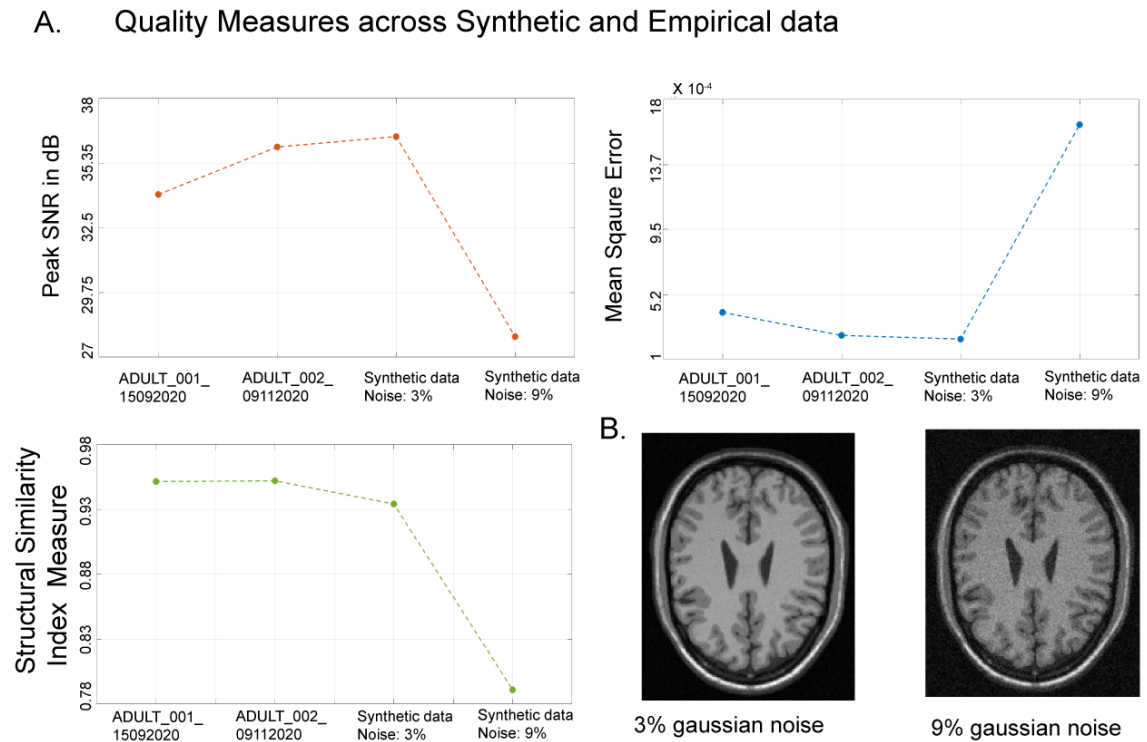


**Figure 4.7 Quantifying the performance of NL means algorithm** (A) Quantifying the performance of NL means across empirical and synthetic dataset. We estimate PSNR, MSE and SSIM for all the available participants of empirical dataset after denoising with NL means and validate the same with synthetic dataset. For the empirical dataset, we report the results of two participants with highest PSNR. We run NL means algorithm with  $\beta = 0.2$  and  $\sigma^2 = 0.5$ . These results suggest good performance of NL means algorithm on the empirical/synthetic dataset. (B) Original 3D MR image or “Ground Truth” of two simulated T1w images from the BrainWeb database with added Gaussian noise at 3% and 9%.

## A. Ground Truth

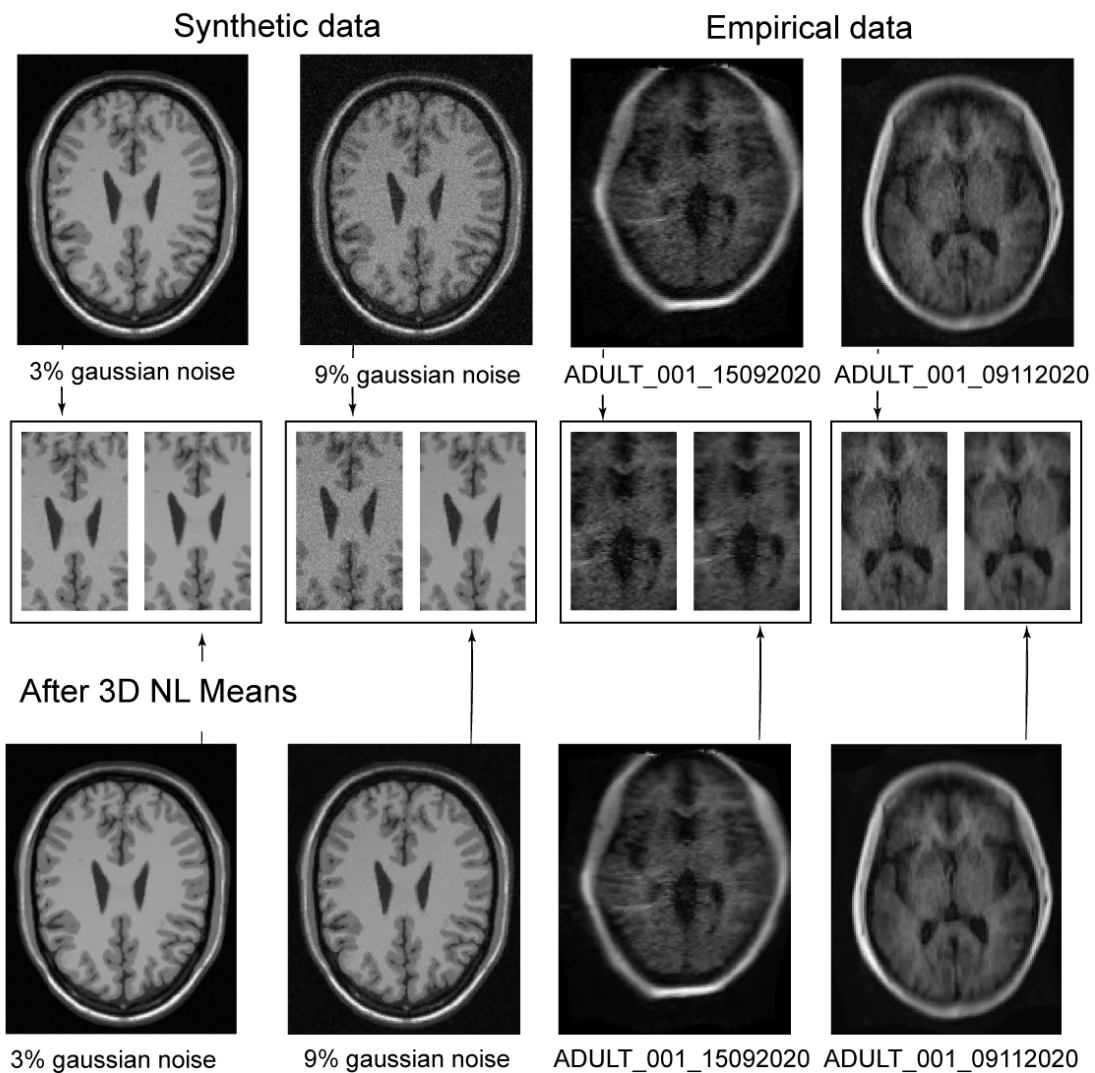


**Figure 4.8 Before and after NL means.** Comparison between Ground truth and denoised images after applying NL means algorithm on T1w images: Synthetic data with 3% and 9% added Gaussian noise and Empirical data.

**Top:** Original Ground Truth T1-w images - Synthetic and empirical

**Middle:** Detailed zoomed-in images contrasting ground truth and denoised T1-w images of synthetic and empirical data. Denoising is achieved with NL means algorithm with adjusting constant of smoothing parameter ( $\beta$ ) = 0.2. Adjusting parameter controls the strength of denoising.

**Bottom:** Original denoised T1-w images obtained after applying NL means algorithm on synthetic and empirical MR images.



#### 4.3.2.2. Image Quality Analysis

##### 4.3.2.2.1. Using image compression quality measures

Although we have applied the NL Means algorithm on all the available participants in the empirical dataset, we present the data of two participants with highest *PSNR*, *SSIM* and lowest *MSE* (Figure 4.7). The performance of NL means algorithm is quantified with quality measures as shown in Figure 4.7A. For both the participants, in the empirical dataset, the algorithm achieved a *PSNR* > 33 dB indicating a good denoising. The *MSE* and *SSIM* for the empirical images were also in the magnitude of  $MSE < 5.2 \times 10^{-4}$  and *SSIM* > 0.95. For the synthetic BrainWeb dataset, two T1w images with different levels of gaussian noise (one at 3% and other at 9%) were simulated in order to do a quantitative comparison with the empirical dataset (Figure 4.7 B). For the synthetic 3D MR images, as expected, the performance of the algorithm deteriorated with increase in noise – *PSNR* for T1w images at 3% noise is 37 dB whereas for T1w images at 9% noise is 28 dB (Figure 4.7A). The original image or the “Ground truth” of empirical /synthetic images and denoised MR images after NL means are shown in Figure 4.8.

## Image quality analysis metrics

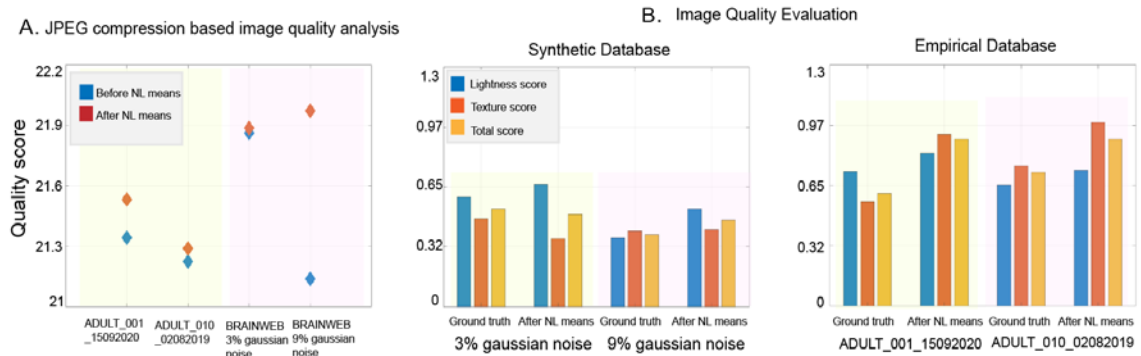


**Figure 4.9 Image quality analysis metrics.** Quantifying the performance of NL means across empirical and synthetic dataset using two metrics - JPEG compression-based image quality analysis (A) and Image quality evaluation (B).

#### 4.3.2.2.2. Using objective assessment measures

Using JPEG compression-based image quality analysis technique as a quality metric

First, we quantify the performance of the NL means algorithm on synthetic and empirical hyperfine MR images with JPEG compression-based quality measures as shown in Figure 4.9A. The overall image quality score increased for MR images after denoising with NL means algorithm – in both synthetic and empirical MR images.

Using Image Quality Evaluation (IQE) technique as a quality metric

Next, we applied Image Quality Evaluation (IQE) technique and calculated lightness contrast score, texture contrast score and an overall image quality score to quantify the performance of the NL means algorithm, on both synthetic and empirical MR images. In the synthetic MR images, lightness contrast score increased with denoising whereas texture contrast score decreased marginally but overall image quality score increased after denoising. In empirical hyperfine MR

images, lightness contrast score, texture contrast score and overall image quality score increased after denoising with the NL means algorithm, indicating a reasonable performance of NL means algorithm in denoising and removing noisy artefacts from the MR images (see Figure 4.9B). Figure 4.10 presents a visual comparison of T1w images for all subjects before and after the application of the NL means algorithm.

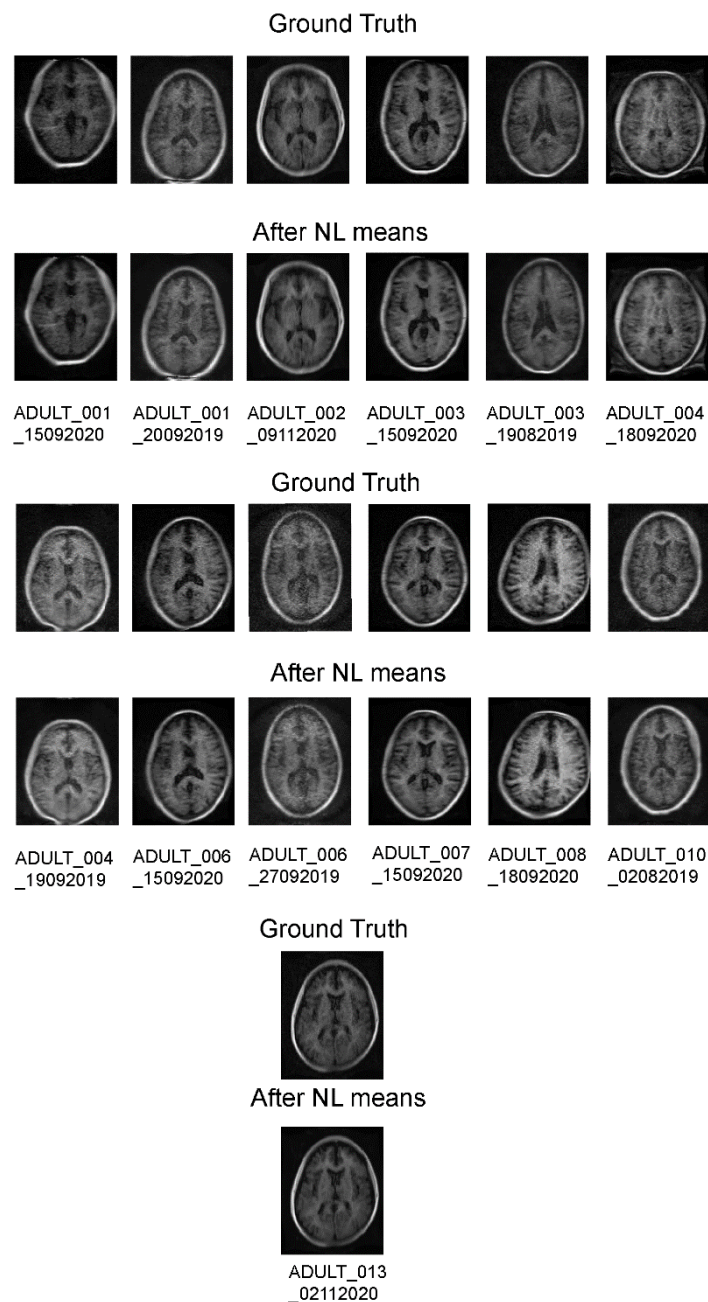


**Figure 4.10 Before and after NL means.** Visual comparison of T1w images for all subjects before and after the application of the NL means algorithm.

#### 4.4. Discussion

The scope of this study is embedded within a broader international multicentre collaborative effort known as the 'Artificial Intelligence Methods for Low Field MRI Enhancement' project, which has received funding from the Bill and Melinda Gates Foundation (BMGF). This initiative is aligned with the Low Field MRI and neurodevelopment initiatives and is aimed at exploring the application of artificial intelligence (AI) techniques to optimize the information content and data quality acquired through low field MRI systems, particularly the Hyperfine Swoop. In this context, the study delves into the utilization of AI-driven methods, specifically image quality transfer (Iglesias , et al., 2021), to enhance the content and quality of data generated by low field MRI systems. The overarching goal of this low field initiative involves both the translation of established techniques and the development of innovative imaging methods for deployment on low field MRI systems. This initiative acknowledges the potential of low field MRI technology and aims to unlock its capabilities through advanced AI approaches. The current study aligns with these objectives and embarks on two primary missions. The first objective entails adapting and implementing machine and deep learning-based image quality transfer techniques, exemplified by methods like SynthSR (Iglesias , et al., 2021) , onto practical hyperfine MR T1w images. As part of first objective, we adapt and implement deep convolutional neural network models such as SynthSR (<https://github.com/BBillot/SynthSR>) to enhance the image quality of low-field T1 w MR tuples. SynthSR stands out as a pioneering learning technique capable of producing isotropic volumes of reference MR contrast. It achieves this feat using a series of scans from a routine clinical MRI exam, even if the original scans are anisotropic 2D acquisitions. The distinctiveness of SynthSR lies in its ability to

operate without access to high-resolution training data for the input modalities (see Figure 4.3). The fundamental methodology of SynthSR involves leveraging random synthetic data that closely mimic the resolution and contrast characteristics of the target scans targeted for super-resolution. This synthetic data is systematically generated in real-time on a GPU, employing an approach inspired by the generative model of Bayesian segmentation. This simulation framework not only encompasses contrast and resolution but also encompasses variations in orientation, subject motion between scans, as well as factors such as bias field and registration errors (Iglesias, et al., 2021). These synthesized artifacts and extracerebral tissues are integrated into the simulations. As a consequence, SynthSR technique circumvents the need for extensive preprocessing steps such as skull stripping, denoising, or bias field correction. The only prerequisite is the rigid coregistration of input scans. SynthSR ability to handle diverse artifacts and simulate realistic imaging conditions adds to its versatility, rendering it an efficient and powerful tool for enhancing the quality and resolution of MRI scans (see Figure 4.5). Subsequently, our investigation delved into the realm of data-driven denoising techniques, specifically focusing on the integration of the non-local means algorithm to enhance the image quality of empirical hyperfine MR T1w images (Figure 4.4) (Coupe P., et al., 2007) (Baudes, Coll, & More, 2005). In this phase, our approach involved the adaptation and implementation of a 3D non-local means denoising algorithm onto practical hyperfine T1w images. This strategic incorporation aimed to address inherent noise and artifacts in the acquired images, optimizing their overall visual clarity and interpretability (Figure 4.8 and Figure 4.10). To systematically gauge the efficacy of these enhancements, we went on to develop a set of comprehensive image quality measures (Image compression

quality measures and objective assessment measures) (Osadebey , Pederson , Arnold , & Wendel-Mitoraj , 2018) (Figure 4.9). These metrics were meticulously designed to quantify the extent of image enhancement achieved through our adapted denoising methodologies. By employing these quantitative measures, we were able to objectively evaluate and compare the improvements achieved across various image datasets, providing a standardized means to gauge the effectiveness of our denoising strategies (Figure 4.9).

In essence, our study undertook a two-fold approach, first utilizing machine and deep learning techniques to enhance the resolution of hyperfine MR T1w images through image quality transfer methods like SynthSR. Subsequently, we harnessed the power of data-driven denoising algorithms, specifically the non-local means algorithm, to further elevate the image quality by reducing noise and refining visual clarity. Through these twin methodologies and the development of tailored image quality metrics, our study sought to comprehensively optimize the overall quality and interpretability of empirical hyperfine MR T1w images.

# Chapter 5

## Conclusion

Artificial Intelligence (AI), exemplified by advancements like ChatGPT and DALL-E, represents a transformative force permeating various aspects of life. One prominent domain for AI's application is healthcare, especially in diagnostics. This thesis delves into the applications of AI in the human brain, encompassing both its structural and functional connectome. The effectiveness of AI's predictions heavily relies on robust input features, particularly when dealing with intricate systems like the brain. In this context, it becomes crucial for these features to be firmly grounded in well-established biological evidence. When rooted in biological evidence, these features enable the model's predictions to closely align with observed outcomes within the biological systems it aims to replicate. Notably, in functional connectomics, brain connectivity patterns offer a promising avenue for identifying input features guided by biological evidence. Developing a data-driven methodology for studying brain connectivity patterns, free from data biases, holds paramount importance. Dynamic functional connectivity (dFC), despite its inherent limitations (Prete, Bolton, & Van De Ville, 2017) captures meaningful information in temporal fluctuations on the scale of minutes (Hutchison & et al, 2013). Understanding the key contributors to the stability of FC patterns in ongoing brain dynamics is crucial for survival and remains an unresolved vital issue (Li, Lu, & Yan, 2019). In the realm of structural connectomics, the utilization of machine learning and deep learning models to enhance the image quality of low-field MRI scans carries significant importance, especially for lower and middle-income

countries. These advancements have the potential to substantially improve image quality, thereby positively impacting medical diagnostics and research within these regions.

In Part I of this thesis, we concentrate on developing data-driven, unsupervised methodologies and stochastic measures to estimate the temporal stability of functional connectomics. These methods are applied to large-scale resting-state lifespan aging and common mental disorder datasets. In Part II of the thesis, the focus shifts to utilizing deep learning and machine learning models for enhancing T1-weighted structural images. In the three studies detailed in Chapters 2, 3, and 4, we arrive at the following significant conclusions:

1. In study 1, we introduce a novel data-driven, unsupervised method aimed at characterizing the temporal stability of functional brain architecture. When we applied this method to a dataset representing lifespan aging ( $N > 600$  participants), we made several noteworthy observations. Firstly, during a naturalistic movie-watching task, the temporal dynamics of the entire brain were more similar to those observed during resting states than during sensorimotor tasks. Secondly, our study revealed that the sensorimotor task exhibited the highest peak temporal stability, followed by naturalistic movie watching and resting states. This pattern held true across different age groups, including young, middle-aged, and elderly individuals. Most importantly, we found that the temporal stability of the functional brain architecture during resting states was primarily influenced by the stability of the sensorimotor network across the entire lifespan. This discovery underscores the potential of using temporal stability measures as valuable



biomarkers for a range of neurological disorders, given their ability to quantify differences in network stability associated with healthy aging.

2. In study 2, we apply and improve upon our novel methodology introduced in study 1 and propose an unsupervised approach that combines spatial and temporal characterization of brain networks to classify common mental disorders from fMRI timeseries, utilizing two cohorts (N=408 participants). This study highlights the significance of dynamic functional connectivity (dFC) and temporal stability in characterizing common mental disorders. While the community architecture of functionally connected brain networks, assessed using the weighted stochastic block model (WSBM), shows discernible patterns between individuals with mental disorders and healthy controls, nonetheless WSBM faced challenges in clearly distinguishing between different disorders. The measurements of assortativity, coreness, and motif participation index provide valuable insights into community interactions but did not result in distinct separation between disorders. However, temporal stability analysis, through angular distance, global temporal distance and entropy calculations, uncovers impaired stability in schizophrenia and ADHD, while bipolar disorder shows notable differences. These findings underscore the crucial role of dFC and temporal stability in understanding and characterizing common mental disorders, offering potential insights into their underlying mechanisms and potential diagnostic markers.
3. In study 3, our analysis pursued a dual approach. Firstly, we employed machine and deep learning techniques to enhance the resolution of hyperfine MR T1-weighted images using image quality transfer methods like

SynthSR. Following that, we harnessed data-driven denoising algorithms, particularly the non-local means algorithm, to further improve image quality by reducing noise and enhancing visual clarity. Through the combination of these two methodologies and the creation of customized image quality metrics, our study aimed to comprehensively optimize the overall quality and interpretability of empirical hyperfine MR T1-weighted images.

## **Future directions**

A meaningful extension of the present thesis could involve exploring the potential of using temporal stability as a feature in the classification of common mental health disorders by developing unsupervised classification algorithms. This would delve into the application of temporal stability measures to enhance our understanding of these disorders and potentially improve diagnostic capabilities. Another promising avenue for extension would be to investigate whether temporal stability could serve as a predictive marker. For instance, can temporal stability be used as a predictive marker for epilepsy seizures? This research could involve leveraging brain connectivity patterns to identify key distinctions between seizure and non-seizure activity, potentially leading to advancements in seizure prediction and management. Furthermore, a methodological extension could involve adapting the method used for estimating temporal stability, which is primarily based on fMRI datasets, to other imaging modalities such as EEG, MEG, and simultaneous EEG-fMRI. This expansion of the methodology could enable a broader and more comprehensive exploration of temporal stability in neural activity across various imaging techniques, providing valuable insights into brain dynamics.

# References

- Björck, A., & Golub, G. H. (1973). Numerical methods for computing angles between linear subspaces. *Mathematics of Computation*, 27, 579-594. doi:<https://doi.org/10.1090/S0025-5718-1973-0348991-3>
- Aertsen, A., Gerstein, G., Habib, M., & Palm, G. (1989). Dynamics of neuronal firing correlation: modulation of "effective connectivity". *Journal of Neurophysiology*, 61(5), 900-917. doi:<https://doi.org/10.1152/jn.1989.61.5.900>
- Aicher, C., Jacobs, A., & Clauset, A. (2015). Learning latent block structure in weighted networks. *Journal of Complex Networks*, 3(2), 221-248. doi:<https://doi.org/10.1093/comnet/cnu026>
- Alexander-Bloch, A., Lambiotte, R., Roberts, B., Giedd, J., Gogtay, N., & Bullmore, E. (2012). The discovery of population differences in network community structure: New methods and applications to brain functional networks in schizophrenia. *Neuroimage*, 59(4), 3889-3900. doi:<https://doi.org/10.1016/j.neuroimage.2011.11.035>
- Alexander-Bloch, A., Gogtay, N., Meunier, D., Birn, R., Clasen, L., Lalonde, F., . . . Bullmore, E. (2010). Disrupted modularity and local connectivity of brain functional networks in childhood onset schizophrenia. *Frontiers in systems neuroscience*, 4. doi:<https://doi.org/10.3389/fnsys.2010.00147>
- Alize J Ferrari, D. F. (2022). Global, regional, and national burden of 12 mental disorders in 204 countries and territories, 1990–2019: a systematic analysis for the Global Burden of Disease Study 2019. *The Lancet Psychiatry*, 9, 137-150. doi:[https://doi.org/10.1016/S2215-0366\(21\)00395-3](https://doi.org/10.1016/S2215-0366(21)00395-3)
- Allen, E., Damaraju, E., Plis, S., Erhardt, E., Eichele, T., & Calhoun, V. (2014). Tracking whole-brain connectivity dynamics in the resting state. *Cerebral Cortex*, 24(3), 663-676. doi:<https://doi.org/10.1093/cercor/bhs352>
- Allen, E., Damaraju, E., Plis, S., Erhardt, E., Eichele, T., & Calhoun, V. (2014). Tracking whole-brain connectivity dynamics in the resting state. *Cerebral Cortex*, 24(3), 663–676. doi:<https://doi.org/10.1093/cercor/bhs352>
- Amini, M., Pedram, M., Moradi, A., Jamshidi, M., & Ouchani, M. (2021). Single and Combined Neuroimaging Techniques for Alzheimer's Disease Detection. *Computational intelligence and Neuroscience*, 2021, 9523039. doi:<https://doi.org/10.1155/2021/9523039>

- Andersson, J. L., Hutton, C., Ashburner, J., Turner, R., & Friston, K. (2001). Modeling Geometric Deformations in EPI time series. *NeuroImage*, 13(5), 909-919. doi:<https://doi.org/10.1006/nimg.2001.0746>
- Arbablyazd, L., Lombardo, D., Blin, O., Didic, M., Battaglia, D., & Jirsa, V. (2020). Dynamic functional connectivity as a complex random walk: Definitions and the dFCwalk toolbox. *MethodsX*, 7, 101168. doi:<https://doi.org/10.1016/j.mex.2020.101168>
- Banerjee, A., Pillai, A. S., Sperling, J. R., Smith, J. F., & Horwitz, B. (2012). Temporal microstructure of cortical networks (TMCN) underlying task-related differences. *NeuroImage*, 62(3), 1643-1657. doi:<https://doi.org/10.1016/j.neuroimage.2012.06.014>
- Banerjee, A., Pillai, A., Sperling, J., Smith, J., & Horwitz, B. (2012). Temporal microstructure of cortical networks (TMCN) underlying task-related differences. *NeuroImage*, 62(3), 1643-1657. doi:<https://doi.org/10.1016/j.neuroimage.2012.06.014>
- Bassett, D., Wymbs, N., Porter, M., Mucha, P., Carlson, J., & Grafton, S. (2011). Dynamic reconfiguration of human brain networks during learning. *PNAS*, 108(18), 7641-7646. doi:<https://doi.org/10.1073/pnas.1018985108>
- Bassett, D., Zurn, P., & Gold, J. (2018). On the nature and use of models in network neuroscience. *Nature reviews neuroscience*, 19, 566-578. doi:<https://doi.org/10.1038/s41583-018-0038-8>
- Baudes, A., Coll, B., & More, J.-M. (2005). A review of image denoising algorithms, with a new one. *Multiscale modeling & simulation*, 4(2), 490-530.
- Bellec, P. (2016). Cobre preprocessed with niak 0.17-lightweight release.figshare. Available online at:[10.6084/m9.figshare.4197885.v1](https://doi.org/10.6084/m9.figshare.4197885.v1).
- Betzel, R., Medgalia, J., & Bassett, D. (2018). Diversity of meso-scale architecture in human and non-human connectomes. *Nature communications*, 9, 346. doi:<https://doi.org/10.1038/s41467-017-02681-z>
- Betzel, R., Bertolero, M., & Bassett, D. (2018). Non-assortative community structure in resting and task evoked functional brain networks. *Biorxiv*. doi:<https://doi.org/10.1101/355016>
- Betzel, R., Byrge, L., He, Y., Goñi, J., Zuo, X.-N., & Sporns, O. (2014). Changes in structural and functional connectivity among resting-state networks across the human lifespan. *NeuroImage*, 102(2), 345-357. doi:<https://doi.org/10.1016/j.neuroimage.2014.07.067>
- Billiot, B., Robinson, E., Dalca, A., & Iglesias, J. (2020). Partial Volume Segmentation of Brain MRI Scans of any Resolution and Contrast. *Medical Image Computing and Computer Assisted Intervention—MICCAI 2020: 23rd International Conference, Lima, Peru, Proceedings, Part VII*, 23.

- Biswal, B., Yetkin, F., Haughton, V., & Hyde, J. (1995). Functional connectivity in the motor cortex of resting human brain using echo-planar MRI. *Magnetic Resonance in Imaging*, *34*(4), 537-541. doi:<https://doi.org/10.1002/mrm.1910340409>
- Bjorck, A., & Golub, G. (1973). Numerical methods for computing angles between linear subspaces. *Mathematics and Computation*, *27*, 579-594.
- Black, M., & Sapiro, G. (1999). Edges as outliers: Anisotropic smoothing using local image statistics. *International Conference on Scale-Space Theories in Computer Vision. Berlin, Heidelberg*, 259-270.
- Bolton, T., Morgenroth, E., Preti, M., & Van De Ville, D. (2020). Tapping into Multi-Faceted Human Behavior and Psychopathology Using fMRI Brain Dynamics. *Trends in Neurosciences*, *43*(9), 667-680. doi:<https://doi.org/10.1016/j.tins.2020.06.005>
- Bordier, C., Nicolini, C., Forcellini, G., & Bifone, A. (2018). Disrupted modular organization of primary sensory brain areas in schizophrenia. *Neuroimage: Clinical*, *18*, 682-693. doi:<https://doi.org/10.1016/j.nicl.2018.02.035>
- Bullmore, E., & Sporns, O. (2009). Complex brain networks: Graph theoretical analysis of structural and functional systems. *Nature Reviews Neuroscience*, *10*, 186–198. doi:<https://doi.org/10.1038/nrn2575>
- Cabral, J., Viduarre, D., Marques, P., Magalhaes, R., Moreira, P., Soares, J. M., . . . Kringelbach, M. (2017). Cognitive performance in healthy older adults relates to spontaneous switching between states of functional connectivity during rest. *Scientific reports*, *7*, 5135. doi:<https://doi.org/10.1038/s41598-017-05425-7>
- Cabral, J., Viduarre, D., Marques, P., Magalhaes, R., Moreira, P., Soares, J., . . . Kringelbach, M. (2017). Cognitive performance in healthy older adults relates to spontaneous switching between states of functional connectivity during rest. *Scientific Reports*, *5135*. doi:<https://doi.org/10.1038/s41598-017-05425-7>
- Calhoun, V., Sui, J., Kiehl, K., Turner, J., Allen, E., & Pearlson, G. (2012). Exploring the psychosis functional connectome: aberrant intrinsic networks in schizophrenia and bipolar disorder. *Frontiers in Psychiatry*, *2*, 75. doi:<https://doi.org/10.3389/fpsy.2011.00075>
- Calhoun, V., Wager, T., Krishnan, A., Rosch, K., Seymour, K., Nebel, M. B., . . . Kiehl, K. (2017). The impact of T1 versus EPI spatial normalization templates for fMRI data analyses. *Human Brain Mapping*, *38*(11), 5331-5342. doi:<https://doi.org/10.1002/hbm.23737>
- Cao, M., Wang, J.-H., Dai, Z.-J., Cao, X.-Y., Jiang, L.-L., Fan, F.-M., . . . He, Y. (2014). Topological organization of the human brain functional connectome across the lifespan. *Developmental Cognitive Neuroscience*, *7*, 76-93. doi:<http://dx.doi.org/10.1016/j.dcn.2013.11.004>

- Castanon, N. (2020). FMRI denoising procedure. *Handbook of functional connectivity magnetic resonance imaging methods in CONN*, 17-25.
- Castellanos , F., Margulies , D., Kelly , C., Uddin , L., Ghaffari , M., Kirsch , A., . . . Milham , M. (2008). Cingulate-Precuneus interactions: A new locus of dysfunction in adult attention deficit/hyper activity disorder. *Biological Psychiatry*, 63(3), 332-337.  
doi:<https://doi.org/10.1016/j.biopsych.2007.06.025>
- Chang, C., & Glover, G. (2010). Time-frequency dynamics of resting-state brain connectivity measured with fMRI. *NeuroImage*, 50(1), 81-98.  
doi:<https://doi.org/10.1016/j.neuroimage.2009.12.011>
- Chen, K., Li, C., Sun, W., Tao, Y., Wang, R., Hou, W., & Liu, D.-Q. (2021). Hidden Markov Modeling Reveals Prolonged “Baseline” State and Shortened Antagonistic State across the Adult Lifespan. *Cerebral Cortex*.  
doi: <https://doi.org/10.1093/cercor/bhab220>
- Chen, Y., Wang, W., Zhao, X., Sha, M., Liu, Y., Zhang, X., . . . Ming, D. (2017). Age-related decline in variation of dynamic functional connectivity: A resting state analysis. *Frontiers in Aging Neuroscience*, 9:203.  
doi:<https://doi.org/10.3389/fnagi.2017.00203>
- Chengyuan , W., Ferreira , F., Fox , M., Harel , N., Hattangadi-Gluth, J., Horn , A., . . . Akram , H. (2021). Clinical applications of magnetic resonance imaging based functional and structural connectivity. *Neuroimage*, 244, 118649. doi:<https://doi.org/10.1016/j.neuroimage.2021.118649>
- Chow , L., & Paramesran, R. (2016). Review of medical image quality assessment. *Biomedical signal processing and control*, 27, 145-154.  
doi:<https://doi.org/10.1016/j.bspc.2016.02.006>
- Cocosco , C., Kollokian , V., Kwan, R., & Evans , A. (1997). BrainWeb: Online Interface to a 3D MRI Simulated Brain Database. *Neuroimage*, 5(4).
- Cocosco, C., Kollokian, V., Kwan, R., & Evans , A. (1997). Brainweb: Online interface to a 3D MRI Simulated Brain Database. *NeuroImage*, 5, 425.
- Cohen , J. (2018). The behavioral and cognitive relevance of time-varying, dynamic changes in functional connectivity. *Neuroimage*, 180 (Part B), 515-525. doi:<https://doi.org/10.1016/j.neuroimage.2017.09.036>
- Cooley , C., McDaniel, P., Stockmann, J., Srinivas , S., Cauley , S., Sliwiak , M., . . . Wald , L. (2021). A portable scanner for magnetic resonance imaging of the brain. *Nature Biomedical Engineering*, 5(3), 229-239.  
doi:<https://doi.org/10.1038/s41551-020-00641-5>
- Coupe , P., Yger , P., Prima , S., Hellier , P., Kevrann , P., & Barillot , C. (2007). An Optimized Blockwise Nonlocal Means Denoising Filter for 3-D Magnetic Resonance Images. *IEEE transactions on medical imaging*, 27(4), 425-441. doi:<https://doi.org/10.1109/tmi.2007.906087>

- Coupe, P., Yger, P., Prima, S., Hellier, P., Kervrann, C., & Barillot, C. (2008). An optimized blockwise nonlocal means denoising filter for 3D magnetic resonance images. *IEEE transactions on medical imaging*, 27(4). doi:10.1109/TMI.2007.906087
- Damaraju, E., Allen, E., Belger, A., Ford, J., McEwen, S., Mathalon, D., . . . Calhoun, V. (2014). Dynamic functional connectivity analysis reveals transient states of dysconnectivity in schizophrenia. *NeuroImage*, 5, 298-308. doi:https://doi.org/10.1016/j.neuroimage.2014.07.003
- Damoiseaux, J., Beckmann, C., Arigita, S., Barkhof, F., Scheltens, P., Stam, C., . . . Rombouts, S. (2008). Reduced resting state brain activity in the default network in normal aging. *Cerebral Cortex*, 18(8), 1856-1264. doi:https://doi.org/10.1093/cercor/bhm207
- Davis, S., Dennis, N., Buchler, N., White, L., Madden, D., & Cabeza, R. (2009). Assessing the effects of age on long white matter tracts using diffusion tensor tractography. *NeuroImage*, 46(2), 530-541. doi:https://doi.org/10.1016/j.neuroimage.2009.01.068
- Deco, G., Jirsa, V., & McIntosh, A. (2010). Emerging concepts for the dynamical organization of resting state activity in the brain. *Nature reviews neuroscience*, 12, 43-56. doi:https://doi.org/10.1038/nrn2961
- Deco, G., & Jirsa, V. (2012). Ongoing cortical activity at rest: Criticality, Multistability, and Ghost Attractors. *Journal of Neuroscience*, 32(10), 3366-3375. doi:https://doi.org/10.1523/JNEUROSCI.2523-11.2012
- Deco, G., & Kringelbach, M. (2016). Metastability and Coherence: Extending the communication through coherence hypothesis using a whole brain computational perspective. *Trends in Neurosciences*, 39(3), 125-135. doi:https://doi.org/10.1016/j.tins.2016.01.001
- Deco, G., & Kringelbach, M. (2016). Metastability and Coherence: Extending the communication through coherence hypothesis using a whole-brain computational perspective. *Trends in Neuroscience*, 39(3), 125-135. doi:https://doi.org/10.1016/j.tins.2016.01.001
- Deco, G., Jirsa, V., & McIntosh, A. (2011). Emerging concepts for the dynamical organization of resting-state activity in the brain. *nature reviews neuroscience*, 12, 43–56. doi:https://doi.org/10.1038/nrn2961
- Demirtas, M., Tornador, C., Falcón, C., López-Solà, M., Hernández-Ribas, R., Pujol, J., . . . Deco, G. (2016). Dynamic functional connectivity reveals altered variability in functional connectivity among patients with major depressive disorder. *Human Brain Mapping*, 37(8), 2918-2930. doi:https://doi.org/10.1002/hbm.23215
- Diamond, J. (1997). *Guns, Germs and Steel*. W. W Norton.
- Ding, C., Xiang, J., Cui, X., Wang, X., Li, D., Cheng, C., & Wang, B. (2022). Abnormal dynamic community structure of patients with attention-deficit/

- hyperactivity disorder in the resting state. *Journal of attention disorders*, 26(1), 34-47. doi:<https://doi.org/10.1177/1087054720959712>
- Dong , D., Duan , M., Wang , Y., Zhang , X., Jia , X., Li , Y., . . . Luo , C. (2019). Reconfiguration of dynamic functional connectivity in sensory and perceptual system in schizophrenia. *cerebral cortex*, 29(8), 3577-3589. doi:<https://doi.org/10.1093/cercor/bhy232>
- Donoho , D., & Johnstone , I. (1994). Ideal spatial adaptation by wavelet shrinkage. *Biometrika*, 81(3), 425-455.
- Edgar Canario, D. C. (2021). A review of resting-state fMRI and its use to examine psychiatric disorders. *Psychoradiology*, 1(1), 42-53. doi:<https://doi.org/10.1093/psyrad/kkab003>
- Elton, A., & Gao, W. (2015). Task-related modulation of functional connectivity variability and its behavioural correlations. *Human Brain Mapping*, 36, 3260–3272. doi:10.1002/hbm.22847
- Faghiri , A., Iraj, A., Damaraju, E., Belger, A., Ford, J., Mathalon, D., . . . Calhoun, V. (2020). Weighted average of shared trajectory: A new estimator for dynamic functional connectivity efficiently estimates both rapid and slow changes over time. *Journal of Neuroscience*, 334, 108600. doi:<https://doi.org/10.1016/j.jneumeth.2020.108600>
- Fair , D., Posner, J., Nagel , B., Bathula , D., Costa Dias , T., Mills , K., . . . Nigg , J. (2010). Atypical default network connectivity in youth with attention-deficit/hyperactivity disorder. *Biological Psychiatry*, 68(12), 1084-1091. doi:<https://doi.org/10.1016/j.biopsych.2010.07.003>
- Fedorenko, E., & Thompson-Schill, S. (2014). Reworking language network. *Trends in Cognitive Sciences*, 18(3), 120-126. doi:<https://doi.org/10.1016/j.tics.2013.12.006>
- Figuroa-Jimenez, M., Cañete-Massé, C., Carbó-Carreté, M., Zarabozo-Hurtado, D., Peró-Cebollero, M., Salazar-Estrada<sup>1</sup>, J., & Guàrdia-Olmos, J. (2020). Resting-state default mode network connectivity in young individuals with Downs Syndrome. *Brain and Behaviour*, 11(1). doi:10.1002/brb3.1905
- Fornito , A., Zalesky , A., & Breakspear, M. (2015). The connectomics of brain disorders. *Nature Reviews Neuroscience*, 16, 159–172. doi:<https://doi.org/10.1038/nrn3901>
- Fox, M., Snyder, A., Vincent, J., Corbetta, M., Van Essen, D., & Raichle, M. (2005). The human brain is intrinsically organized into dynamic, anticorrelated functional networks. *PNAS*, 102(27), 9673–9678. doi:10.1073/pnas.0504136102
- Friston , K. (2011). Functional and Effective connectivity: A review. *Brain Connectivity*, 1(1), 11-36. doi:<https://doi.org/10.1089/brain.2011.0008>



- Friston, K., Frith, C., Liddle, P., & Frackowiak, R. (1993). Functional connectivity: The principal-component analysis of large (PET) datasets. *Journal of cerebral blood flow and metabolism*, 13(1). doi:https://doi.org/10.1038/jcbfm.1993.4
- Friston, K., Frith, C., Liddle, P., & Frackowiak, R. (1993). Functional Connectivity: The principal-component analysis of large (PET) data sets. *Journal of Cerebral Blood Flow and Metabolism*, 13(1), 5-14. doi:https://doi.org/10.1038/jcbfm.1993.4
- Geman, S., & Geman, D. (1984). Stochastic relaxation, Gibbs distributions, and the Bayesian restoration of images. *IEEE Transactions on pattern analysis and machine intelligence*, 721-741.
- Ghosh, A., Rho, Y., McIntosh, A., Kötter, R., & Jirsa, V. (2008). Noise during rest enables the exploration of brain's repertoire. *PLOS computational biology*, 4(10), e1000196. doi:https://doi.org/10.1371/journal.pcbi.1000196
- Gifford, G., Crossley, N., Kempton, M., Morgan, S., Dazzan, P., Young, J., & McGuire, P. (2020). Resting state fMRI based multilayer network configuration in patients with schizophrenia. *Neuroimage: Clinical*, 25, 102169. doi:https://doi.org/10.1016/j.nicl.2020.102169
- Glerean, E., Salmi, J., Lahnakoski, J., Jaaskelainen, L., & Sams, M. (2012). Functional Magnetic Resonance Imaging phase synchronization as a measure of dynamic functional connectivity. *Brain Connectivity*, 2(2), 91-101. doi:https://doi.org/10.1089/brain.2011.0068
- Glerean, E., Salmi, J., Lahnakoski, J., Jääskeläinen, L., & Sams, M. (2012). Functional Magnetic Resonance Imaging Phase synchronization as a measure of dynamic functional connectivity. *Brain Connectivity*, 2(2), 91-101. doi:https://doi.org/10.1089/brain.2011.0068
- Gonzalez-Castillo, J., & Bandettini, P. (2018). Task-based dynamic functional connectivity: Recent findings and open questions. *NeuroImage*, 180, Part B, 526-533. doi:https://doi.org/10.1016/j.neuroimage.2017.08.006
- Gonzalez-Castillo, J., Hoy, C., Handwerker, D., Robinson, M., Buchanan, L., Saad, Z., & Bandettini, P. (2015). Tracking ongoing cognition in individuals using brief, whole-brain functional connectivity patterns. *PNAS*, 112(28), 8762-8767. doi:https://doi.org/10.1073/pnas.1501242112
- Gonzalez-Castillo, J., Hoy, C., Handwerker, D., & Bandettini, P. (2014). Task dependence, tissue specificity, and spatial distribution of widespread activation in large single-subject functional MRI datasets at 7T. *Cerebral Cortex*, 25(12), 4667-4677. doi:https://doi.org/10.1093/cercor/bhu148
- Gorgolewski, K., Durnez, J., & Poldrack, R. (2017). Preprocessed consortium for neuropsychiatric phenomics dataset. *F1000 Research*, 6, 1262. doi:https://doi.org/10.12688/f1000research.11964.1

- Guo, S., Zhao, W., Tao, H., Liu, Z., & Palaniyappan, L. (2017). The instability of functional connectivity in patients with schizophrenia and their siblings: A dynamic connectivity study. *Schizophrenia Research*, *195*, 183-189. doi:<https://doi.org/10.1016/j.schres.2017.09.035>
- H.Akaike. (1974). A new look at the statistical model identification. *IEEE transaction on automatic control*, *19*(6), 716-723. doi:10.1109/TAC.1974.1100705.
- Han , S., Cui, Q., Wang , X., Li , L., Li , D., He , Z., . . . Chen , H. (2020). Resting state functional network switching rate is differently altered in bipolar disorder and major depressive disorder. *Human Brain Mapping*, *41*(12), 3295-3304. doi:<https://doi.org/10.1002/hbm.25017>
- Hansen, E. C., Battaglia, D., Spiegler, A., Deco, G., & Jirsa, V. K. (2015). Functional connectivity dynamics: Modeling the switching behavior of the resting state. *NeuroImage*, *105*, 525-535. doi:<https://doi.org/10.1016/j.neuroimage.2014.11.001>
- Harlalka, V., Bapi, R., Vinod, P., & Roy, D. (2019). Atypical flexibility in dynamic functional connectivity quantifies the severity in Autism Spectrum Disorder. *Frontiers in Human Neuroscience*, *13*. doi:<https://doi.org/10.3389/fnhum.2019.00006>
- Henschel , L., Conjeti , S., Estrada , S., Diers , K., Fischl , B., & Reuter, M. (2020). FastSurfer - A fast and accurate deep learning based neuroimaging pipeline. *Neuroimage*, *219*, 117012. doi:<https://doi.org/10.1016/j.neuroimage.2020.117012>
- Hilger, K., Fukushima, M., Sporns, O., & Fiebach, C. J. (2019). Temporal stability of functional brain modules associated with human intelligence. *Human Brain Mapping*, *41*(2), 362-372. doi:<https://doi.org/10.1002/hbm.24807>
- Hindriks, R., Adhikari, M., Murayama, Y., Ganzetti, M., Mantini, D., Logothetis, N., & Deco, G. (2016). Can sliding-window correlations reveal dynamic functional connectivity in resting-state fMRI? *NeuroImage*, *127*(15), 242-256. doi:<https://doi.org/10.1016/j.neuroimage.2015.11.055>
- Hoffman , M., Billot , B., Iglesias , J., Fischl , B., & Dalca , A. (2020). Learning image registration without images. *Arxiv preprint*. doi:arXiv:2004.10282
- Hutchison , R., Womelsdorf, T., Allen , E., Bandettini, P., Calhoun, V., Corbetta , M., . . . Chang, C. (2013). Dynamic functional connectivity: Promise, issues and interpretations. *Neuroimage*, *80*, 360-378. doi:<https://doi.org/10.1016/j.neuroimage.2013.05.079>
- Hutchison, R., & et al. (2013). Dynamic functional connectivity: Promise, issues and interpretations. *NeuroImage*, *80*, 360-378. doi:<https://doi.org/10.1016/j.neuroimage.2013.05.079>

- IAEA. (2021). IMAGINE - IAEA Medical imAGIng and Nuclear mEdicine global resources database.  
doi:<https://humanhealth.iaea.org/HHW/DBStatistics/IMAGINE.html>
- Iglesias , E. J., Billot , B., Balbastre, Y., Tabari , A., Conklin, J., Alexander , D., . . . Fischl , B. (2021). Joint super-resolution and synthesis of 1 mm isotropic MP-RAGE volumes from. *NeuroImage*, 237.  
doi:[doi:10.1016/j.neuroimage.2021.118206](https://doi.org/10.1016/j.neuroimage.2021.118206)
- Insensee, F., Jaeger , P., Kohl , S., Peterson , J., & Maier-Hein , K. (2021). nnU-Net: a self-configuring method for deep learning-based biomedical image segmentation. *Nature methods*, 18, 203–211.  
doi:<https://doi.org/10.1038/s41592-020-01008-z>
- J. Candès, E., Li, X., Ma, Y., & Wright, J. (2011). Robust Principal Component Analysis? *Journal of ACM*, 58(3), 1-37.  
doi:<https://doi.org/10.1145/1970392.1970395>
- Jia , H., Hu, X., & Deshpande , G. (2014). Behavioral relevance of dynamics of the functional brain connectome. *Brain connectivity*, 4(9), 741-759.  
doi:<https://doi.org/10.1089/brain.2014.0300>
- Jockwitz, C., & Caspers, S. (2021). Resting-state networks in the course of aging—differential insights from studies across the lifespan vs. amongst the old. *Pflügers Archiv - European Journal of Physiology*, 473, 793–803.  
doi:<https://doi.org/10.1007/s00424-021-02520-7>
- King, B., Ruitenbeek, P., Leunissen, I., Cuypers, K., Heise, K.-F., Monteiro, T., . . . Swinnen, S. (2017). Age-related declines in motor performance are associated with decreased segregation of large scale resting state brain networks. *Cerebral Cortex*, 28(12), 4390-4402.  
doi:<https://doi.org/10.1093/cercor/bhx297>
- Kiviniemi, V., Vire, T., Remes, J., Elseoud, A., Starck, T., Tervonen, O., & Nikkinen, J. (2011). A sliding time-window ICA reveals spatial variability of default mode network in time. *Brain Connectivity*, 1(4), 339-347.  
doi:<https://doi.org/10.1089/brain.2011.0036>
- Kong, X., Kong, R., Orban, C., Wang, P., Zhang, S., Anderson, K., . . . Yeo, B. (2021). Sensory-motor cortices shape functional connectivity dynamics in the human brain. *Nature Communications*(12), 6373.  
doi:<https://doi.org/10.1038/s41467-021026704-y>
- Kucyi, A., Hove , M., Esterman, M., Hutchison, M., & Valera, E. (2017). Dynamic brain network correlates of spontaneous fluctuations in attention. *Cerebral cortex*, 27(3), 1831-1840. doi:<https://doi.org/10.1093/cercor/bhw029>
- Kudela, M., Harezlak, J., & Lindquist, M. (2017). Assessing uncertainty in dynamic functional connectivity. *NeuroImage*, 149, 165-177.  
doi:<https://doi.org/10.1016/j.neuroimage.2017.01.056>

- Kupis, L., Goodman, Z., Kornfeld, S., Hoang, S., Romero, C., Dirks, B., . . . Uddin, L. (2021). Brain Dynamics Underlying Cognitive Flexibility Across the Lifespan. *Cerebral Cortex*, *bhab156*. doi:<https://doi.org/10.1093/cercor/bhab156>
- Le, L., Lu, B., & Yan, C.-G. (2020). Stability of dynamic functional architecture differs between brain networks and states. *Neuroimage*, *216*, 116320. doi:<https://doi.org/10.1016/j.neuroimage.2019.116230>
- Lerman-Sinkoff, D., & Barch, D. (2016). Network community structure alterations in adult schizophrenia: identification and localization of alternations. *Neuroimage: Clinical*, *10*, 96-106. doi:<https://doi.org/10.1016/j.nicl.2015.11.011>
- Li, L., Lu, B., & Yan, C.-G. (2019). Stability of dynamic functional architecture differs between brain networks and states. *NeuroImage*, *216*, 116230. doi:<https://doi.org/10.1016/j.neuroimage.2019.116230>
- liégeois, R., Laumann, T. O., Snyder, A. Z., Zhou, J., & Yeo, B. (2017). Interpreting temporal fluctuations in resting-state functional connectivity MRI. *NeuroImage*, *163*, 437-455. doi:<https://doi.org/10.1016/j.neuroimage.2017.09.012>
- Lin, P., sun, J., Yu, G., Wu, Y., Yang, Y., Liang, M., & Liu, X. (2014). Global and local brain network reorganization in attention deficit/hyperactivity disorder. *Brain Imaging and Behaviour*, *8*, 558-569. doi:<https://doi.org/10.1007/s11682-013-9279-3>
- Lindquist, M., Xu, Y., Nebel, M. B., & Caffo, B. S. (2014). Evaluating dynamic bivariate correlations in resting-state fMRI: A comparison study and a new approach. *NeuroImage*, *101*, 531-546. doi:<https://doi.org/10.1016/j.neuroimage.2014.06.052>
- Liu, X., Chang, C., & Duyn, J. (2013). Decomposition of spontaneous brain activity into distinct fMRI co-activation patterns. *Frontiers in systems neuroscience*, *7*:101. doi:<https://doi.org/10.3389/fnsys.2013.00101>
- Lombardo, D., Casse-Perrot, C., Ranjeva, J.-P., Le Troter, A., Guye, M., Wirisch, J., . . . Battaglia, D. (2020). Modular slowing of resting state dynamic functional connectivity as a marker of cognitive dysfunction induced by sleep deprivation. *Neuroimage*, *222*(15), 117155. doi:<https://doi.org/10.1016/j.neuroimage.2020.117155>
- Long, Y., Liu, Z., Yuen Chan, C., Wu, G., Xue, Z., Pan, Y., . . . Pu, W. (2020). Altered temporal variability of local and large-scale resting state brain functional connectivity patterns in schizophrenia and bipolar disorder. *Frontiers in Psychiatry*, *11*. doi:<https://doi.org/10.3389/fpsyt.2020.00422>
- Long, Y., Lu, X., & Liu, Z. (2023). Temporal stability of the dynamic resting state functional brain network; current measures, clinical research progress and

- future perspectives. *Brain Sciences*, 13(3), 429.  
doi:<https://doi.org/10.3390/brainsci13030429>
- Long , Y., Ouyang, X., Yan, C., Wu, Z., Huang, X., Pu, W., . . . Palaniyappan, L. (2023). Evaluating test-retest reliability and sex-/age-related effects on temporal clustering coefficient of dynamic functional brain networks. *Human Brain Mapping*, 44(6), 2191-2208.  
doi:<https://doi.org/10.1002/hbm.26202>
- Lopez, M. M., Frederick, J., & Ventura, J. (2021). Evaluation of MRI denoising methods using unsupervised learning. *Frontiers in Artificial Intelligence*, 4:642731. doi:<https://doi.org/10.3389/frai.2021.642731>
- Maesschalck, R., Jouan-Rimbaud,, D., & Massart, D. (2000). *The Mahalanobis distance*. Chemometrics and Intelligent Laboratory Systems.  
doi:[doi:10.1016/S0169-7439\(99\)00047-7](https://doi.org/10.1016/S0169-7439(99)00047-7)
- Mahalanobis, P. (1930). On tests and measures of group divergence. *Journal of Asiatic Society of Bengal*, 26(4), 36.
- Mahmoudi, M., & Sapiro, G. (2005). Fast image and video denoising via non local means of similar neighborhoods. *IEEE signal processing letters*, 12(12).  
doi:[10.1109/LSP.2005.859509](https://doi.org/10.1109/LSP.2005.859509)
- Mazziotta , J., Toga , A., Evans , A., Fox , P., Lancaster, J., Zilles, K., & Woods , R. (2001). A probabilistic atlas and reference system for the human brain: International Consortium for Brain Mapping (ICBM). *Philosophical transactions of royal society*, 356, 1293-1322.
- McDonnell, M. (1981). Box filtering techniques. *Computer Graphics and Image Processing*, 17(1), 65-70. doi:[https://doi.org/10.1016/S0146-664X\(81\)80009-3](https://doi.org/10.1016/S0146-664X(81)80009-3)
- McGhee, G. (2006). *The geometry of evolution: Adaptive landscapes and theoretical morphospaces*. Cambridge: Cambridge University Press.
- McIntosh, A., Kovacevic, N., Lippe, S., Garrett, D., Grady, C., & Jirsa, V. (2010). The development of a noisy brain. *Archives Italiennes de Biologie*, 148(3), 323-337. doi:<https://doi.org/10.4449/aib.v148i3.1225>
- Miranda, L., Paul , R., Putz, B., Koutsouleris, N., & Muller-Myhsok, B. (2021). Systematic Review of Functional MRI Applications for Psychiatric Disease Subtyping. *Frontiers in Psychiatry*, 12.  
doi:<https://doi.org/10.3389/fpsy.2021.665536>
- Nguyen , T., Kovacevic , S., Dev , S., Lu , K., Liu, T., & Eyler , L. (2017). Dynamic functional connectivity in bipolar disorder is associated with executive function and processing speed: A preliminary study. *Neuropsychology*, 31(1). doi:<https://doi.org/10.1037/neu0000317>
- Oliver, I., Hlinka, J., Kopal, J., & Davidsen, J. (2019). Quantifying the Variability in Resting-State Networks. *Entropy*, 21. doi:[10.3390/e21090882](https://doi.org/10.3390/e21090882)

- O'Rilley , T., Teeuwisse , W., De gans , D., Koolstra , K., & Webb, A. (2021). In vivo 3D brain and extremity MRI at 50 mT using a permanent magnet Halbach array. *Magnetic Resonance in Medicine*, *85*, 495–505. doi:<https://doi.org/10.1002/mrm.28396>
- Osadebey , M., Pederson , M., Arnold , D., & Wendel-Mitoraj , K. (2018). Image quality evaluation in clinical research: A case study on brain and cardiac mri images in multi-center clinical trials. *IEEE journal of translational engineering in health and medicine*, *6*, 1-15. doi:<https://doi.org/10.1109/JTEHM.2018.2855213>
- Park , H., & Friston , K. (2013). Structural and Functional Brain Networks: From Connections to Cognition. *Science*, *342*(6158), 1238411 . doi:<https://doi.org/10.1126/science.1238411>
- Perona P , & Malik , J. (1990). Scale-space and edge detection using anisotropic diffusion. *IEEE Transactions on pattern analysis and machine intelligence*, *12*(7), 629-639.
- Pillai, A. S., & Jirsa, V. K. (2017). Symmetry breaking in space-time hierarchies shapes brain dynamics and behavior. *Neuron*, *94*(5), 1010-1026. doi:<https://doi.org/10.1016/j.neuron.2017.05.013>
- Poldarck, R., Baker , C., Durnez , J., Gorgolewski , K., Mathews , P., Munafo , M., . . . Yarkoni , T. (2017). Scanning the horizon: towards transparent and reproducible neuroimaging research. *Nature Reviews Neuroscience*, *18*, 115–126. doi:<https://doi.org/10.1038/nrn.2016.167>
- Poldrack, R., Congdon, E., Triplett, W., Gorgolewski, K., Karlsgodt , K., Mumford , J., . . . Bilder, R. (2016). A phenome-wide examination of neural and cognitive function. *Scientific Data*, *3*, 160110. doi:<https://doi.org/10.1038/sdata.2016.110>
- Ponce-Alvarez, A., Deco, G., Hagmann, P., Romani, G., Mantini, D., & Corbetta, M. (2015). Resting-state temporal synchronization networks emerge from connectivity topology and heterogeneity. *PLOS Computational Biology*, *11*(2), e1004100. doi:<https://doi.org/10.1371/journal.pcbi.1004100>
- Preti, M. G., Bolton, T., & De ville, D. (2017). The dynamic functional connectome: State of the art and perspectives. *Neuroimage*, *160*, 41-54. doi:<https://doi.org/10.1016/j.neuroimage.2016.12.061>
- Preti, M., Bolton, T., & Van De Ville , D. (2017). The dynamic functional connectome: State-of-the-art and perspectives. *NeuroImage*, *160*, 41-54. doi:<https://doi.org/10.1016/j.neuroimage.2016.12.061>
- Quinn, A., Vidaurre, D., Abeysuriya, R., Becker, R., Nobre, A., & Woolrich, M. (2018). Task-evoked dynamic network analysis through hidden markov modeling. *Frontiers in Neuroscience*, *12*, 603. doi:<https://doi.org/10.3389/fnins.2018.00603>

- Quiyuan , T., Bilgic , B., Fan , Q., Ngamsombat, C., Zarestskaya, N., Fultz, N., . . . Huang , S. (2021). Improving in vivo human cerebral cortical surface reconstruction using data-driven super-resolution. *Cerebral Cortex*, 31(1), 463–482. doi:<https://doi.org/10.1093/cercor/bhaa237>
- Rahman, M., Damaraju, E., Saha, D., Plis, S., & Calhoun, V. (2020). Statelets: high dimensional predominant shapes in dynamic functional network connectivity. *bioRxiv*. doi: <https://doi.org/10.1101/2020.08.16.252999>
- Rakthanmanon, T., Keogh, E., Lonardi, S., & Evans , S. (2011). Time series epenthesis: Clustering time series streams requires ignoring some data. *IEEE 11th International conference on data mining, vancouver, BC, Canada*, 547-556. doi:<https://doi.org/10.1109/ICDM.2011.146>
- Rakthanmanon, T., Keogh, E., Lonardi, S., & Evans, S. (2011). Time series Epenthesis: Clustering time series streams requires ignoring some data. *2011 IEEE 11th International Conference on Data Mining*, 547-556. doi:10.1109/ICDM.2011.146
- Ramesh , A., Khambhanpati , C., Monson , J., & Drew , P. (2004). Artificial intelligence in medicine. *The royal society of surgeons*, 334-338. doi:<https://doi.org/10.1308/147870804290>
- Ray , S. (2019). A Quick Review of Machine Learning Algorithms. *International Conference on Machine Learning, Big Data, Cloud and Parallel Computing (Com-IT-Con)*. doi:<https://doi.org/10.1109/comitcon.2019.8862451>
- Rudin , L., Osher , S., & Fatemi , E. (1992). Nonlinear total variation based noise removal algorithms. *Physica D: nonlinear phenomena*, 60 (1-4), 259-268.
- Saint-Marc, P., Chen , J.-s., & Medioni , G. (1991). Adaptive smoothing: A general tool for early vision. *Transactions on Pattern Analysis & Machine Intelligence*, 13(6), 514-529.
- Sastry, N. C., Roy, D., & Banerjee, A. (2023). Stability of sensorimotor network sculpts the dynamic repertoire of resting state over lifespan. *Cerebral Cortex*, 33(4), 1246-1262. doi:<https://doi.org/10/1093/cercor/bhac133>
- Schaefer , A., Kong , R., Gordon , E., Laumann, T., Zuo, X.-N., Holmes , A., . . . Yeo , B. (2018). Local-global parcellation of the Human Cerebral Cortex from Intrinsic functional connectivity MRI. *Cerebral Cortex*, 28(9), 3095-3114. doi:<https://doi.org/10.1093/cercor/bhx179>
- Sejowski , T. J., Churchland , P., & Movshon , J. (2014). Putting big data to good use in neuroscience. *Nature Neuroscience*, 17, 1440–1441. doi:<https://doi.org/10.1038/nn.3839>
- Shafto, M., Tyler, L., Dixon, M., Taylor, J., Rowe, J., Cusack, R., . . . Matthews, F. (2014). The Cambridge Centre for Ageing and Neuroscience(CamCAN) study protocol: a cross-sectional, lifespan, multidisciplinary examination of healthy cognitive ageing. *BMC Neurology*, 14, 204 . doi:<https://doi.org/10.1186/s12883-014-0204-1>

- Shen, C., Kim, J., & Wang, L. (2010). Scalable large-margin mahalanobis distance metric learning. *IEEE transactions on Neural Networks*, 21(9), 1524-1530. doi:10.1109/TNN.2010.2052630
- sheth , K., Mazureck , M., Yuen , M., Cahn , B., Shah , J., Ward , A., . . . Kimberly , T. (2021). Assessment of Brain Injury Using Portable, Low-Field Magnetic Resonance Imaging at the Bedside of Critically Ill Patients. *JAMA Neurology*, 78(1), 41–47. doi:https://doi.org/10.1001/jamaneurol.2020.3263
- Shetta, O., & Niranjana, M. (2020). Robust subspace methods for outlier detection in genomic data circumvents the curse of dimensionality. *Royal Society of Open Science*, 7(2). doi:https://doi.org/10.1098/rsos.190714
- Sladky , R., Friston , K., Trostl, J., Cunnington , R., Moser, E., & Windischberger, C. (2011). Slice timing effects and their correction in functional MRI. *NeuroImage*, 58(2), 588-594. doi:https://doi.org/10.1016/j.neuroimage.2011.06.078
- Smith , S., Beckmann, C., Andersson , J., Auerbach , E., Bijsterbosch , J., Douaud , G., . . . Glasser , M. (2013). Resting state fMRI in human connectome project. *Neuroimage*, 80, 144-168. doi:https://doi.org/10.1016/j.neuroimage.2013.05.039
- Surampudi, S., Naik, S., Surampudi, R., Jirsa , V., Sharma , A., & Roy, D. (2018). Multiple kernel learning model for relating structural and functional connectivity in the brain. *Scientific reports*, 8, 3265. doi:https://doi.org/10.1038/s41598-018-21456-0
- Taylor, J., Williams , N., Cusack, R., Auer, T., Shafto, M., Dixon , M., . . . Henson , R. (2017). The Cambridge Centre for Ageing and Neuroscience (Cam-CAN) data repository: structural and functional MRI, MEG and cognitive data from a cross-sectional adult lifespan sample. *NeuroImage*, 144, Part B, 262-269. doi:https://doi.org/10.1016/j.neuroimage.2015.09.018
- Tomasi, C., & Manduchi, R. (1998). Bilateral filtering for gray and color images. *In Sixth international conference on computer vision (IEEE Cat. No. 98CH36271)*, 839-846.
- Tomasi, D., & Volkow, N. (2012). Aging and functional brain networks. *Molecular Psychiatry*, 17, 549–558. doi:https://doi.org/10.1038/mp.2011.81
- Tooley , U., Bassett, D., & Mackey, A. (2022). Functional brain network community structure in childhood: Unfinished territories and fuzzy boundaries. *Neuroimage*, 247, 118843. doi:https://doi.org/10.1016/j.neuroimage.2021.118843
- Turpin , J., Unadkat, P., Thomas , J., Kleiner, N., Khazahnehdari , S., Wanchoo, S., . . . Schulder, M. (2020). Portable Magnetic Resonance Imaging for ICU Patients. *Critical Care Explorations*, 2(12), e306. doi:https://doi.org/10.1097/CCE.0000000000000306



- Tzourio-Mazoyer, N., Landeau, B., Papathanassiou, D., Crivello, F., Etard, O., Delcroix, N., . . . Joliot, M. (2002). Automated anatomical labeling of activations in SPM using a macroscopic anatomical parcellation of MNI MRI single subject brain. *NeuroImage*, *15*(1), 273-289.  
doi:<https://doi.org/10.1006/nimg.2001.0978>
- Vidaurre, D., Quinn, A., Baker, A., Dupret, D., Tejero-Cantero, A., & Woolrich, M. (2016). Spectrally resolved fast transient brain states in electrophysiological data. *NeuroImage*, *126*, 81-95.  
doi:<https://doi.org/10.1016/j.neuroimage.2015.11.047>
- Vidaurre, D., Smith, S., & Woolrich, M. (2017). Brain network dynamics are hierarchically organized in time. *PNAS*, *114*(48), 12827-12832.  
doi:<https://doi.org/10.1073/pnas.1705120114>
- Viduarre, D., Smith, S., & Woolrich, M. (2017). Brain network dynamics are hierarchically organized in time. *PNAS*, *114*(48), 12827-12832.  
doi:<https://doi.org/10.1073/pnas.1705120114>
- Viviano, R., Raz, N., Yuan, P., & Damoiseaux, J. (2017). Associations between dynamic functional connectivity and age, metabolic risk and cognitive performance. *Neurobiology of Aging*, *59*, 135-143.  
doi:<https://doi.org/10.1016/j.neurobiolaging.2017.08.003>
- Viviano, R., Raz, N., Yuan, P., & Damoiseaux, J. (2017). Associations between dynamic functional connectivity and age, metabolic risk, and cognitive performance. *Neurobiology of Aging*, *59*, 135-143.  
doi:<https://doi.org/10.1016/j.neurobiolaging.2017.08.003>
- Vohryzek, J., Deco, G., Cessac, B., Kringelbach, M., & Cabral, J. (2020). Ghost Attractors in Spontaneous Brain Activity: Recurrent Excursions into Functionally-Relevant BOLD Phase-Locking states. *Frontiers in Systems Neuroscience*, *14*. doi: <https://doi.org/10.3389/fnsys.2020.00020>
- Voytek, B., Kramer, M., Case, J., Lepage, K., Tempesta, Z., Knight, R., & Gazzaley, A. (2015). Age-related changes in 1/f neural electrophysiological noise. *Journal of Neuroscience*, *35*(38), 13257-13265.  
doi:<https://doi.org/10.1523/JNEUROSCI.2332-14.2015>
- Wagenmaker, E.-J., & Farrell, S. (2004). AIC model selection using Akaike weights. *Psychonomic Bulletin and review*, *11*, 192–196.  
doi:<https://doi.org/10.3758/BF03206482>
- Wang, Z., Liu, J., Zhong, N., Qin, Y., Zhou, H., & Li, K. (2012). Changes in the brain intrinsic organization in both on-task state and post-task resting state. *NeuroImage*, *62*, 394- 407.  
doi:[doi:10.1016/j.neuroimage.2012.04.051](https://doi.org/10.1016/j.neuroimage.2012.04.051)
- Wang, Z., Sheikh, H., & Bovik, A. (2002). No-reference perceptual quality assessment of JPEG compressed images. *Proceedings. International conference on image processing.*, *1*, 1-1.

- Winston, P. (1984). *Artificial Intelligence* .
- Woodard , J., & Carley-Spencer, M. (2006). No-reference image quality metrics for structural MRI. *Neuroinformatics*, *4*(3), 243-262.  
doi:<https://doi.org/doi:10.1385/ni:4:3:243>
- Wu , H., Xie , Q., Pan , J., Liang, Q., Lan , Y., Guo , Y., . . . Qin , P. (2023). Identifying patients with cognitive motor dissociation using resting-state temporal stability. *Neuroimage*, *272*, 120050.  
doi:<https://doi.org/10.1016/j.neuroimage.2023.120050>
- Xia, Y., Chen, Q., Shi, L., Li, M., Gong, W., Chen, H., & Qiu, J. (2018). Tracking the dynamic functional connectivity structure of the human brain across the adult lifespan. *Human Brain Mapping*, *40*, 717–728.  
doi:[10.1002/hbm.24385](https://doi.org/10.1002/hbm.24385)
- Y. Kuo, F., & Sloan, I. (2005). Lifting the Curse of Dimensionality. *NOTICES OF THE AMS*, *52*(11), 1320-1328.
- Yaesoubi, M., Miller, R., & Calhoun, V. (2015). Mutually temporally independent connectivity patterns: A new framework to study the dynamics of brain connectivity at rest with application to explain group difference based on gender. *NeuroImage*, *107*, 85-94.  
doi:<https://doi.org/10.1016/j.neuroimage.2014.11.054>
- Yang, A., Huang, C.-C., Yeh , H.-L., Liu, M.-E., Hong, C.-J., Tu, P.-C., . . . Tsai, S.-J. (2013). Complexity of spontaneous BOLD activity in default mode network is correlated with cognitive function in normal male elderly: a multiscale entropy analysis. *Neurobiology of Ageing*, *34*(2), 428-438.  
doi:<https://doi.org/10.1016/j.neurobiolaging.2012.05.004>
- Yeshurun, Y., Nguyen, M., & Hasson, U. (2021). The default mode network: where the idiosyncratic self meets the shared social world. *Nature reviews neuroscience*, *22*, 181-192. doi:<https://doi.org/10.1038/s41583-020-00420-w>
- Yin, D., Liu, W., Zeljic, K., Wang, Z., Lv, Q., Fan, M., . . . Wang, Z. (2016). Dissociable changes in frontal and parietal cortices in inherent functional flexibility across the human life span. *The Journal of Neuroscience*, *36*(39), 10060-10074. doi:<https://doi.org/10.1523/JNEUROSCI.1476-16.2016>
- Yu , Z., Qin , J., Xiong , X., Xu , F., Wang, J., Hou , F., & Yang, A. (2020). Abnormal topology of brain functional networks in unipolar depression and bipolar disorder using optimal graph thresholding. *Progress in neuro-psychopharmacology and biological psychiatry*, *96*, 109758.  
doi:<https://doi.org/10.1016/j.pnpbp.2019.109758>
- Yu, M., Song, H., Huang, J., Song, Y., & Liu, J. (2020). Motor Learning improves the stability of large-scale brain connectivity pattern. *Frontiers in Human Neuroscience*, *14*. doi:<https://doi.org/10.3389/fnhum.2020.571733>

- Zhang , J., Cheng , W., Liu, Z., Zhang , K., Lei, X., Yao , Y., . . . Feng, J. (2016). Neural, electrophysiological and anatomical basis of brain-network variability and its characterisitc change in mental disorders. *Brain*, 139(8), 2307-2321. doi:<https://doi.org/10.1093/brain/aww143>
- Zhang , L., Wu , h., Zhang , A., Bai , T., ji , G.-j., Tian , Y., & Wang , K. (2021). Aberrant brain network topology in the frontoparietal-limbic circuit in bipolar disorder: a graph theory study. *European Archives of psychiatry and clinical neuroscience*, 271, 1379-1391. doi:<https://doi.org/10.1007/s00406-020-01219-7>
- Zhang, J., & et al. (2016). Neural, electrophysiological and anatomical basis of brain-network variability and its characteristic changes in mental disorders. *Brain*, 139(8), 2307–2321. doi:<https://doi.org/10.1093/brain/aww143>

# Appendix

## Supplementary figures and tables

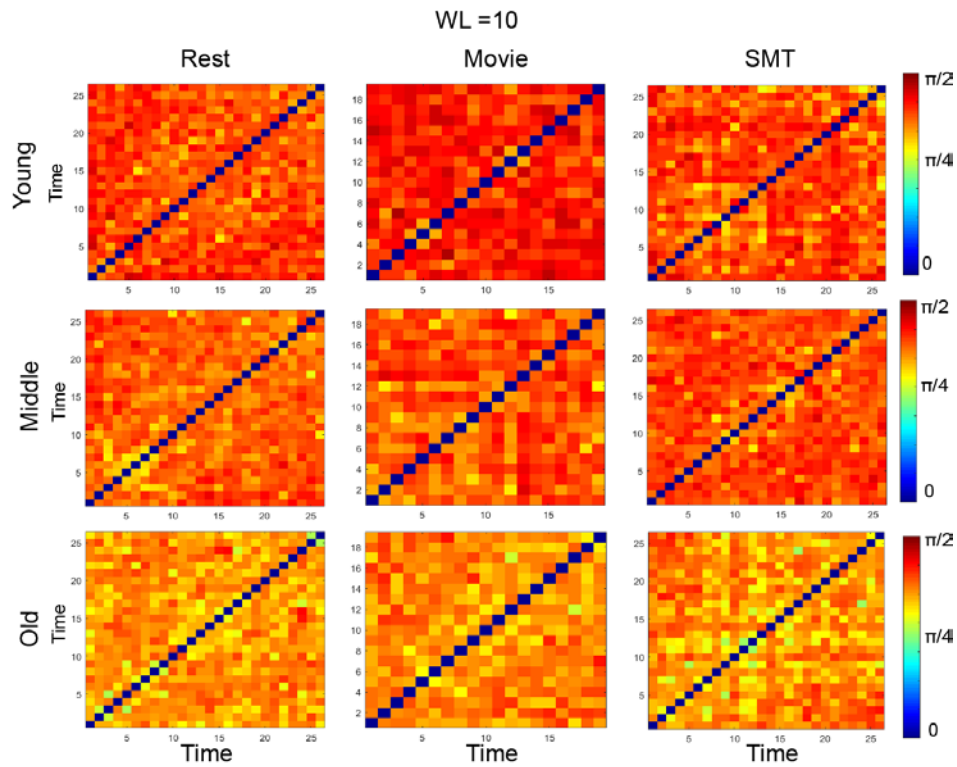


**Figure A 2.1** Temporal stability matrices of the resting state, naturalistic movie watching task and sensorimotor task, where each entry is the principal angle between dominant dFC subspaces at and , for young and old adults. For validation of the results where dFC was estimated using BOLD phase coherence, we calculated dFC using sliding window approach with (window length)  $WL = 10$  time points.

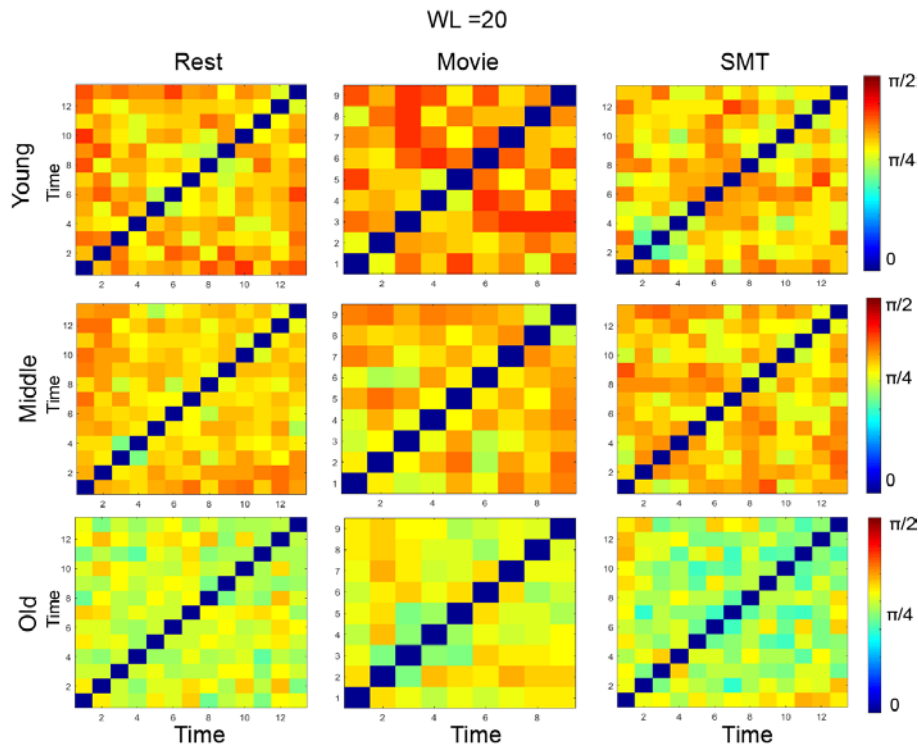


**Figure A 2.2** Temporal stability matrices of the resting state, naturalistic movie watching task, and sensorimotor task, for both young and old adults. dFC was estimated using sliding window approach with (window length) WL= 20 time points.

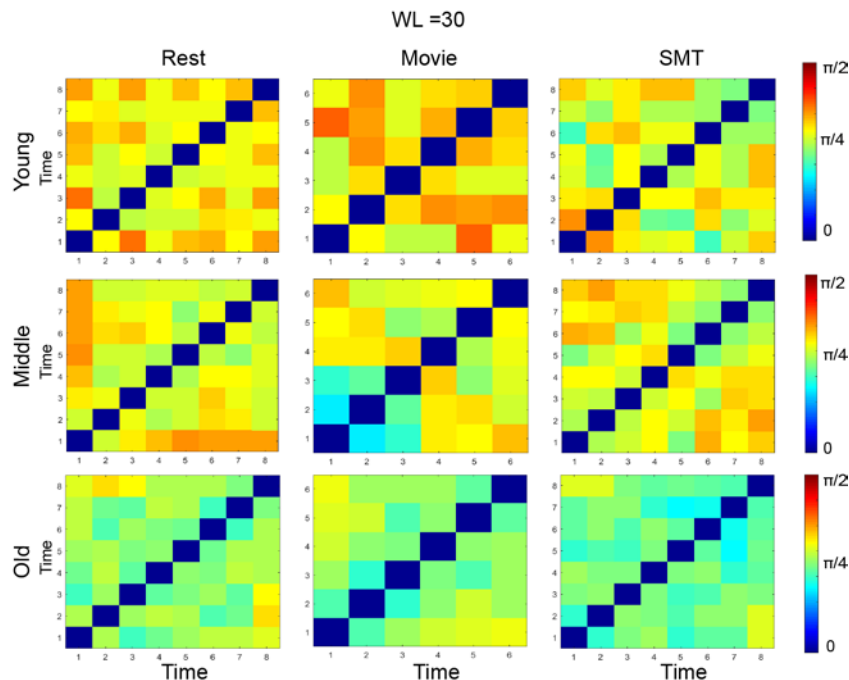


**Figure A2.3** Temporal stability matrices of the resting state, naturalistic movie watching task, and sensorimotor task, for both young and old adults. dFC was estimated using sliding window approach with (window length) WL= 30 time points

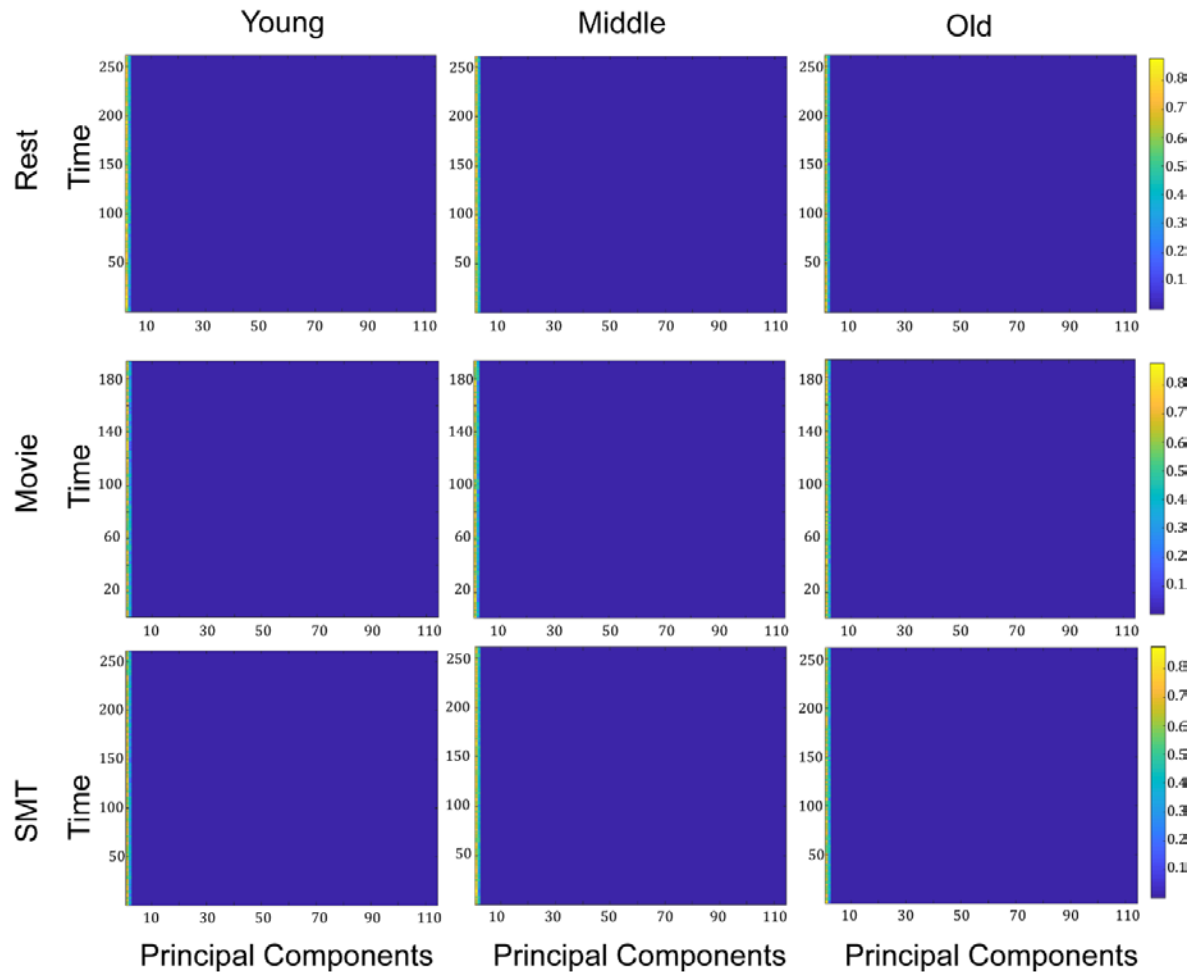


**Figure A2.4** The Plot represents the variance explained by all 116 principal components of the input dFC matrix for all categories. The first three principal components explain almost 99% of the variance of the input matrix.

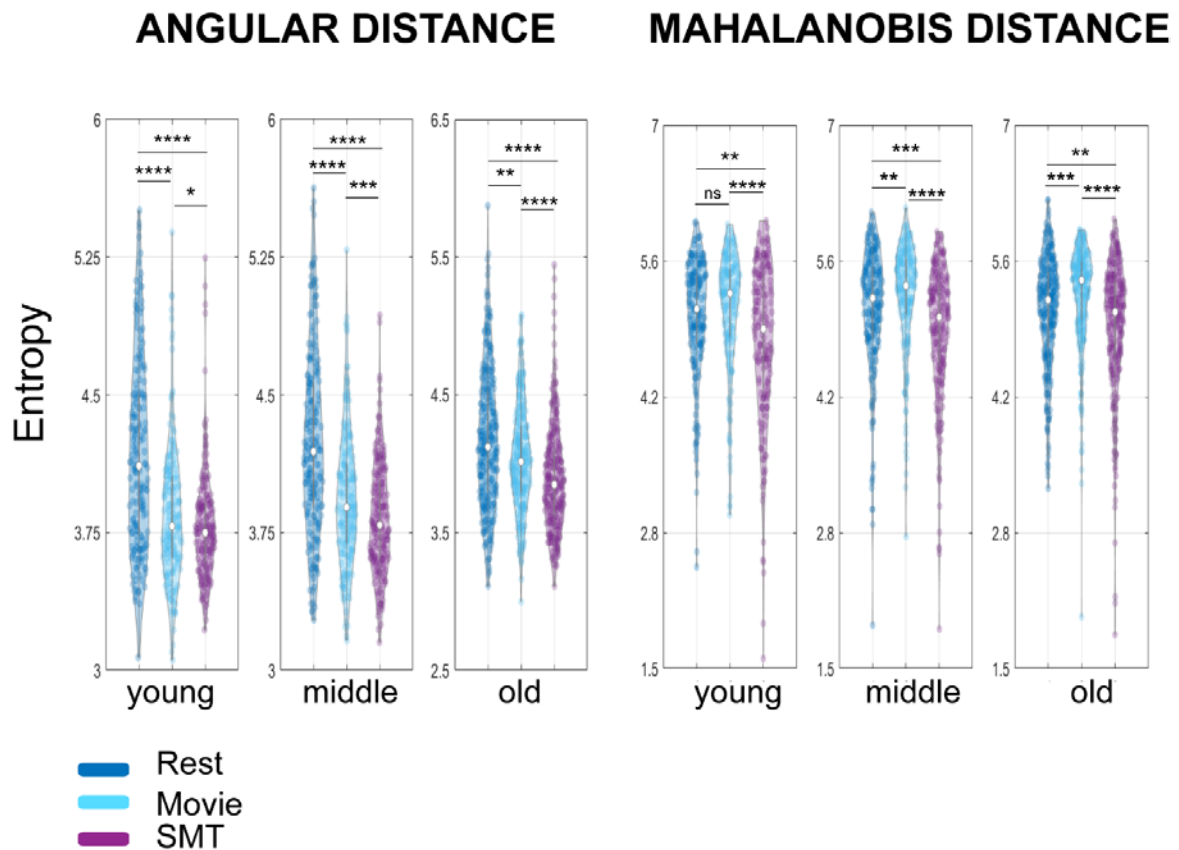


**Figure A2.6** The plot represents entropy of temporal stability matrices of resting state (rest), movie watching (movie) and sensorimotor task (smt) across young, middle and old adults, in both angular distance and Mahalanobis distance metric.

In angular distance, comparing the median values, peak entropy was reported in temporal stability matrices of resting state, followed by movie watching task and sensorimotor task. The distributions were non-parametric. Wilcoxon sign rank test revealed significant differences between entropy of temporal dynamics matrices of resting state and movie watching task, movie watching and sensorimotor task and sensorimotor task and resting state in young, middle and old adults as shown below:

Angular distance	rest - movie	movie-smt	smt-rest
Young	p=1.10e-10	p=0.034	p=2.6e-17
Middle	p=6.9e-11	p=5.19e-04	p=5.65e-21
Old	p=0.0013	p=4.9e-09	p=9.81e-17

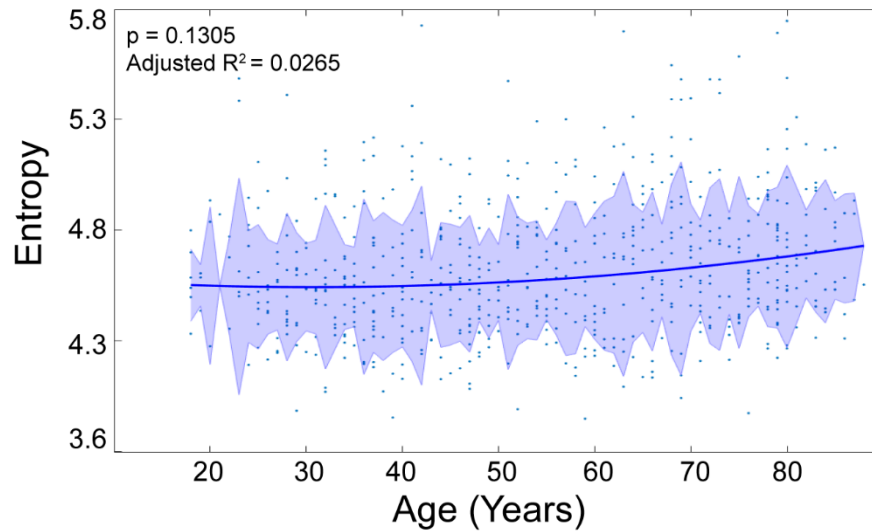
*In Mahalanobis distance, although the median values report peak entropy in movie watching task, followed by resting state and sensorimotor task, the violin plot indicates high variability of entropy values in resting state and movie watching task among middle and elderly. Wilcoxon sign rank test revealed significant differences between entropy of temporal dynamics matrices of resting state and movie watching task, movie watching and sensorimotor task and sensorimotor task and resting state in young, middle and old adults as shown below:*

<b>Mahalanobis distance</b>	<b>rest - movie</b>	<b>movie - smt</b>	<b>rest - smt</b>
Young	ns	p=1.9e-05	p=0.0014
Middle	p=0.0094	p=1.65e-10	p=2.9e-04
Old	p=7.6e-04	p=1.7e-10	p=0.0073



## Angular Distance

## Default Mode Network



## Salience Network

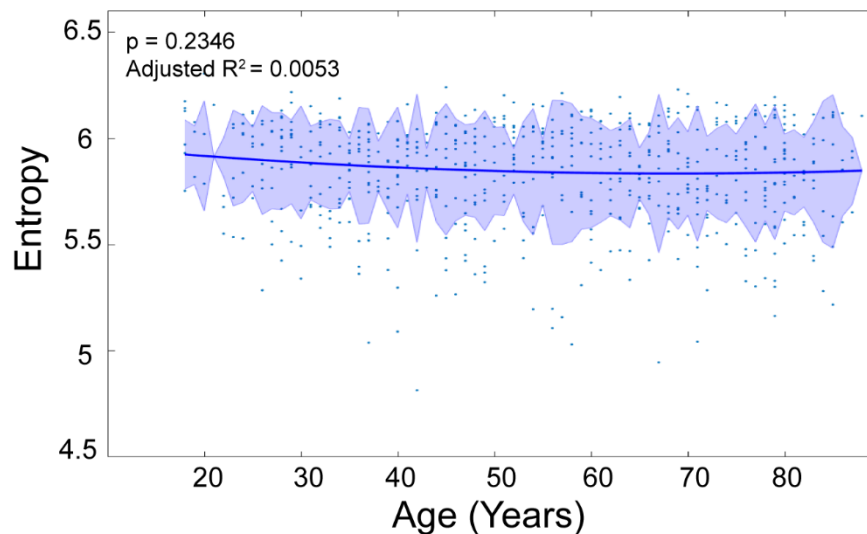


**Figure A2.6** Scatter plot of entropy of temporal dynamics matrices of resting state brain network subspaces (default mode network, salience network) across lifespan ageing ( $N=645$  participants) estimated with angular distance metric. A quadratic regression model is fitted onto the entropy values. 'p' is effectively a 2-sided t-test against the corresponding coefficient being zero.

## Mahalanobis Distance

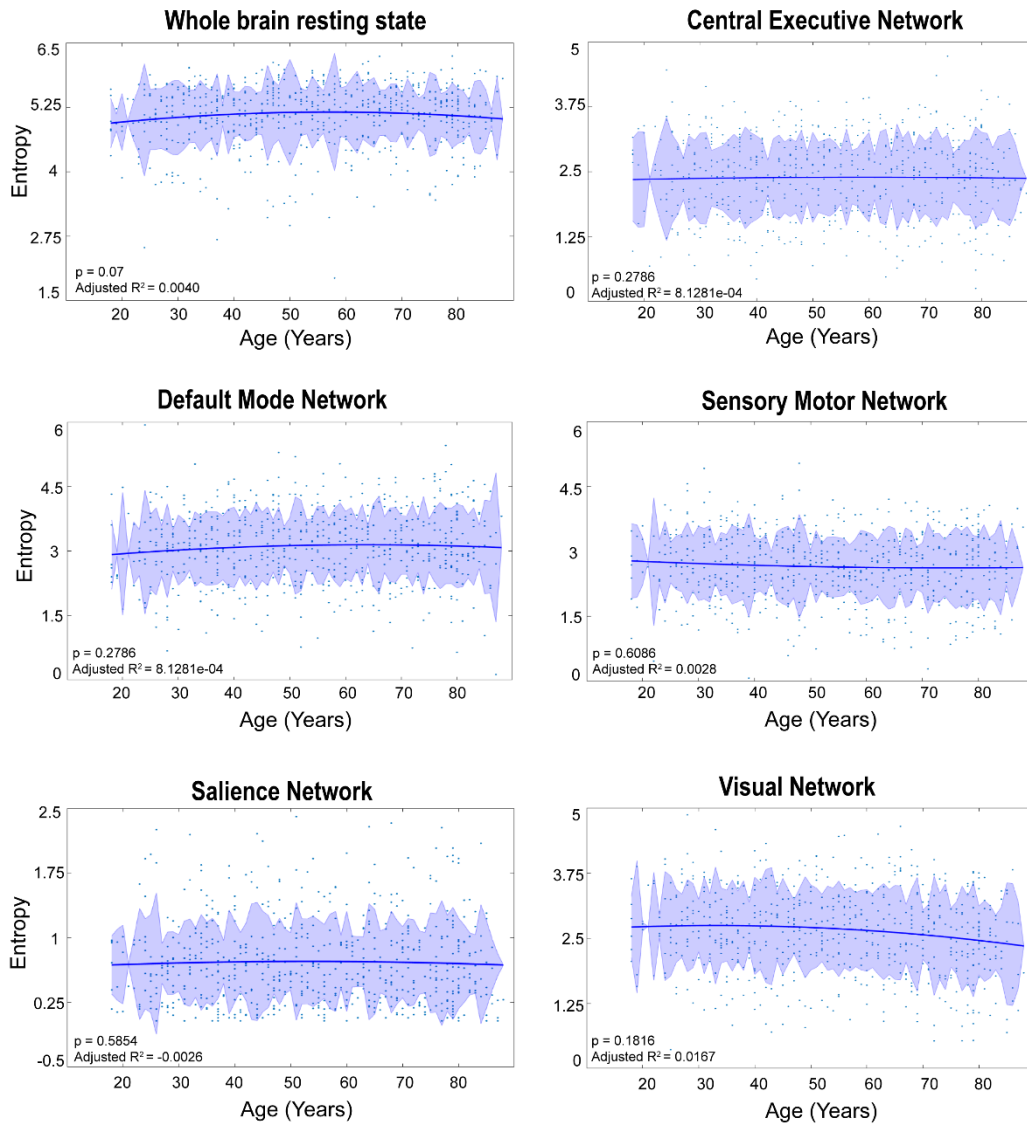


**Figure A2.7** Life span ageing related changes in temporal stability of dynamic functional connectivity subspace of whole-brain resting state, central executive network, default mode network, sensorimotor network, salience network and Visual network estimated with Mahalanobis distance metric. A quadratic regression model is fitted onto the entropy values. ‘p’ is effectively a 2-sided t-test against the corresponding coefficient being zero.

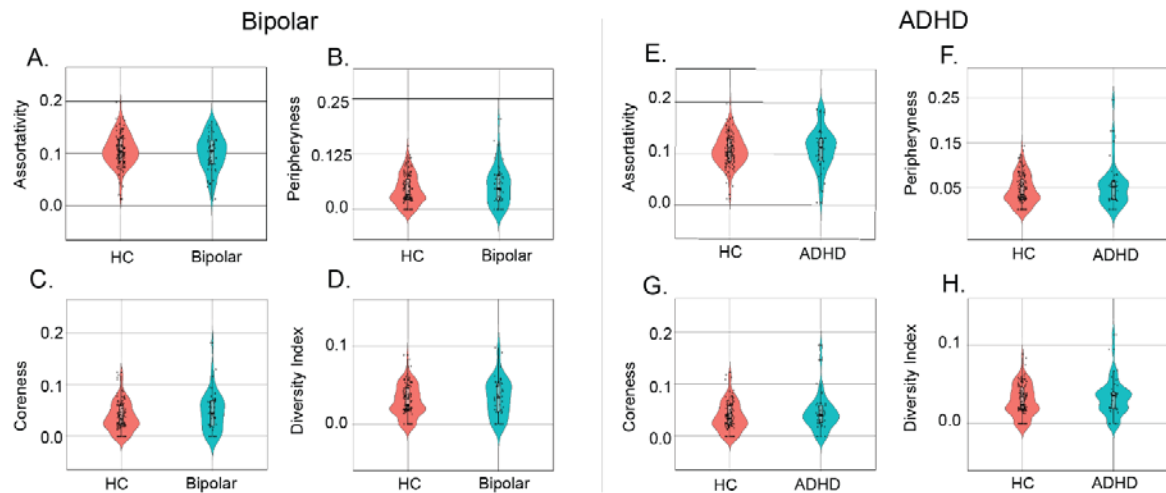


**Figure A3.1**(A-D) Violin plots showing community interaction motifs (assortativity, coreness and peripheryness) and diversity index averaged across all communities per subject in participants with bipolar disorder (green) and healthy controls (orange) (E-F) Violin plots showing community interaction motifs (assortativity, coreness and peripheryness) and diversity index averaged across all communities per subject in participants with ADHD (green) and healthy controls (orange)

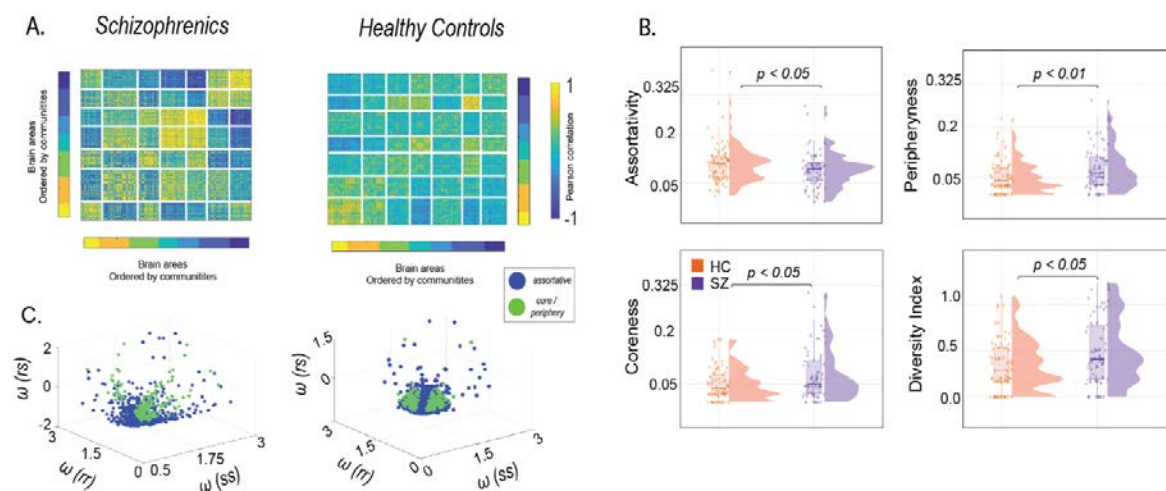
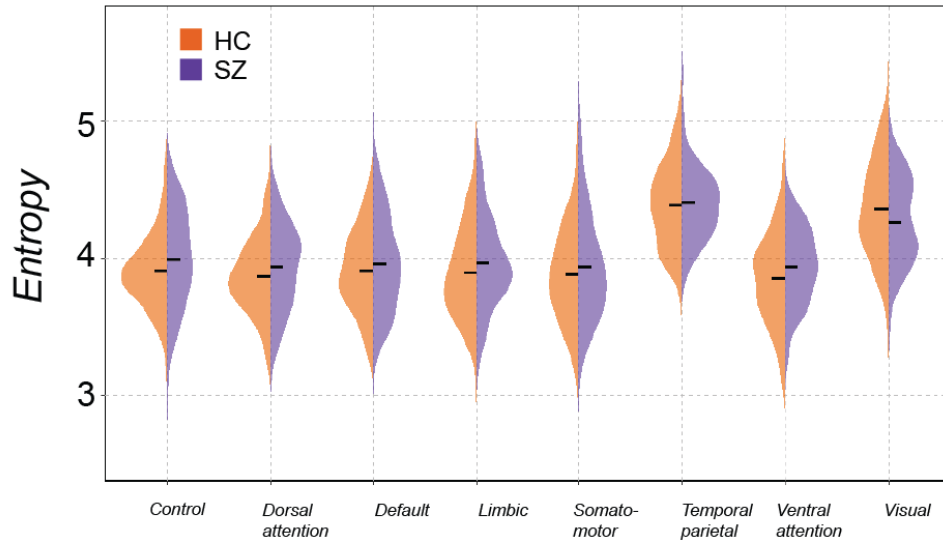


**Figure A3.2** (A) Static functional connectivity matrices where each entry is the Pearson correlation between brain regions  $n$  and  $p$  ordered by communities (B) Each pair of communities,  $r$  and  $s$  are classified into one of three community motifs – assortative, coreness and peripheryness. Diversity index averaged across all brain regions per subject. The violin plots indicate, in schizophrenics communities are less assortative (C) Morphospace constructed by using all pairs of community interactions and are colour coded – blue (assortative community interactions) and green (core or peripheryness community interaction).

## A. Dataset 1 (UCLA)



## B. Dataset 2 (COBRE)

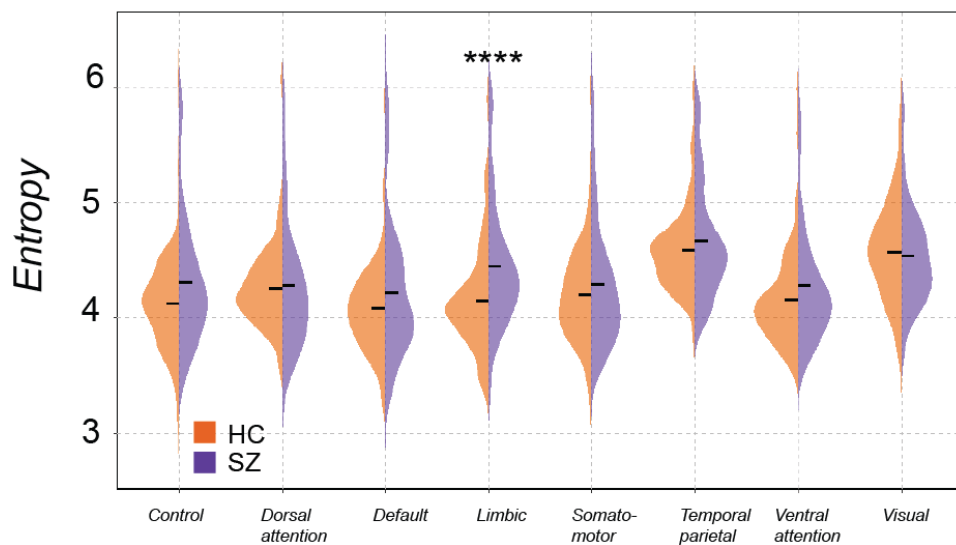


**Figure A3.3** Quantifying temporal stability using entropy for the resting state networks defined in Schaeffer atlas in Dataset 1 (A) and Dataset 2 (B). Statistically significant differences (uncorrected) are indicated using \* ( $P \leq 0.05$ ), \*\* ( $P \leq 0.01$ ), \*\*\* ( $P \leq 0.001$ ), \*\*\*\* ( $P \leq 0.0001$ ), ns (not significant).

# List of Publications

1. **Sastry, Nisha Chetana**, Banerjee, Arpan. Dynamicity of brain network organization & their community architecture as characterizing features for classification of common mental disorders from whole-brain connectome (Under review). Medrxiv. 2023.07. 14.23292699  
Doi: <https://doi.org/10.1101/2023.07.14.23292699>
  
2. **Sastry, Nisha Chetana**, BE, Roy, Dipanjan, PhD, Banerjee Arpan, PhD, Stability of sensorimotor network sculpts the dynamic repertoire of resting state over lifespan, Cerebral Cortex, 2022 (**selected as cover**)  
Doi: <https://doi.org/10.1093/cercor/bhac133>

# Selected list of Conferences

1. **Sastry, Nisha Chetana**, Banerjee, Arpan. Characterising spatiotemporal landscape of functional connectome and its changes in schizophrenia. **Montreal. OHBM 2023**. Poster Presentation.
2. **Sastry, Nisha Chetana**, Banerjee, Arpan. Characterizing temporal and community architecture in resting-state fMRI of patients with common mental health disorders. San Diego. **SfN Neuroscience 2022**. Poster Presentation.
3. **Sastry, Nisha Chetana**, Roy, Dipanjan, Banerjee, Arpan. Stability of sensorimotor network sculpts the dynamic repertoire of resting state across age. Virtual conference. **ACCS 2021**. Poster Presentation
4. **Sastry, Nisha Chetana**, Roy, Dipanjan, Banerjee, Arpan. Dynamic Repertoire of the Brain during Task and Rest. Berlin (**Virtual due to COVID**) **BCN 2020**. Poster Presentation
5. **Sastry, Nisha Chetana**, Roy, Dipanjan, Banerjee, Arpan. Dynamic Repertoire of the Brain during Task and Rest. BITS Goa. **ACCS 2019**. Oral Presentation

